3D PTV applied to a viscous flow in a cylindrical domain

van der Starre, A.

Award date:
2004

TU/e technische universiteit eindhoven

Eindhoven University of Technology

Department of Applied Physics
Fluid Dynamics Laboratory
Building: Cascade
P.O. Box 513
5600 MB Eindhoven

Title	:	$3D$ PTV applied to a viscous flow in a cylindrical domain
Author	:	A. van der Starre
Reportnumber	:	R-1585-A
Date	:	June 2002

Master's thesis of the period April 2001 - June 2002.

Group	:	Vortex Dynamics
Advisors	:	Dr. H.J.H. Clercx Prof. dr. ir. G.J.F. van Heijst

Abstract

The work presented in this report encompasses a study on the currently used Three Dimensional Particle Tracking Velocimetry ($3D$ PTV) measurement technique. The focus will be on improving the measurement technique in order to find long particle trajectories. Searching for long particle trajectories is very ambitious, but when found it results in very interesting Lagrangian information.

Under steady flow conditions long particle trajectories are found. These particle trajectories are quantitatively highly comparable to numerical simulations. The particle density is shown to be critical, when searching for long particle trajectories. The best results are obtained, when about 200 detected particles are used.

To be able to do long-time experiments a new periodic forcing protocol, consisting of four subsequent steady flow steps, with a net zero endwall displacement after a global period time T, is introduced. A thorough analysis of this protocol is carried out analytically and numerically. Periodic-1 lines are found and some mixing properties are investigated. First attempts have been made to measure particle trajectories in flows with this forcing protocol. Unfortunately, these experiments are limited to the measurements of segments of particle trajectories only, due to a too high particle density.

Contents

Chapter 1

Introduction

1.1 Scope

In general fully three dimensional fluid flows are still poorly understood. A lot more is known about it's two dimensional counterpart. In this report a simple three dimensional geometry, the cylinder with moving endwalls, will be used as an archetypal flow domain for three dimensional flows in general.

The thesis of Michel Speetjens (2001) is used as a guide-line for this report. The experimental and numerical investigation by Speetjens was focused on advection problems in a cylindrical domain with moving endwalls for low Re numbers. Mixing is a keyword in his thesis, but only on a level where molecular effects do not come into play. He used the dynamical point of view, where flow topology, chaos and dynamical systems play a central role. For doing numerical simulations he developed a spectral flow solver. To visualize the fluid motion in his experiments he made use of Ordinary Dye (OD), Fluorescent Dye (FD) and of small particles. The OD experiments gave qualitative results only, measurements have been repeated and improved a little by De Groot (2001). FD experiments with LIF (Laser Induced Fluorescence) gave concentration related quantitative results, see also Nijdam (2000).

This report focuses on the third visualization technique. This technique, called Three Dimensional Particle Tracking Velocimetry ($3D$ PTV), visualizes the small particles in a quantitative way. The basic idea is very simple: record the motion of small particles seeded in the fluid, with a couple of cameras, viewing from a slightly different angle. When a calibration in-situ has been done, the positions of these small particles are known. Tracking these particles, if passive, gives Lagrangian information about the fluid flow.

Speetjens carried out $3D$ PTV experiments for the steady flow case. The velocity fields and Lagrangian particle trajectories showed a high degree of correspondence to numerical simulations. However, he concluded that the PTV algorithm is ill-suited for long(er) time particle tracking, especially when using a higher particle density.

The aim is to improve the $3D$ PTV technique so, that long particle trajectories can be found. The measured Lagrangian trajectories are compared to numerical simulations. To be able to perform long-time experiments, a four-step endwall displacement (denoted as protocol D) is introduced, with the property of having the endwalls back in the initial positions after a global forcing period T.

1.2 Outline of this report

In chapter 2 some basic aspects of fluid dynamics are given, with tools to find periodic structures and symmetries of a periodically forced fluid in the paragraphs 2.4 and 2.5. In chapter 3 the steady flow is introduced and some special properties are given. The steady flow is important, because it can be seen as the basic building block for time-periodic forcing protocols. In paragraph 3.2 the

forcing protocols A, B and C from Speetjens and the new forcing protocol D are introduced. The numerical analysis of protocol D is treated in chapter 4. In chapter 5 the $3D$ PTV algorithm is explained, the used experimental set-up is described and some useful equations in optics are derived. In chapter 6 an accuracy assessment of the $3D$ PTV algorithm is carried out. Quality factors and accuracy tools are introduced to support the $3D$ PTV measurements. In chapter 7 the conclusions and recommendations are given.

Chapter 2

Three-dimensional Stokes flow in a cylindrical domain

In this chapter the basic aspects of a Stokes flow in a cylindrical domain are given[1].

2.1 Tracer kinematics

The motion of passive tracers in a fluid can be described by the $3D$ kinematic vector equation

$$\frac{d\boldsymbol{x}}{dt} = \boldsymbol{u}(\boldsymbol{x},t), \qquad \boldsymbol{x}(0) = \boldsymbol{x}_0, \tag{2.1}$$

describing the temporal evolution of the position $\boldsymbol{x}$ of a passive tracer released at the position $\boldsymbol{x}_0$ in the flow field $\boldsymbol{u}(\boldsymbol{x},t)$. The general solution of (2.1) can be formally represented as

$$\boldsymbol{x}(t) = \boldsymbol{\Phi}_t(\boldsymbol{x}_0), \tag{2.2}$$

and states the current position $\boldsymbol{x}$ to be uniquely determined through the initial tracer location $\boldsymbol{x}_0$. The orbit of a passive tracer is described by the parameter function

$$\boldsymbol{X}_t(\boldsymbol{x}_0) = \boldsymbol{\Phi}_{t'}(\boldsymbol{x}_0), \qquad t' = [0,t], \tag{2.3}$$

propagating from $\boldsymbol{x}_0$ to the current location $\boldsymbol{x}$ in course of time. For the particular case of a $3D$ laminar incompressible flow, the kinematic equation (2.1) constitutes a $3D$ deterministic conservative dynamical system.

In this report steady flow and time-periodic flow will be considered only. In a steady flow an explicit time-dependence is absent in the flow field, in consequence tracer paths coincide with the streamlines of the flow. Time-periodic systems are characterized by $\boldsymbol{u}(\boldsymbol{x},t) = \boldsymbol{u}(\boldsymbol{x},t+T)$, with T the global period time. Time-periodic systems allow for a reduction of the continuous orbits (2.2) into the discrete relation

$$\boldsymbol{x}_{n+1} = \boldsymbol{\Phi}_T(\boldsymbol{x}_n), \tag{2.4}$$

translating the continuous flow $\boldsymbol{\Phi}_t$ into the discrete mapping $\boldsymbol{\Phi}_T$. The sequence

$$\boldsymbol{X}_n(\boldsymbol{x}_0) = [\boldsymbol{x}_0, \boldsymbol{x}_1, ..., \boldsymbol{x}_n], \tag{2.5}$$

contains the subsequent tracer positions at the discrete time levels $t = [0, T, ..., nT]$ and forms the temporal *Poincaré section* (or stroboscopic map) of the Lagrangian tracer trajectory $\boldsymbol{X}_t(\boldsymbol{x}_0)$. In this report only n-step time-periodic systems of the form

$$\boldsymbol{\Phi}_T = \boldsymbol{F}_n \boldsymbol{F}_{n-1} ... \boldsymbol{F}_1, \tag{2.6}$$

[1] This chapter is a slightly adapted version of chapter 2 of the thesis of Speetjens (2001).

will be considered. The steps $\boldsymbol{F}_i$ form the piecewise steady forcing stages, during which the endwalls perform a steady translation, acting upon the fluid during the time interval $t = [(i-1)T/n, iT/n]$.

An important flow property is given by Liouville's theorem

$$\frac{dV}{dt} = \int_{V(t)} \nabla \cdot u dv, \tag{2.7}$$

which implies that a incompressible flow (conservative system) is volume-preserving.

Chaotic tracer motion forms an important issue for the present study. A general hallmark of chaos is the extreme sensitivity to its initial conditions. Consider a separation $\epsilon = \boldsymbol{x}^{(2)} - \boldsymbol{x}^{(1)}$ between two tracers $\boldsymbol{x}^{(1)}$ and $\boldsymbol{x}^{(2)}$ and introduce the Lyapunov exponents

$$\lambda_i(t) = \frac{1}{t} \ln[\frac{\epsilon_i(t)}{\epsilon_i(0)}], \qquad \epsilon_i(0) \to 0, \qquad\qquad i = 1,2,3, \tag{2.8}$$

quantifying the temporal evolution of the separation $\epsilon = (\epsilon_1, \epsilon_2, \epsilon_3)$. Positive Lyapunov exponents reflect exponential separation as time progresses and imply minute uncertainties in the initial conditions grow to dramatic proportions in course of time.

2.2 Governing equations

The $3D$ flow field is governed by the classical conservation laws of mass (continuity equation) and momentum (Navier-Stokes equation). In the incompressible case the conservation of mass and the Navier-Stokes equation are given by

$$\nabla \cdot \boldsymbol{u} = 0, \qquad \frac{\partial \boldsymbol{u}}{\partial t} + \boldsymbol{u} \cdot \nabla \boldsymbol{u} = -\frac{1}{\rho} \nabla p + \nu \nabla^2 \boldsymbol{u}, \tag{2.9}$$

with ρ the constant density, ν the kinematic viscosity and p the pressure. The initial and boundary conditions are given by

$$\boldsymbol{u}|_{t=0} = \boldsymbol{u}_0, \qquad \boldsymbol{u}|_\Gamma = \boldsymbol{U}(\boldsymbol{u}|_\Gamma, t), \tag{2.10}$$

with $\boldsymbol{U}$ the no-slip velocity on the rigid boundary $\Gamma = \partial\mathbb{D}$. These equations describe the fluid flow in the entire $3D$ cylindrical domain $\mathbb{D} : [r, \theta, z] = [0, R] \times [0, 2\pi] \times [-\frac{H}{2}, \frac{H}{2}]$. A schematic representation of the cylindrical domain is given in figure 2.1, wherein R and H signify the dimensions of the cylinder and the arrows indicate the in-plane motion of the endwalls at velocity $\boldsymbol{U}$.

2.3 Dimensional Analysis

In order to create a non-dimensional form of the Navier-Stokes equation, a magnitude assessment has to be carried out for each individual contribution. This results in

$$\frac{\partial \boldsymbol{u}}{\partial t} \sim \frac{U}{T^*}, \qquad \boldsymbol{u} \cdot \nabla \boldsymbol{u} \sim \frac{U^2}{R}, \qquad \frac{1}{\rho} \nabla p \sim \frac{P}{\rho R}, \qquad \nu \nabla^2 \boldsymbol{u} \sim \frac{\nu U}{H^2}, \tag{2.11}$$

for the particular case of translating endwalls, with the time scale T^* and the pressure scale P momentarily left unspecified. Application of (2.11) to the Navier-Stokes equation of (2.9) leads to the non-dimensional form

$$Sr \, \frac{\partial \widetilde{\boldsymbol{u}}}{\partial \widetilde{t}} + Re \, \widetilde{\boldsymbol{u}} \cdot \widetilde{\nabla} \widetilde{\boldsymbol{u}} = -\widetilde{\nabla} \widetilde{p} + \widetilde{\nabla}^2 \widetilde{\boldsymbol{u}}, \tag{2.12}$$

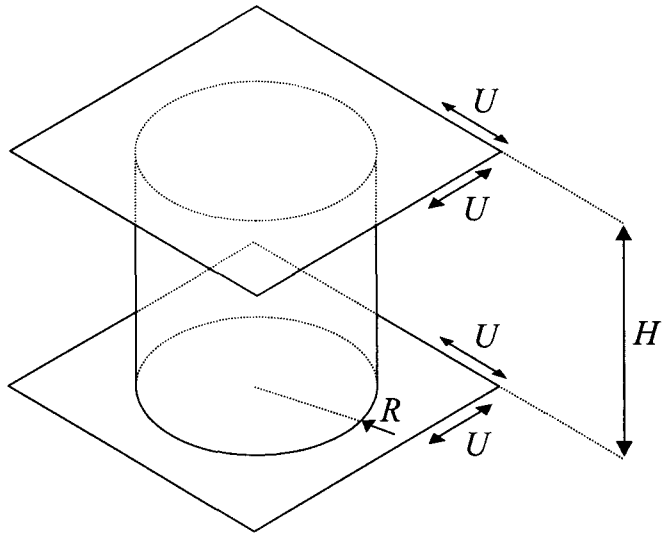

Figure 2.1: A schematic representation of the cylindrical domain and the forcing method.

relative to the unit cylinder $\widetilde{\mathbb{D}} : [\widetilde{r}, \widetilde{\theta}, \widetilde{z}] = [0,1] \times [0, 2\pi] \times [-1, 1]$. In what follows the tildes indicating non-dimensionality are dropped in favor of clarity. The pressure scale $P = \rho\nu UR/H^2$ follows from the presumed dominance of viscous over inertial forces, which dictates a (near) balance between the pressure gradient and the diffusion term. The non-dimensional parameters are

$$Re = \frac{UH^2}{\nu R}, \qquad Sr = \frac{H^2}{\nu T^*}, \qquad D_1 = \frac{H}{R}, \qquad D_2 = \frac{UT}{nR}, \tag{2.13}$$

with Re the Reynolds number and Sr the Strouhal number as dynamical parameters. D_1 and D_2 are the geometrical parameters. D_1 is the aspect ratio, which will be held fixed during this report and is set to $D_1 = 2$, making the cylinder height H equal to the cylinder diameter $2R$. D_2 reflects the dimensionless displacement of an endwall, during steady forcing ($n = 1$) or during one stage of a n-step time periodic forcing ($n > 1$), with T the global forcing time scale. Two characteristic time scales T^* can be deduced from the Navier-Stokes equation (2.9), namely the advection time scale $T_a = R/U$ and the viscous time scale $T_\nu = H^2/\nu$. Given the restriction to viscous flows, unsteady flow phenomena scale with T_ν and result in $T^* = T_\nu$ as a characteristic time scale, see Telionis (1981). Consequentially, $Sr = 1$ and the Navier-Stokes equation (2.12) becomes

$$\frac{\partial \boldsymbol{u}}{\partial t} + Re\ \boldsymbol{u} \cdot \nabla \boldsymbol{u} = -\nabla p + \nabla^2 \boldsymbol{u}, \tag{2.14}$$

implying that Re is the only remaining dynamical parameter. The fluid is agitated by (a sequence of) steady translation(s) of an endwall, therefore the essential fluid dynamical problem comes down to the response of a stagnant fluid to an impulsive start-up (initial acceleration or an intermediate change of direction of the motion of a moving endwall). The unsteady term from the initial acceleration decays exponentially in the course of time, causing the flow to reach a steady state at $t \simeq 1$. For $t \geq 1$ the dimensionless Navier-Stokes equation (2.14) can be further reduced to

$$Re\ \boldsymbol{u} \cdot \nabla \boldsymbol{u} = -\nabla p + \nabla^2 \boldsymbol{u}. \tag{2.15}$$

To show the relative share of start-up effects during the forcing process an alternative Strouhal number can be introduced

$$Sr_f = \frac{nT_\nu}{T}, \tag{2.16}$$

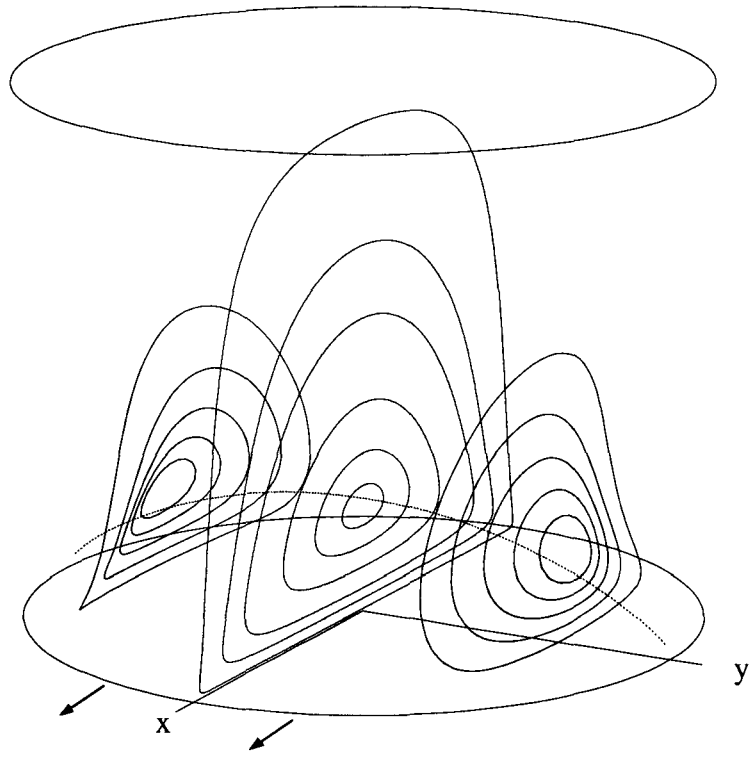

Figure 2.2: The primary eddy structure of the steady flow is shown. The dashed line represents the stagnation line belonging to the primary eddy.

relating the viscous time scale to the global time scale for a n-step. Using the last equation on the regime $Sr_f \ll 1$, putting forth

$$Re\ \boldsymbol{u} \cdot \nabla \boldsymbol{u} = -\nabla p + \nabla^2 \boldsymbol{u}, \qquad \nabla \cdot \boldsymbol{u} = 0, \qquad \boldsymbol{u}|_\Gamma = \boldsymbol{U}(\boldsymbol{u}|_\Gamma, t), \tag{2.17}$$

as governing flow model holding this report. Re and D_2 can be seen as only parameters associated with (2.17). Non-linear effects can enter the flow field exclusively through the inertial term $\boldsymbol{u}.\nabla \boldsymbol{u}$ and the boundary condition $\boldsymbol{U}$. The assumption $Sr_f \ll 1$ makes the viscous time scale T_ν insignificant, see equation (2.16) This leaves the advective time scale $T_a = R/U$ and the global period time scale T as only relevant time scales. These two time scales are related via the non-dimensional displacement parameter D_2 and n on the following way

$$\frac{T}{T_a} = nD_2. \tag{2.18}$$

This makes the advective time scale T_a the principal time scale.

2.4 Periodic structures

A material point $\boldsymbol{x}$, such that $\boldsymbol{u}(\boldsymbol{x})= 0$ for all t, is called a stagnation point. An illustrative example is the steady flow in a cylindrical volume, where the fluid contains a complete stagnation line, see figure 2.2. This figure gives a $3D$ impression of the streamlines in the primary eddy structure too. From now on a time periodic forcing protocol will be assumed of the form given by equation (2.6) with T the global period time. A periodic point $\boldsymbol{x}_0^{(k)}$ is a material point returning to its initial position after k cycles. If $k = 1$ the point will remain fixed in the mapping portrait $\boldsymbol{X}_n(\boldsymbol{x}_0)$. For $k > 1$ one finds the period-k point wandering along the k locations $\boldsymbol{\Phi}_T^i(\boldsymbol{x}_0^{(k)})$, with $0 \leq i \leq k-1$,

prior to returning to the initial position. A material point released on *any* of these intermediate points follows this path, k-th order periodic structures invariably emerge as clusters

$$\boldsymbol{\chi}_0^{(k)} = [\boldsymbol{x}_0^{(k)}, \boldsymbol{\Phi}_T(\boldsymbol{x}_0^{(k)}), \boldsymbol{\Phi}_T^2(\boldsymbol{x}_0^{(k)}), ..., \boldsymbol{\Phi}_T^{k-1}(\boldsymbol{x}_0^{(k)})], \tag{2.19}$$

with root $\boldsymbol{x}_0^{(k)}$. Mostly one is interested in relatively fast mixing protocols, therefore the time periodic-1 lines (points) are often studied only.

The behavior of a periodic point can be investigated by doing analysis on infinitesimally close neighbouring points. A neighbouring point $\boldsymbol{x}_0^{(k)} + d\boldsymbol{x}_0$ arrives after k periods at $\boldsymbol{x}_0^{(k)} + d\boldsymbol{x}_k = \boldsymbol{\Phi}_T^k(\boldsymbol{x}_0^{(k)} + d\boldsymbol{x}_0)$. Linearization about the point $\boldsymbol{x}_0^{(k)} = \boldsymbol{\Phi}_T^k(\boldsymbol{x}_0^{(k)})$ adds up to

$$d\boldsymbol{x}_k = \boldsymbol{F} d\boldsymbol{x}_0, \tag{2.20}$$

with $\boldsymbol{F} = \partial\boldsymbol{\Phi}_T/\partial\boldsymbol{x}|_{\boldsymbol{x}_0^{(k)}}$the Jacobian matrix, or alternatively, deformation tensor. Analysis of the eigenvalue spectrum of F, for a $3D$ flow, leads to a third order characteristic polynomial with three eigenvalues. At least one of these eigenvalues is positive and real, because of the incompressibility constraint $\lambda_1\lambda_2\lambda_3 = 1$. A further analysis leads to nine regimes, depending on the three eigenvalues, see Speetjens (2001).

A special class forms $\lambda_1 = 1$ signifying the absence of stretching and compression in a certain direction n_1. This behavior is typical for periodic lines, on which n_1 aligns with the tangent vector of the periodic line. One can distinguish elliptic (λ_2 and λ_3 are complex), parabolic ($\lambda_2 = \lambda_3 = 1$) and hyperbolic (λ_2 and λ_3 real, with one, say λ_2 larger than 1 and $\lambda_3 = 1/\lambda_2$) points, representing the behavior of neighbouring points. Fluid in the neighbourhood of individual periodic points with $\lambda_1 = 1$, behaves locally essentially $2D$ and adopts the classification proposed for $2D$ systems, see Ottino (1989). Hyperbolic points have $\lambda_2 > 1$, making chaotic motion possible in the region of the hyperbolic points as defined by equation (2.8).

The behavior in the neighbourhood of a periodic line is thus essentially $2D$, however quasi $3D$ effects exist in that elliptic and hyperbolic segments can be smoothly connected via parabolic points.

2.5 Symmetries

Searching for periodic structures is facilitated when symmetries are found. For the detection of these symmetries only gross knowledge of the velocity field is needed.

Trajectories $\boldsymbol{\Phi}_t(\boldsymbol{x}_0)$ can accommodate two types of symmetries, viz.

$$\boldsymbol{\Phi}_t = S\boldsymbol{\Phi}_t S^{-1}, \quad \boldsymbol{\Phi}_t = S\boldsymbol{\Phi}_t^{-1} S^{-1}, \tag{2.21}$$

ordinary reflectional symmetry and time-reversal reflectional symmetry, respectively, under operation of the symmetry operator S with respect to the fixed manifold of symmetry I_s,see figure 2.3. Note that for ordinary reflectional symmetries, the trajectories cannot cross I_s, because of the following reasoning: assume a particle is moving from left to right with velocity U, this corresponds to a mirror particle moving from right to left with velocity $-U$, making the velocity of a particle residing on I_s ambivalent, which is against the assumption of a deterministic velocity field. Therefore, the symmetry plane I_s acts as a transport barrier in the case of ordinary reflectional symmetry. For time-reversal reflectional symmetry there is no such a restriction. When a bounded flow has a time-reversal symmetry, it always hosts a stagnation or a periodic line, see Speetjens (2001).

For time-periodic systems, thus where equation (2.6) holds, a second class of symmetries exists

$$\boldsymbol{F}_i = S\boldsymbol{F}_j S^{-1}, \quad \boldsymbol{F}_i = S\boldsymbol{F}_j^{-1} S^{-1}, \tag{2.22}$$

reflecting the same kind of symmetries, but now for each individual stage of the forcing sequence. This tool simplifies searching for possible global symmetries considerably. Possible symmetries can be derived directly, using the symmetries of the subsequent steps $\boldsymbol{F}_i$. For $i = j$ relation (2.22) denotes self-symmetry within one single step $\boldsymbol{F}_i$.

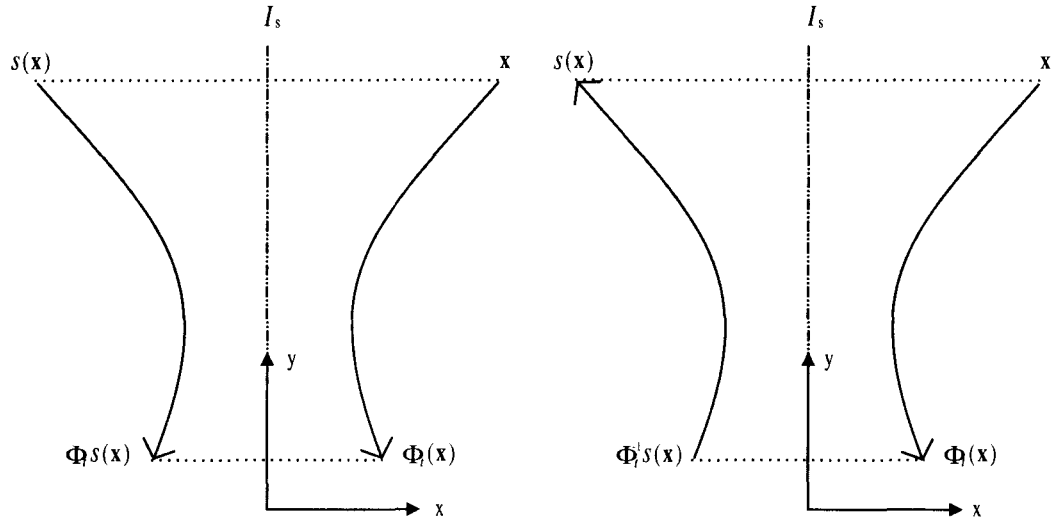

Figure 2.3: Ordinary reflectional symmetry (*left*) and time-reversal reflectional symmetry (*right*).

Chapter 3

Flow Analysis

In the thesis of Speetjens (2001) a thorough analysis of steady flow and of the three forcing protocols (denoted by A, B and C) can be found. One can roughly say that these protocols show an increasing level of chaotic behavior, respectively, which can basically understood by arguments of symmetry, these forcing protocols show a decreasing grade of symmetry level,respectively.

The steady flow will be introduced in section 3.1, because of its relevance as basic building block. The protocols A, B and C are all non-repetitive, which means that the cylinder endwalls do not return to their initial positions, after a global time period T. Therefore a new protocol, the four-step protocol D, will be introduced in the section 3.2. The net zero displacement of the endwalls of this protocol D is important, for studying long-time effects in the experiments.

3.1 Steady flow as a basic building block

Start up and slow down effects are neglected in this chapter under assumption of $Sr_f \ll 1$, which implies that the governing flow model given by equation (2.17) holds. $Sr_f \ll 1$ is a rather exotic assumption, because it implies that the velocity field reacts directly upon the forcing: if an imposed forcing changes, the velocity field will *jump* instantaneously to the velocity field belonging to the newly imposed forcing. Furthermore, we will focus on the non-inertial limit $Re = 0$, which makes the Navier-Stokes equation a linear problem. This assumption leads to the following piecewise steady Stokes equation as the governing flow model

$$\nabla p = \nabla^2 \boldsymbol{u}, \qquad \nabla \cdot \boldsymbol{u} = 0 \qquad \boldsymbol{u}|_\Gamma = \boldsymbol{U}(\boldsymbol{u}|_\Gamma, t). \tag{3.1}$$

This leaves the dimensionless displacement D_2 as the only parameter, meaning that in the Stokes limit the flow entirely depends on this parameter D_2 and its boundary condition. To specify the boundary condition, forcing steps of the specified form given in equation (2.6) are used and will replace the boundary condition of equation 3.1. In the forthcoming analysis, the subsequent steps $\boldsymbol{\Phi}_i$ composing forcing protocol (2.6), are assumed either of the forms

$$\boldsymbol{F}_B^{(\pm x)}, \qquad \boldsymbol{F}_B^{(\pm y)}, \qquad ,\boldsymbol{F}_T^{(\pm x)}, \tag{3.2}$$

with the subscripts T and B signifying the top ($z = 1$) and bottom ($z = -1$) endwall, respectively, performing a translation with velocity $U = 1$ in the indicated coordinate direction ($+x$, $-x$, $+y$ or $-y$).

The steady flow is described by:

$$\boldsymbol{\Phi}_T = \boldsymbol{F}_B^{(+x)}, \tag{3.3}$$

containing one single forcing step with T as global total forcing time.

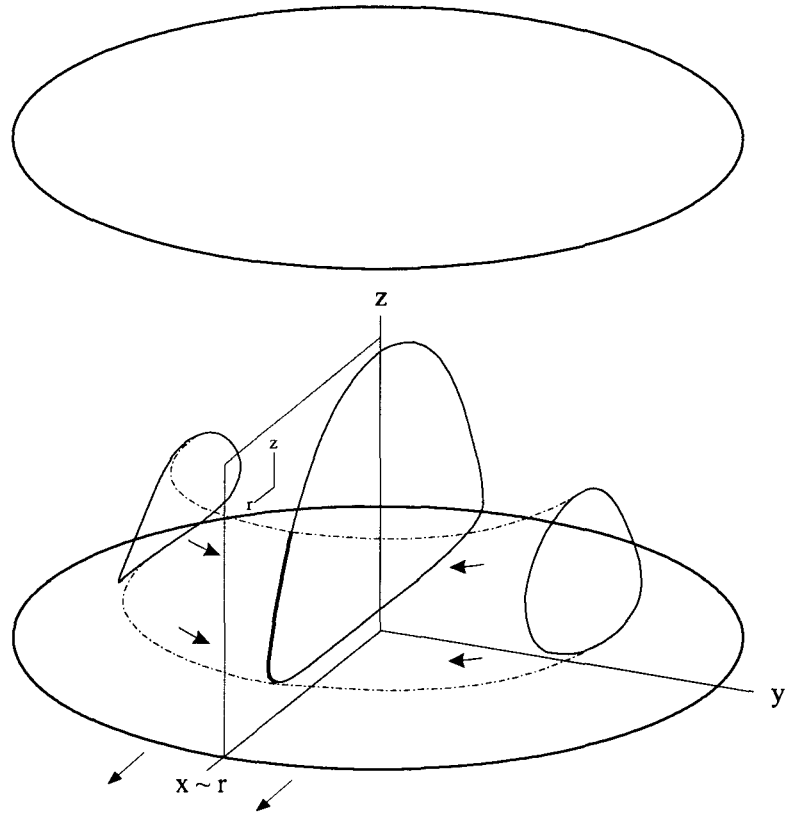

Figure 3.1: Visualisation of the rz-projection, holding for $Re = 0$ only.

Under the steady forcing condition (3.3), there exists an analytical solution of the Stokes equation (3.1), which is given by Shankar (1997). The solution is assumed to be of the form

$$u_r(\boldsymbol{x}) = u_r(r,z)\cos\theta, \quad u_\theta(\boldsymbol{x}) = u_\theta(r,z)\sin\theta, \quad u_z(\boldsymbol{x}) = u_z(r,z)\cos\theta, \tag{3.4}$$

defining the velocity field with closed streamlines $\boldsymbol{X}_t(\boldsymbol{x}_0)$ symmetrically arranged about the plane $y = 0$ and exhibiting self-symmetry about $x = 0$. When performing a numerical simulation it would mean that, in the spectral space, $m = 1$ is the only azimuthal mode giving a contribution to the solution. A special property of this steady Stokes flow is, that the projection of arbitrary $3D$ streamlines in the rz-plane coincides with streamlines in the plane $y = 0$. This is not just a normal Cartesian projection, but a projection in cylindrical coordinates, which eliminates θ. It is just like the projection you can imagine when you are closing a book, see figure 3.1. The left and the right closed loops (symmetric with respect to the plane $y = 0$), shown in figure 3.1, are projected on the same line segment in the plane $y = 0$, where the line segment itself forms a part of a closed streamline in the plane $y = 0$.

In the steady flow case most phenomena can be found in the plane $y = 0$, due to the possibility of this rz-projection when $Re = 0$, making the plane $y = 0$ a very interesting one. The streamline pattern of this plane is shown in figure 3.2. The heavy line separates two distinct regions, the largest inner part is called the primary eddy and the smaller outer part, left and right on top is called the secondary eddy. The impact of the secondary eddy grows substantially, when using higher aspect ratios. For example when $D_1 = 4$, the secondary eddy is transformed into a counter rotating primary eddy. Increasing the aspect ratio further will lead to even more counter rotating eddies, see Shankar (2000). In this report $D_1 = 2$, so the secondary eddy plays a minor role and not so much attention will be paid to it.

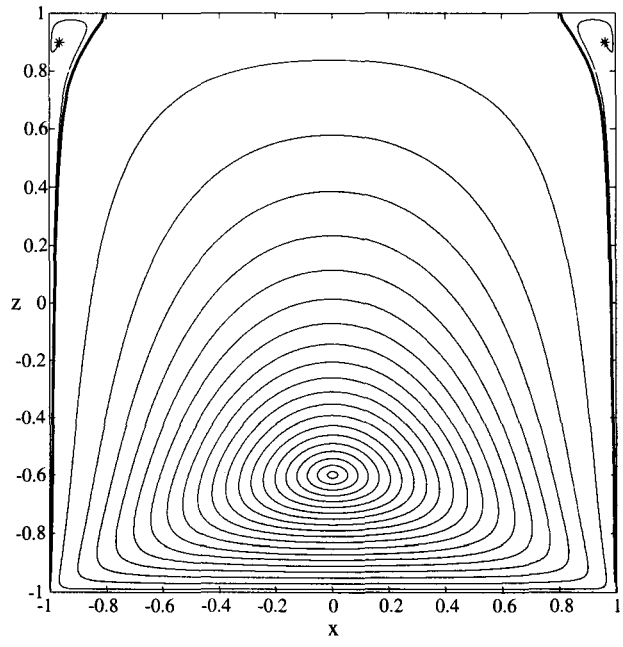

Figure 3.2: Closed streamlines (particle trajectories) in the plane $y = 0$. When $Re = 0$, the rz-projection of all streamlines in three dimensions coincide with these streamlines.

3.2 Protocol D

The protocols A,B and C introduced by Speetjens are represented in figure 3.3. All these protocols

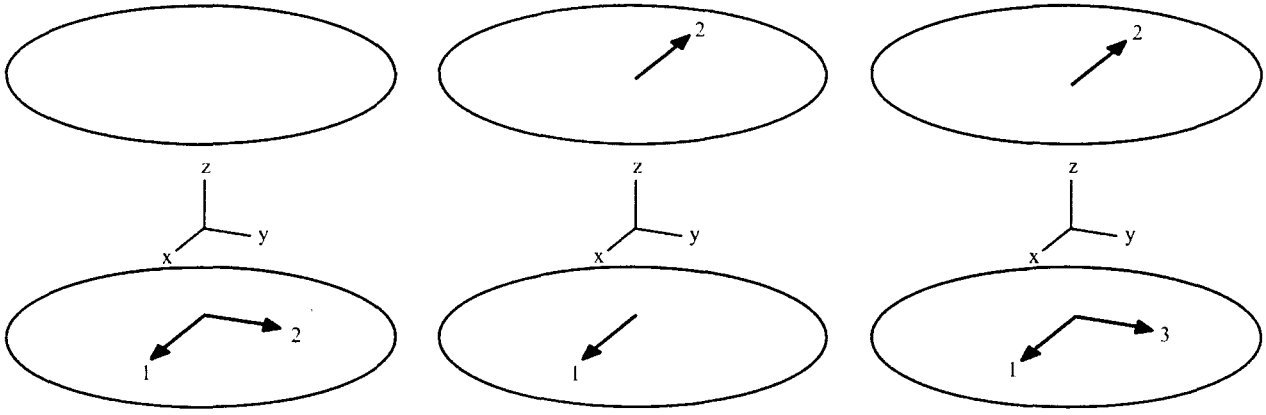

Figure 3.3: A representation of the forcing protocols A, B and C introduced by Speetjens. The numbers indicating the successive steps.

have in common, that their endwalls will not return to the initial positions after a complete forcing cycle. These protocols are said to be non-repetitive. Repetitiveness of a protocol is needed to be able to do long-time experiments. This is because an endwall can move only a finite distance in a certain direction, in the current experimental set-up, that distance is 21 cm. When one likes to measure longer than one global period time T, then a net zero displacement after a global period time T is a restriction. To overcome this problem the repetitive four-step protocol D will be introduced.

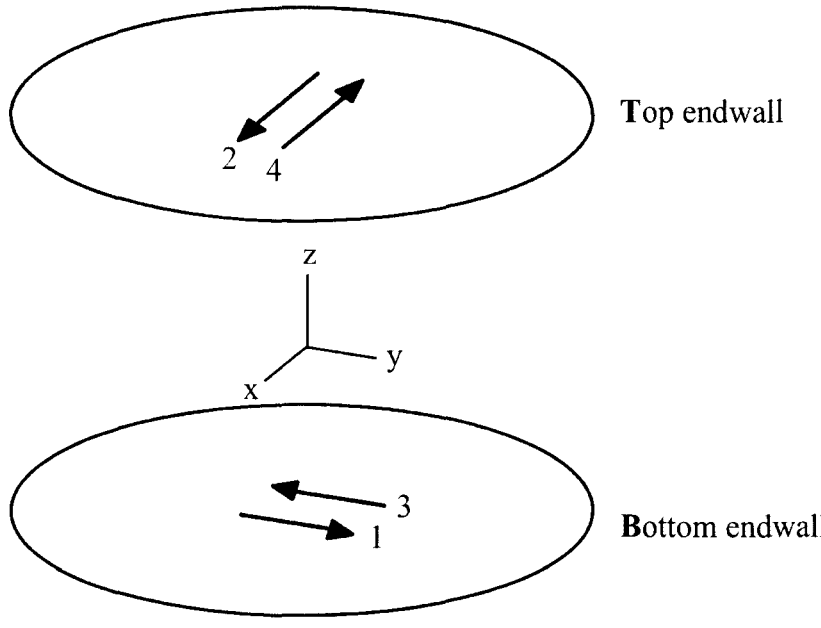

Figure 3.4: A representation of the four-step forcing protocol D, where the numbers representing the successive steps. After each completed cycle the endwalls are back in their initial positions.

This four-step forcing protocol D is described by

$$\boldsymbol{\Phi}_T = \boldsymbol{F}_4\boldsymbol{F}_3\boldsymbol{F}_2\boldsymbol{F}_1 : \quad \boldsymbol{F}_4 = \boldsymbol{F}_T^{(-x)}, \quad \boldsymbol{F}_3 = \boldsymbol{F}_B^{(-y)}, \quad \boldsymbol{F}_2 = \boldsymbol{F}_T^{(+x)}, \quad \boldsymbol{F}_1 = \boldsymbol{F}_B^{(+y)}. \tag{3.5}$$

The choice of present order of forcing, facilitates a direct comparison with the work by Anderson (1999), who applied the same forcing protocol to study mixing in a cubic domain. The comparison self will be pursued in chapter 4, which is about the numerical investigation of protocol D. A graphical representation of the forcing of protocol D is given in figure 3.4.

Protocol D is one of most plain non-trivial repetitive forcing protocols. This protocol exhibits some symmetries, which can lead to periodic structures (periodic lines). Mixing near periodic lines is locally effectively $2D$, meaning that the overall mixing will be not very efficient. A six-step protocol could easily resolve such a problem. A measurement directly applied to a six-step forcing protocol would be to complicated, because experiments till thus far did no go beyond the steady flow case. Protocol D is chosen, because it is repetitive, relatively simple and not so long that no particles can be followed a complete forcing cycle.

An analytically obtained symmetry, enhancing the search for periodic structures, will be deduced here. The basic idea is trying to find one or more global symmetries by exploiting the symmetries on each individual stage, as defined in the section 2.5. Each individual forcing step can be expressed in one single forcing step by adding symmetry operators. The following three symmetry operators S_{xy}, S_z, $\widetilde{S}$ are introduced:

$$S_{xy}(x, y, z) = (y, x, z), \tag{3.6}$$

$$S_z(x, y, z) = (x, y, -z), \tag{3.7}$$

$$\widetilde{S} = S_z S_{xy}. \tag{3.8}$$

The symmetry operator S_{xy} establishes reflection about the plane $y = x$. The symmetry operator S_z establishes reflection about the plane $z = 0$. $\widetilde{S}$ describes a rotation by 180^0, i.e. axial symmetry,

around the line defined by $L_s = \{x - y = 0\} \cap \{z = 0\}$, which can also be seen as just a reflection about that specific line. All three symmetry operators meet $S^2 = I$. The four forcing steps are expressed in terms of $\boldsymbol{F}$ and $\widetilde{S}$ by

$$\boldsymbol{F}_1 = \boldsymbol{F}, \qquad \boldsymbol{F}_3 = \boldsymbol{F}^{-1}, \tag{3.9}$$

$$\boldsymbol{F}_2 = \widetilde{S}\boldsymbol{F}\widetilde{S}, \qquad \boldsymbol{F}_4 = \boldsymbol{F}_2^{-1} = \widetilde{S}\boldsymbol{F}^{-1}\widetilde{S}. \tag{3.10}$$

Substitution of the relations (3.9) and (3.10) into equation (3.5) give

$$\boldsymbol{\Phi}_T = \widetilde{S}\boldsymbol{F}^{-1}\widetilde{S}\boldsymbol{F}^{-1}\widetilde{S}\boldsymbol{F}\widetilde{S}\boldsymbol{F}. \tag{3.11}$$

The inverse of the four-step forcing protocol D looks as follows (operators are rewritten in reverse order and replaced by their inverses, taking into account that $\widetilde{S} = \widetilde{S}^{-1}$)

$$\boldsymbol{\Phi}_T^{-1} = \boldsymbol{F}^{-1}\widetilde{S}\boldsymbol{F}^{-1}\widetilde{S}\boldsymbol{F}\widetilde{S}\boldsymbol{F}\widetilde{S}. \tag{3.12}$$

From equations (3.11) and (3.12) it follows that the protocol $\boldsymbol{\Phi}_T$ and its inverse $\boldsymbol{\Phi}_T^{-1}$ possess the following symmetry relation

$$\boldsymbol{\Phi}_T = \widetilde{S}\boldsymbol{\Phi}_T^{-1}\widetilde{S}. \tag{3.13}$$

This equation shows the global time-reversal reflectional symmetry of protocol D under operation of the symmetry operator $\widetilde{S}$, corresponding to equation (2.21).[1] According to Speetjens, there must be a periodic line, because of the found time-reversal reflectional symmetry. The search for periodic lines can be reduced to half the domain (e.g. $z \leq 0$ or $z \geq 0$), because when (a, b, c) is a periodic point, then $(b, a, -c)$ is a periodic point too, by applying the symmetry operator $\widetilde{S}$. When using the induction principle the following even stronger argument can be found: periodic structures of *any* order should be arranged symmetrically around L_s, see Anderson (1999).

[1] There are more symmetries found, these are described in appendix C.

Chapter 4

Numerical Analysis of Protocol D

In this chapter results of the numeric analysis of Protocol D are represented. Section 4.1 handles non-inertial flows ($Re = 0$) and therefore the analytical solution of Shankar can be applied on each single forcing step. In section 4.2 some effects of inertial flows ($Re > 0$) are shown.

4.1 Non-Inertial Flows

For $Re = 0$ the only remaining parameter is the dimensionless displacement, which is set to $D_2 = 5$ in this chapter. Periodic-1 lines of protocol D are found, by searching for the minima of the displacement functions through the domain, as proposed by Speetjens (2001). This displacement function is defined by $||\boldsymbol{x}(T) - \boldsymbol{x}(0)||$. Searching can be reduced to half the domain by exploiting the time reversal symmetry $\widetilde{S}$. The found periodic-1 lines can be compared to the periodic-1 lines Anderson found in his cubic domain, wherein he applied the same forcing, see Anderson (1999)[1]. Even the dimensionless displacement parameter $D_2 = 5$ is the same, which makes a direct

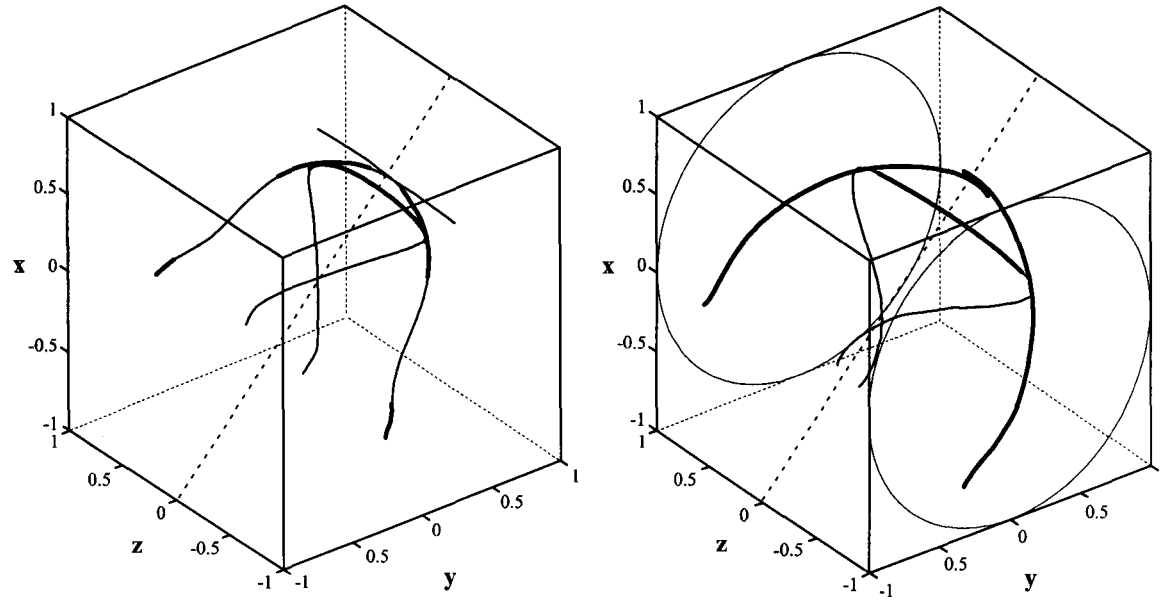

Figure 4.1: The periodic-1 lines of forcing protocol D in a cubic domain (left) of Anderson compared to the found periodic-1 lines in the cylindrical domain (right). The dashed line denotes the axis of symmetry. Elliptic line segments are represented by thick line segments and the hyperbolic line segments are represented by thin line segments.

[1] Anderson used shifted coordinates (z,x,y) in his cubic domain.

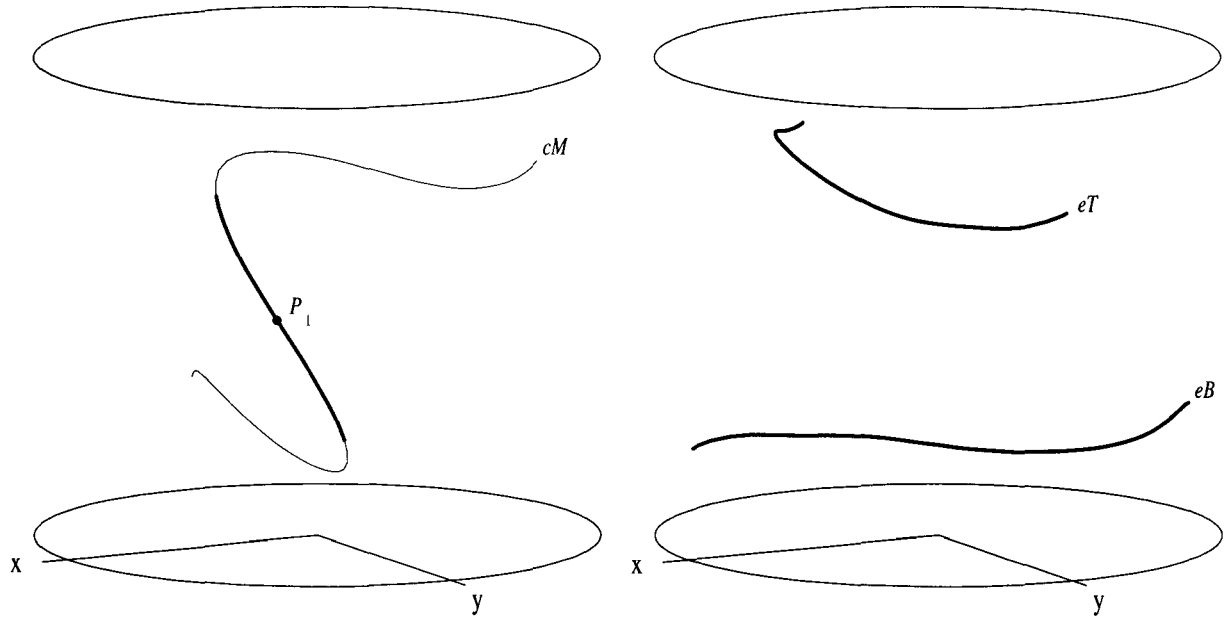

Figure 4.2: The midpoint P_1 on the line cM (left) is crossing the axis of symmetry. The lower part of the line cM is oriented in the y-direction, while the top is oriented in x-direction. The elliptic line eT (right) aligned in the direction of the y-axis. The elliptic line eB (right) is directed in the direction of the x-axis.

comparison possible. This comparison has been made in figure 4.1. The form of the numerical obtained period-1 lines in the cylindrical domain is somewhat rounder compared to the more angular periodic-1 lines in the cubic domain. This is caused by the influence of the different boundaries. In the cylindrical domain two complete elliptic lines are found, while these lines in the cubic domain have hyperbolic regions. The reason is, that the cylinder mantle is much smoother than the corners of the cubic domain and therefore the fluid flow will be less chaotic in the cylindrical domain.

In figure 4.2 the periodic-1 lines found in the cylindrical domain are represented once again, but now in a better perspective. The central periodic line (cM) is shown on the left panel. The elliptic bottom line (eB) and the elliptic top line (eT) are shown on the right panel. The middle of the cM line crosses the line of symmetry L_s in the elliptic point $\mathrm{P}_1 = (0.3463, 0.3463, 0)$. The upper part of the line cM can be seen as a 180^0 rotated lower part of line cM along the line of symmetry L_s, which can be regarded as a kind of self-symmetry. eB is equal to the 180^0 rotated eT along the line of symmetry L_s. The end points of eB and eT end on the cylinder mantle as parabolic points. These parabolic points are in this case even stagnation (fixed) points.

In total 81 periodic tracers on cM and 43 tracers on eB and eT each, are followed during a complete forcing cycle. The tracer trajectories are represented in figure 4.3. It can easily be seen, that definitely more symmetry can be found, than described in section 3.2. In the left figure tracer trajectories attached to cM are symmetrical in the planes $x = 0$ and $y = 0$. The volume formed by all trajectories together is symmetrical in both planes too. In the top region and in the bottom region clearly longer tracer trajectories are seen than in the centre region, reflecting the hyperbolic and the elliptic regions, respectively. On the right panel tracer trajectories connected to eT and eB are symmetrical in the plane $x = 0$ and $y = 0$, respectively. When mirror tracer trajectories are thought reflected in the planes $y = 0$ and $x = 0$ connected to eT and eB, respectively, then eB and eT are double symmetric too. These mirror tracers follow their trajectories in a reversed direction. It can be concluded that all these tracer trajectories exhibit the time-reversal reflectional symmetry, most of the tracer trajectories are even self-symmetrical. Both planes $x = 0$ and $y = 0$ are planes of time-reversal reflectional symmetry. By using the time-reversal symmetries of the

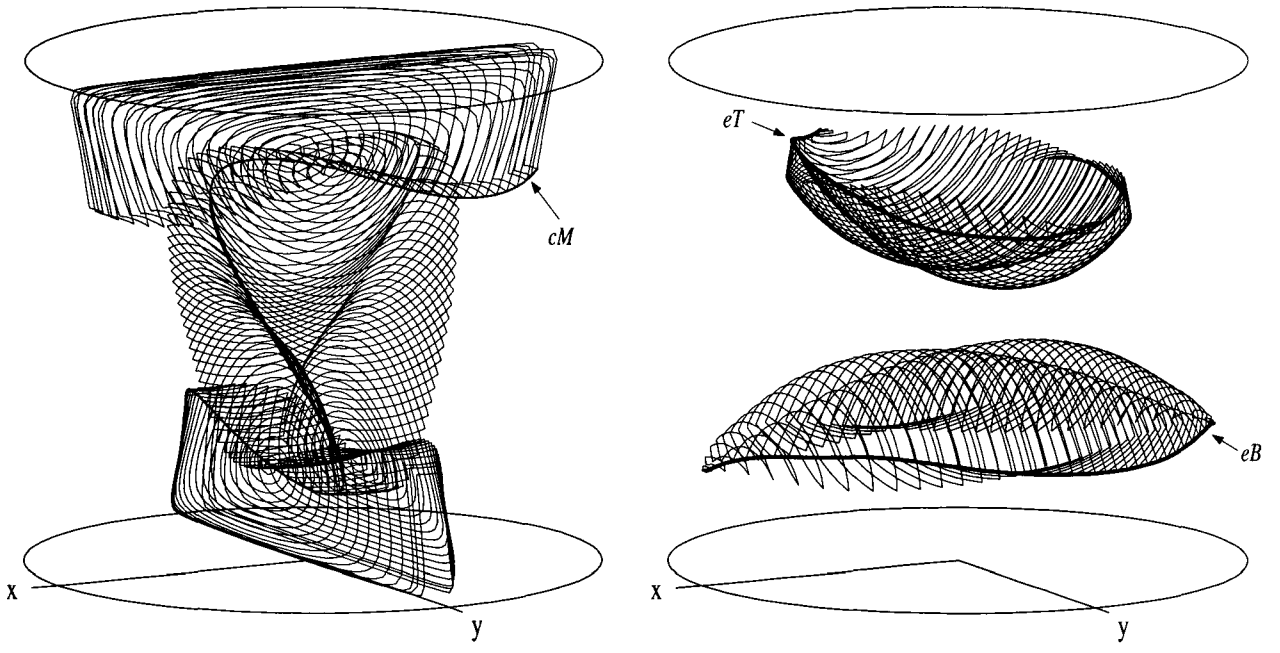

Figure 4.3: Passive tracers released on the periodic-1 lines followed one complete forcing cycle of protocol D. cM (left) indicates the central periodic line. eT and eB (right) indicate the elliptic lines. Symmetries are found in the planes $x = 0$ and $y = 0$.

planes $x = 0$ and $y = 0$, the periodic lines would have been found much more easily. Following one plane of symmetry half a period, would have been enough, instead of searching half the domain, see Speetjens (2001). Instead of using displacement function it would be possible to use the faster bi-section method, because searching takes place in a single plane.

Personal communication with Prof. V.V. Meleshko already led to the idea of following a periodic line segment and see where and how it is located at the specific times $t = 1/8T, 3/8T, 5/8T$ and $7/8T$, thus half away each forcing step. It appears that, at these specific times, the periodic lines are residing on a plane of symmetry as shown in figure 4.4. The symmetry plane at these specific times is always in the forcing direction of protocol D at that moment. Every next step of forcing protocol D implies a -90^0 rotated forcing direction and the other endwall is moving. In the symmetry this returns as follows: every next step correspond to rotation of -90^0 followed by reflection in $z = 0$. Thus every step later the periodic line is found on the other panel of figure 4.4 with on the horizontal axis ($y \rightarrow x$, $x \rightarrow -y$, $-y \rightarrow -x$ or $-x \rightarrow y$) and $z \rightarrow -z$ on the vertical axis.

Two spherical blobs, one put on a hyperbolic point and one on an elliptic point with radius $r/R = 0.1$, are followed two complete forcing cycles of protocol D. The advected blobs are shown for the times $t = 0$, $t = T$ and $t = 2T$, see figure 4.5. Relatively large stretching can be seen for the hyperbolic blob at $t = 2T$. The spherical blobs Speetjens released on hyperbolic points in his forcing Protocols A, B and C, all show more stretching after a global time period T, indicating that protocol D has inferior mixing properties. The largest eigenvalue is $\lambda = 4.31$ and resides on the unstable manifold of cM, while Speetjens found $\lambda = 13.8$ as a maximum in his protocol B. This also indicates the inferior stretching properties and thus probably having not that good mixing properties.

To say more about the mixing properties, a tracer particle has been released at a distance $r_0 = 10^{-3}$ from a hyperbolic point on eM with coordinates (0.1231,0.3912,-0.6500) and is followed over 10,000 global time periods T.

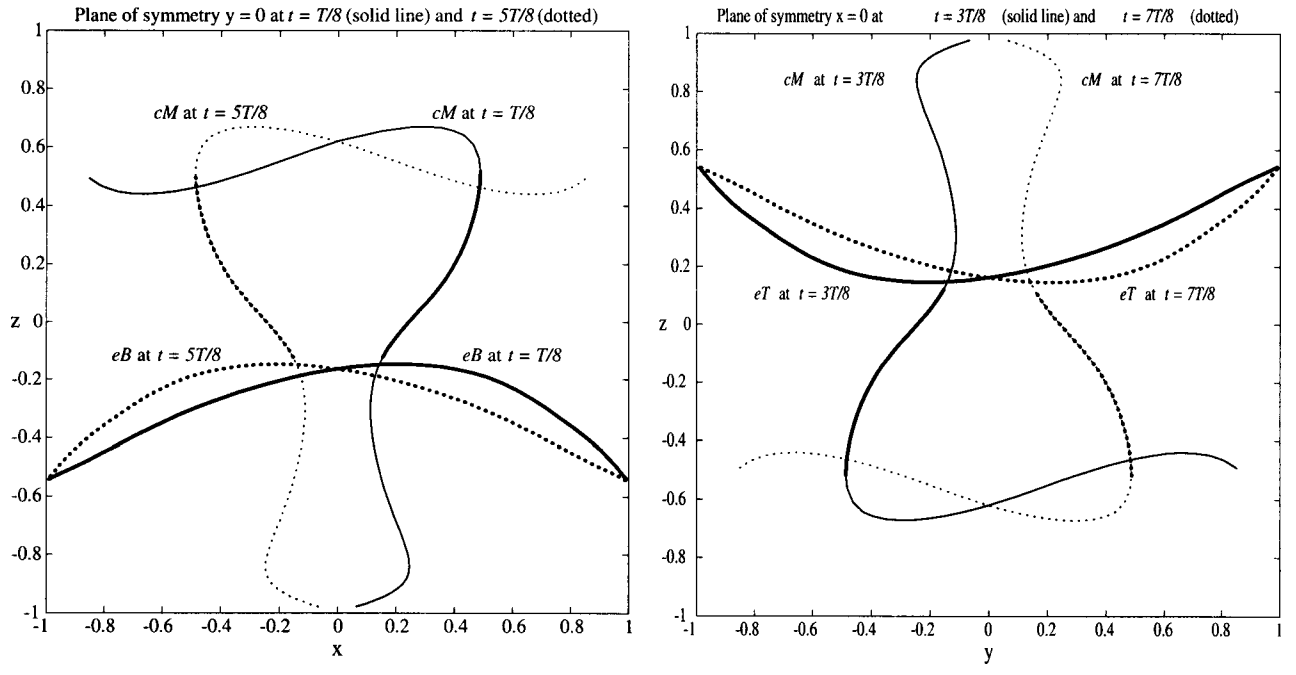

Figure 4.4: Symmetry planes $y = 0$ (left) and $x = 0$ (right) at specific times. Dashed lines are half a period later than the solid lines in the same plane of symmetry.

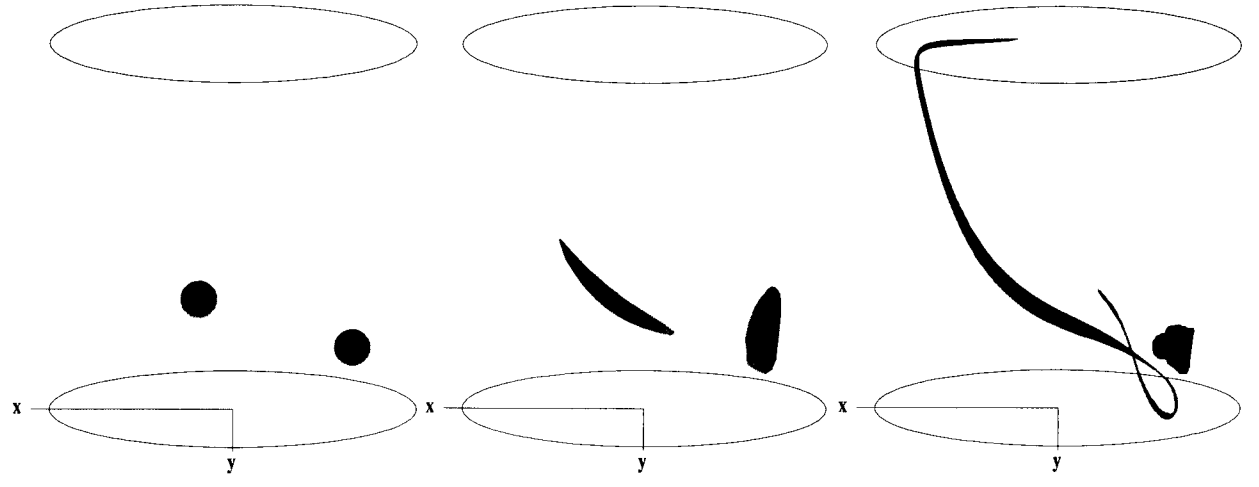

Figure 4.5: A blob released at a hyperbolic point (left) and a blob released in an elliptic point (right). The advected blobs are shown for $t = 0$, $t = T$ and $t = 2T$, respectively.

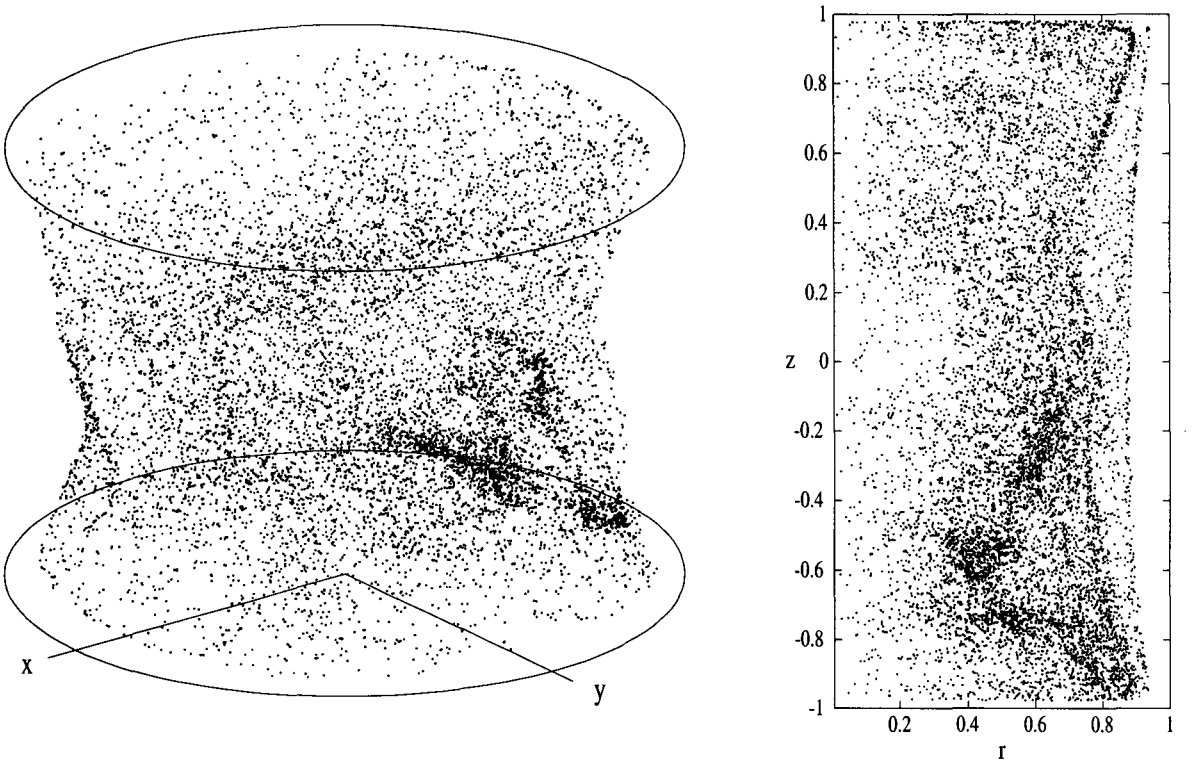

Figure 4.6: A tracer particle released close to a hyperbolic point followed over 10,000 global periods T. On the left plane a Poincaré section is shown for $Re = 0$. On the right plane the rz-projection is shown, with no points in the neighbourhood of the cylinder mantle.

The Poincaré map of this passive tracer is shown on the left panel of figure 4.6.[2] The tracer does not approach the cylinder mantle, which is better shown in the rz-projection, which is represented on the right panel of figure 4.6. It is clear that for $Re = 0$ the mixing near the cylinder mantle is not so efficient, when using protocol D.

4.2 Inertial Flows

In this section $Re = 0$ no longer holds, implying that the analytical solution of Shankar can not be used. Equation 2.17 will be used as a governing flow model, which is the (piecewise) stationary Navier-Stokes equation. A solution can only found by doing a numerical analysis. Speetjens wrote a spectral flow solver to tackle this problem. His method uses slightly different boundary conditions, making a quantitative comparison with the analytical results for $Re = 0$ not possible. Qualitatively seen all phenomena are the same making the simulations still useful. The boundary conditions in the spectral code are slightly different from the boundary conditions of the analytical solution, because only sufficient smooth continuous boundary conditions are allowed, while the analytical solution assumed a discontinuous velocity ring situated between the moving endwall and the cylinder mantle.

A tracer released near a hyperbolic point, when $Re = 0$, does not approach the cylinder mantle when using forcing protocol D. When $Re > 0$, thus by the introduction of an inertial force, it can be expected that the tracer gets closer to the cylinder mantle end thus enhances the mixing properties near the cylinder mantle. Introduction of the inertial force can often be seen as a kind of centrifugal force throwing particles outward. See for example the steady flow in Speetjens (2001),

[2] Recently it appeared, that this Poincaré map is quantitatively incorrect for the singular case $Re = 0$. This has no consequences, when replacing $Re = 0$ by $Re = 1$. The explanation is given in appendix C.

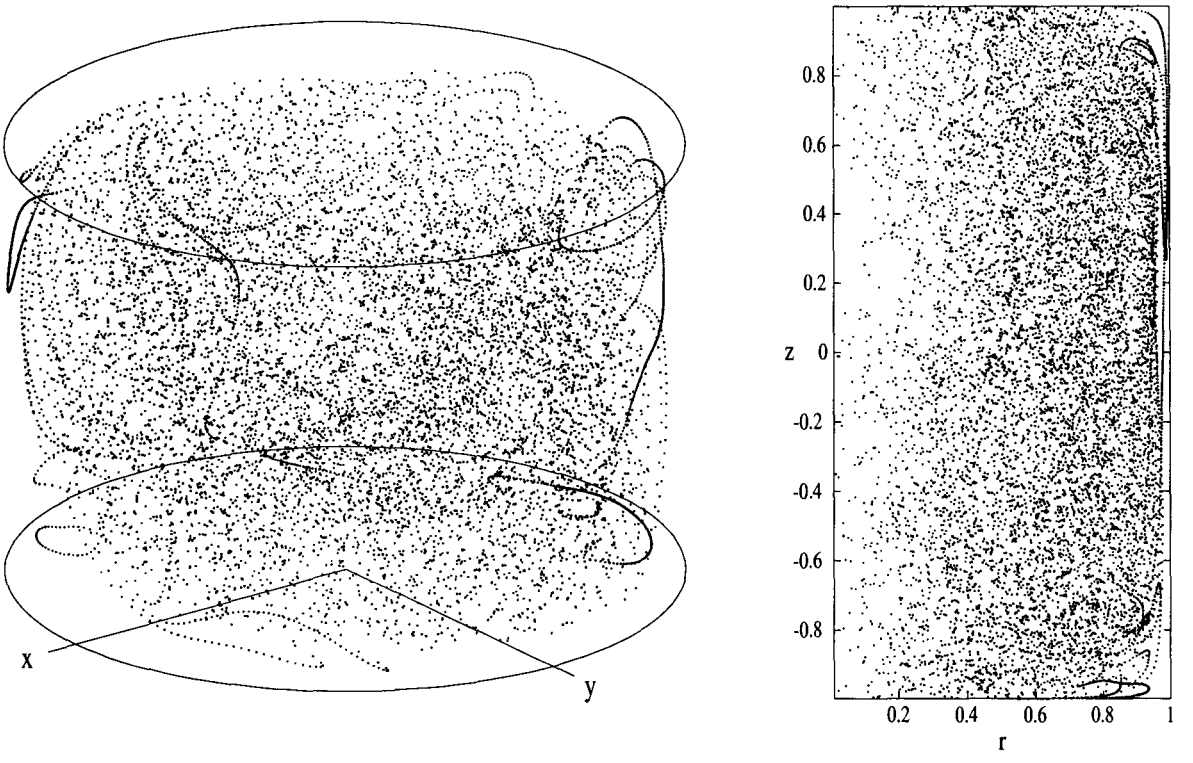

Figure 4.7: A tracer particle followed 10,000 global periods T. On the left side the Poincaré section for $Re = 10$ is represented. On the right side the rz-projection is shown.

where particle trajectories in the case $Re = 0$ form closed loops, while when $Re > 0$ these loops are broken and become non-closed outward spiraling loops.

It is expected that for $Re > 0$ tracers getting closer to the cylinder mantle. To show this, tracers have been released at (0.1231,0.3912,-0.6510) and are followed under the forcing conditions of protocol D over 10,000 global time periods T, for $Re = 10$ and 100. The Poincaré maps belonging to these simulations are plotted in the figures 4.7 and 4.8, respectively.

The rz-projection for $Re = 10$ still shows a small layer between tracer particle positions and the cylinder mantle, while for $Re = 100$ this layer is almost vanished, except in the lower and upper corner. It can be concluded that the inertial term of the Navier-Stokes equation helps the tracer to go everywhere in the cylindrical domain. It can be expected that the mixing under forcing conditions of protocol D is more efficient when $Re > 0$. To strengthen this assumption, the advection of a released blob is followed to see how the blob deforms and how the surface of the blob increases. In an experiment this can be carried out by the injection of a dye, see for example chapter 7 in Speetjens (2001).

A numerical spherical blob with radius $r/R = 0.1$ has been released at (0.3463, 0.3463, 0), this is elliptic point P_1 when $Re = 0$. The under forcing conditions of protocol D advected blobs are shown for $Re = 10$, 50 and 100, respectively, in figure 4.9 at $t = 2T$. At higher Reynolds numbers blobs are definitely more advected. The relative area of the different blobs are shown as a function of time in figure 4.10. The relative area function for $Re = 0$ is added, which is also numerically evaluated to make a direct comparison still possible. Differences between $Re = 0$ and $Re = 10$ are seen after 2 global forcing time periods, when $t = 2T$ both blobs are almost the same and therefore the advected blob for $Re = 0$ is not shown. Differences in relative area start growing after T, where $t = T$ corresponds to 20 in figure 4.10. Using higher Reynolds numbers enhances the mixing properties under the forcing conditions of protocol D.

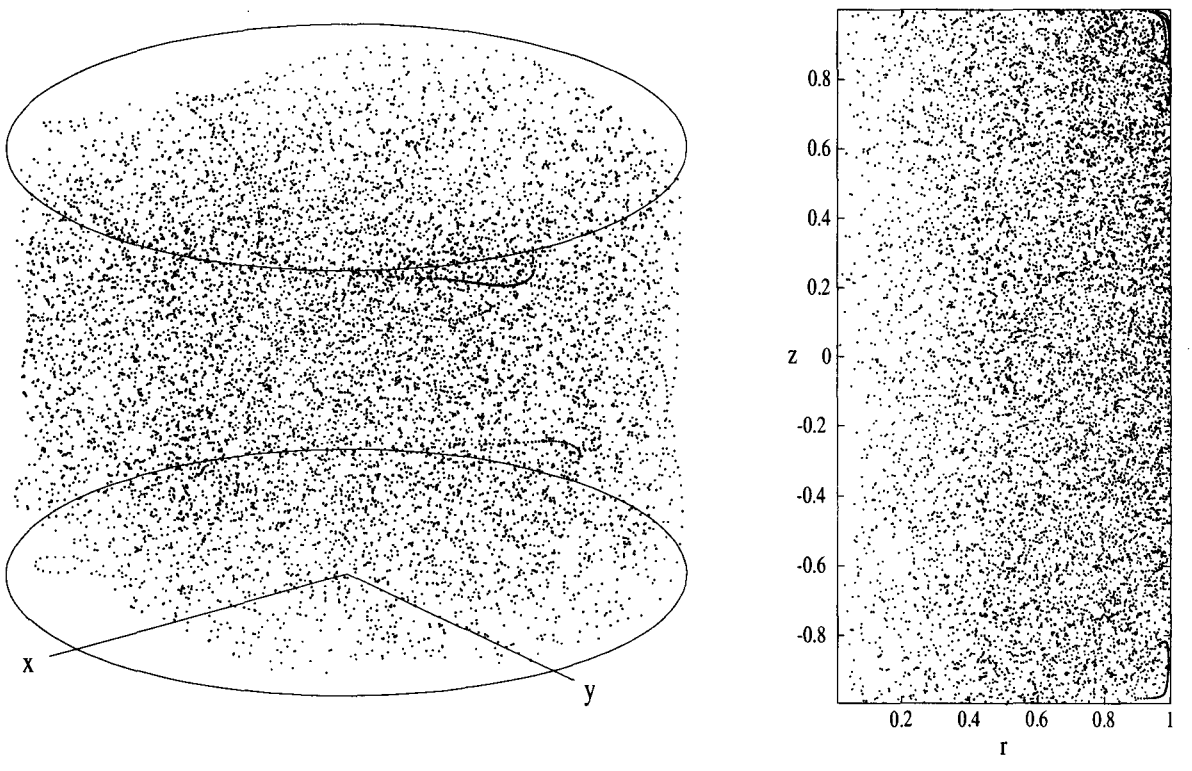

Figure 4.8: A tracer particle followed 10,000 global periods T. On the left side the Poincaré section for $Re = 100$ is represented. On the right side the rz-projection is shown.

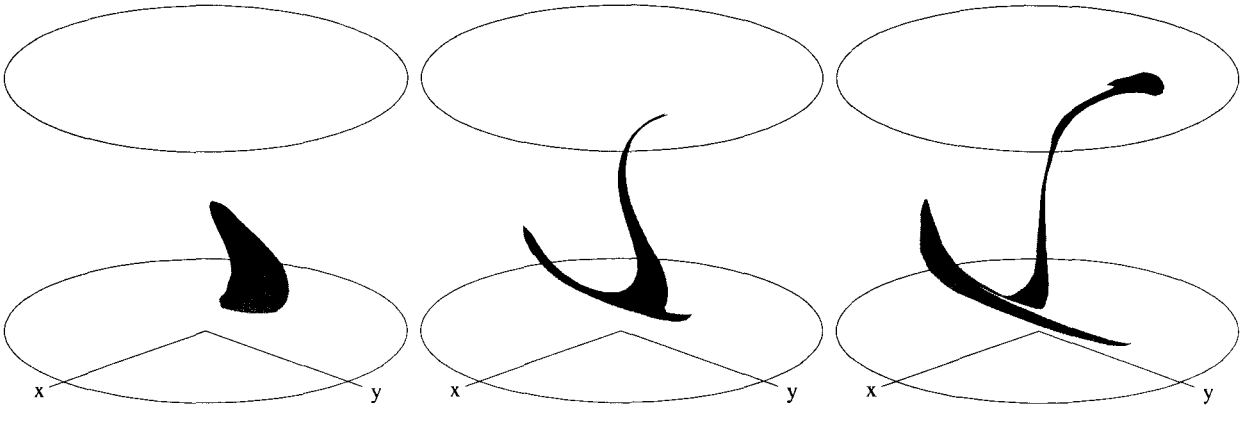

Figure 4.9: The advection of a blob released at P_1 shown after 2 global forcing times T of protocol D. The advected blobs are shown for the cases $Re = 10$, 50 and 100, respectively.

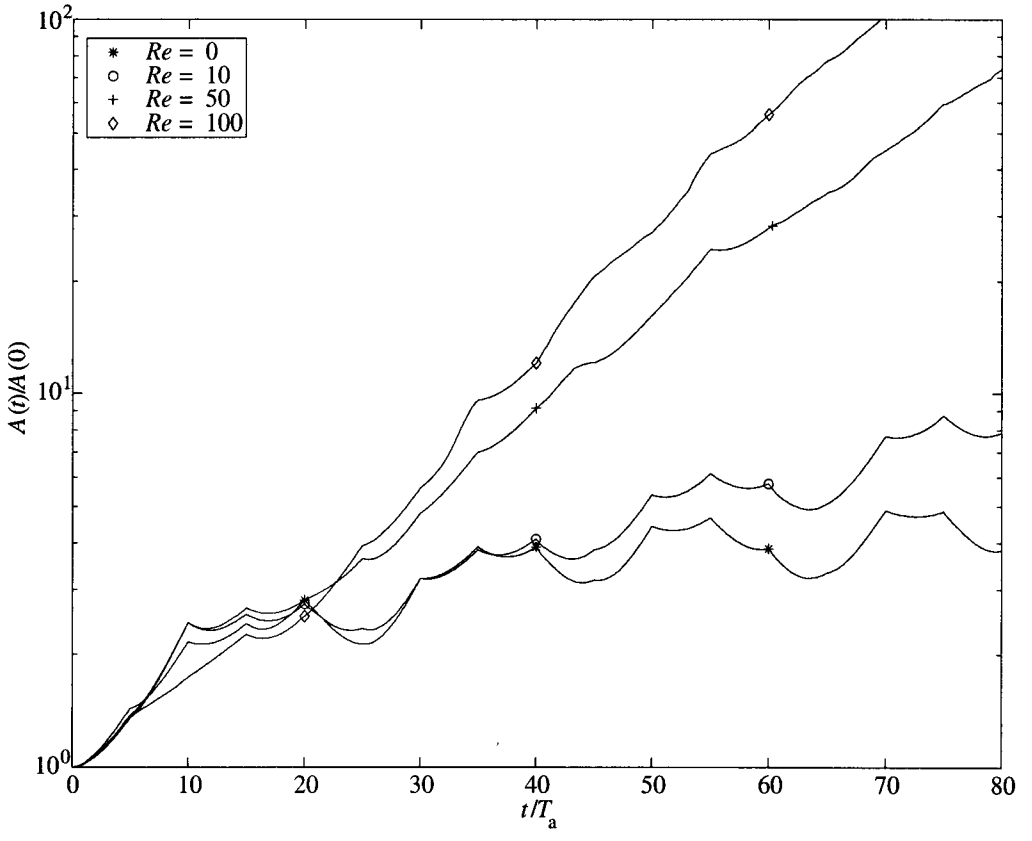

Figure 4.10: Relative area growth of a spherical particle released at P_1 and forced by protocol D. The different lines indicate the different Reynolds numbers.

Chapter 5

3*D* PTV

5.1 Theory of 3*D* PTV

In order to investigate flow phenomena it is possible to use tracer particles for the visualization of the flow. If the particles are small enough, they will act as *passive* tracers and will follow the fluid flow very closely. In a laboratory experiment the fluid is seeded with tracer particles, which are illuminated by source of light. This source of light may be laser, sky-spot or a simple slide projector.

Two dimensional Particle Tracking Velocimetry (2*D* PTV) can be seen as the precursor of three dimensional Particle Tracking Velocimetry (3*D* PTV). 2*D* PTV follows particles in a two dimensional flow field and measures their velocities. Installing one camera and a doing a single calibration in the plane of the measuring is enough before doing an experiment. The calculation of particle positions and their velocities is done by a 2*D* PTV algorithm, which is written by Bastiaans and Van der Plas. A lot of information about 2*D* PTV can be found in the user's guide PIV, PTV and HPV of Zoeteweij & van der Plas (2001). 3*D* PTV can be seen as an extension of the 2*D* variant, therefore a lot of the 2*D* tools, maybe slightly adapted, will also work for 3*D* PTV.

Typical for 3*D* PTV is that two or more cameras are being used and doing a calibration is more complicated. The best way to learn how 3*D* PTV works is to learn how the algorithm works, therefore the 3*D* PTV algorithm will be explained in the subsection 5.1.1. This will be followed by the experimental set-up in the section 5.2. The 3*D* algorithm needs a configuration file. An example configuration file is given and explained in appendix A. Where possible, parameters described in subsection 5.1.1 are written italic to give the direct relationship with parameters described in appendix A.

5.1.1 The 3*D* PTV algorithm

In figure 5.1 an overview of the 3*D* PTV algorithm is given. The algorithm starts with processing of the images. First dynamic thresholding is applied to remove background intensity variations. After that a 'blob' detection algorithm is applied to measure the positions of the particles on the images in pixel coordinates. The core of this algorithm is a 2*D* Gaussian fit through the intensity curve of a particle image. In this way a significant sub-pixel accuracy can be achieved. In the following two steps the actual 3*D* positions of the particles are retrieved. When the 3*D* positions of the particles are known, they can be correlated with the particles found in previous time step(s). When some information about the fluid flow is available, this can be used as a prediction to help the matching with correlated particles in the previous steps. The resulting path information is written into a file, which can be post processed to obtain velocity information or particle trajectory information.

Dynamic thresholding The dynamical thresholding is done by a square min-max subtraction filter. A square window size (*xsize*, *ysize*) has to be chosen to do the filtering procedure. This

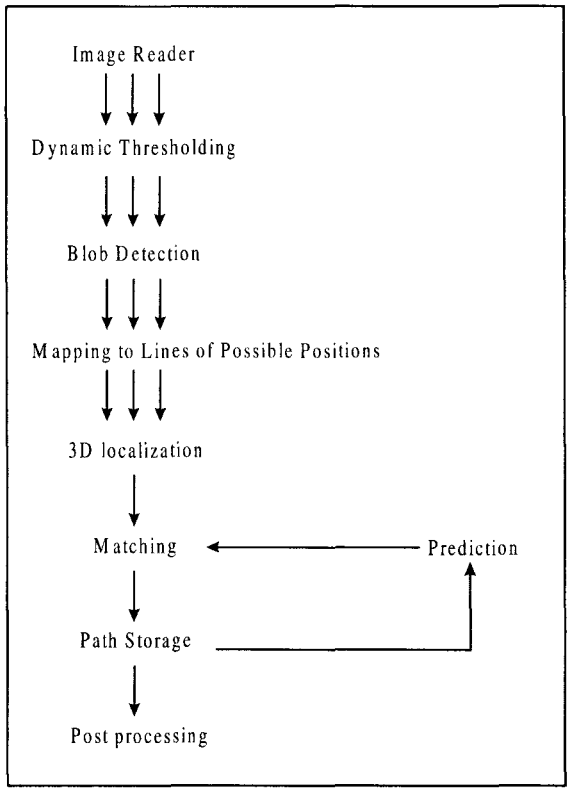

Figure 5.1: The scheme of the $3D$ PTV algorithm.

window size has to be chosen some greater than the blob size in pixel coordinates of the particles to be detected. The algorithm searches for the maximum and the minimum of intensity within the square windows. After that the maximum possible value will be subtracted from the original image, which will result in a dynamic thresholded image. Non-uniform background noise due to reflections and some optical effects like distortion are almost disappeared in this way. Another advantage of this method is, that particle positions are not influenced as they will, when using high-pass filtering procedures. In this way the blobs remain approximately Gaussian.

Blob Detection

Pixels having a vertical or horizontal neighbour are called connected to each other. Regions of connected pixels in an image with an intensity higher than a specified threshold are called blobs. A single *threshold* has to be set just above the noise level of the dynamical thresholded images. Normally this threshold is very low, because most of the background noise has already been disappeared during the dynamic thresholding procedure.

The blob detection scheme selects the particles, which are greater than the minimum allowed size (*int min*) and smaller than the maximum allowed size (*int max*). The positions of these validated particles are determined with sub-pixel accuracy, by using a gray value weighted centre of gravity. A disadvantage of this method is, that only a sequence of maximal 10 frames can be followed at the moment.

An alternative method is peak detection. This algorithm is somewhat faster; it searches for peaks in the connected regions with neighbouring pixels. If a peak has been found, it is called a blob immediately. A disadvantage of this algorithm is that it does not select on blob sizes. However, when one is searching for long Lagrangian particle trajectories, peak detection is the only available option now.

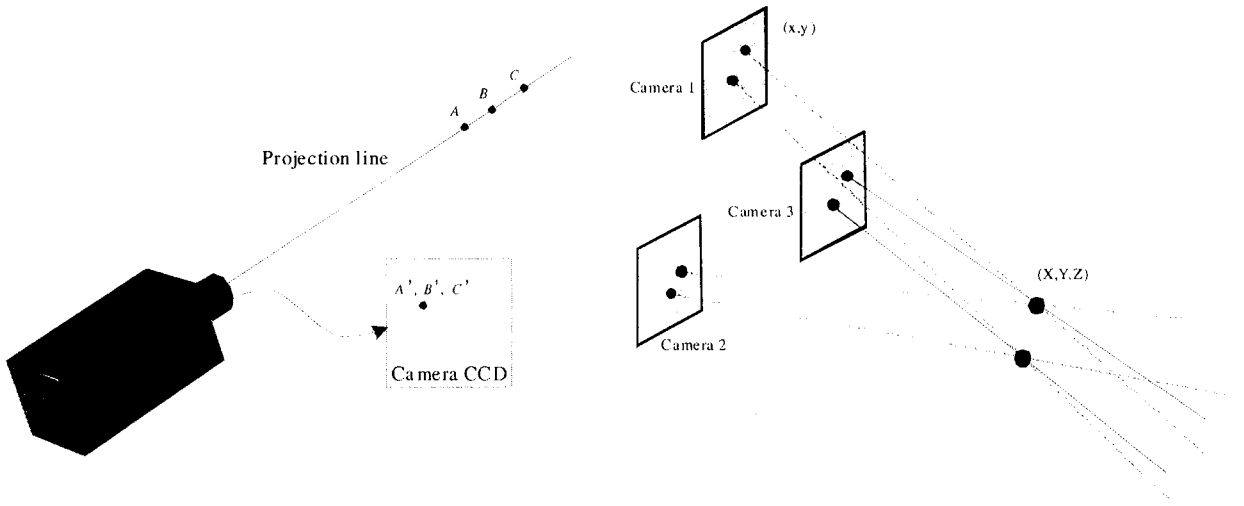

Figure 5.2: On the left side a perspective ray through A, B and C ends in a single projection point on the CCD of the camera. On the right side the $3D$ localization mechanism is shown. Three Projection lines are crossing in a single point in world coordinates, corresponding to a specific pixel coordinate combination on the three cameras.

Mapping to Lines of Possible Positions and $3D$ localization

The main idea of the $3D$ particle localization procedure is that a particle image position, in pixel coordinates, correspond to a position in world coordinates somewhere along a perspective ray, see the left panel of figure 5.2. Within the object volume no variation of the refractive index is allowed, because all perspective rays are assumed to be linear in that region. Normally, when looking to a single component fluid flow, this will not cause any problem. Outside the object volume moderate differences in the refractive index are allowed, even the enclosing body, which is often made of perspex, may have another refractive index. Filming sharp boundary edges is not allowed, because that troubles the assumed continuity within the to be filmed object volume. By using two or more cameras filming under a different angle, the three dimensional image can be reconstructed. How the localization procedure for the reconstruction of the three dimensional image works, can be seen on the right panel of figure 5.2. The points in space where rays from the different cameras cross, are the positions of the particles. In reality lines do not cross exactly, therefore a maximum matching distance (*F3DLocator: maxiummatchingrange*) is needed.

In principal two cameras with non-coinciding vantage points would be enough. With the used calibration technique, orthogonal angles between the cameras are not possible, so lower angles should be used, therefore minimal three cameras should be used. When using a high particle seeding density, it is possible that some particles will hide. According to a publication about $3D$ PTV and Lagrangian motion Virant (1997) at least four cameras are preferable to gather qualitative good experimental Lagrangian information. The transformation of the detected particles, in pixel coordinates on the different cameras, to world coordinates will be done by means of a calibration in-situ. A well defined grid in world coordinates enables the transformation from pixel coordinates of each camera to world coordinates and vice versa. The transformation is given by: $J_i : (x_p^{(i)}, y_p^{(i)}) \Leftrightarrow (x_w, y_w, z_w)$, with $i = 1, 2, 3$ indicating the camera number. More details about the specific used calibration can be found in the section 4.2.

Matching

The best pairings of particles between two images can be found by using the following basic evaluation function

$$c_{ij}^{f} = \left| x_i^{f+1} - x_j^{'f} \right|, \tag{5.1}$$

where $x_j^{'f}$ is the estimated position of particle j from frame f in frame $f+1$. If there is a good estimation or the displacement of the particle is very small, then low values of c_{ij}^{f} correspond to a high probability that the two particle images originate from the same physical particle. There are two types of matching, namely temporal matching and a spatial matching. The solver should find a set of independent matchings. If there is a matching between particle image i in frame f and particle j in frame $f+1$ then $\alpha_{ij}^{f} = 1$ otherwise $\alpha_{ij}^{f} = 0$. By using this definition, the set of matchings is independent if and only if

$$\forall_i \sum_j \alpha_{ij}^{f} \leq 1 \qquad \& \qquad \forall_j \sum_i \alpha_{ij}^{f} \leq 1. \tag{5.2}$$

This means that a particle in frame f can only be assigned to at most one particle in frame $f+1$ and vice versa. Furthermore, the set should contain as many matches as possible. The maximum number of matchings possible is determined by the minimum number of observed particles of the two frames involved.

To optimize the number of matches, the sum of $\alpha_{ij}^{f} c_{ij}^{f}$ over all values of i and j should be kept as low as possible. This optimization problem can be solved by an extended Munkres algorithm. A (*matcher: maximum matching distance)* $\Delta s_{\max}$, is introduced to optimize for speed in this algorithm and to prevent for ridiculous matchings. A good measure for this maximum matching distance is the displacement of the moving endwall between two frames, which of course is equal to the maximum possible displacement. A reliable matching occurs in general when:

$$\Delta s_{\max} < \widehat{d}_n, \tag{5.3}$$

with $\widehat{d}_n$ the mean minimum inter-particle distance. $\widehat{d}_n$ is described by

$$\widehat{d}_n = C \sqrt[3]{\frac{V}{N}}, \tag{5.4}$$

with N the number of particles in the closed volume V and C some constant. For simple regular structures this constant C is equal to or slightly greater than one. A numerical analysis for irregular structures would lead to a value somewhat smaller than one, but for plainness this constant C will be held equal to one.

Prediction

To help the matching procedure a prediction scheme can be used. A temporal extrapolation can be used when former particle positions are known. When the last N_t (*Fpredictor order)* particle positions are known, the future position can be estimated by a polynomial of order $N_t - 1$. Linear extrapolation $N_t = 2$, normally gives the best results. This is when particles between two successive processed frames are moving further than by Brownian motion alone and when the particle density is sufficient high to measure an accurate velocity field. $N_t = 1$ leads to no temporal prediction at all.

When no temporal extrapolation can be used, because no former positions are available or when the extrapolation mode is turned off ($N_t = 1$), spatial interpolation will be used. Spatial interpolation is performed by using the positions of neighbouring particles or by using an external

source with velocity information. In the case of $2D$ PTV, PIV results will often be used as an external source. In the future it is maybe possible to use Shankar's analytical solution for $Re = 0$ as a source of external velocity information. When using the neighbouring matched particles, indicated by the subscript k, the estimated position is calculated by

$$x_i^{f+1} = x_i^f + \frac{\sum_k \beta_k \left|\left| x_k^{f+1} - x_k^f \right|\right|}{\sum_k \beta_k}, \tag{5.5}$$

with β_k the neighbouring weighting function, which is chosen to be Gaussian with characteristic width σ (*Gaussian Delta*). The last parameter in the configuration file is *minimum particles*, this can be can as a kind of threshold, making Gaussian estimation only work when there are sufficient weighted neighbouring particles present.

Post processing

The post processing routine *f3dpostES1.0new* contains several options to store found particle trajectories or to calculate particle velocities. Some of these options are treated here.

The option f stores all particles beginning at a certain frame with a maximum defined pathlength. New is the option n, which stores the newly found particle paths with a maximum defined pathlength. With a newly found particle is meant a particle starting in frame i, that has not been matched with a particle in frame $i-1$. A clever combination of the options f and n make it possible to find all particle trajectories over a certain time span of interest. How to do this is explained in Appendix B.

For the calculation of the particle velocities a couple of methods are available. A central second order scheme will usually work the best. Option v can be used for doing this, with s the central frame number and $p = 1$ to apply the central second order scheme. Higher values of p lead to a higher order schemes. By applying this method only particle velocities of particles with a minimum path length of $2p + 1$ can be calculated. The velocity calculated with the second order scheme of particle i in frame f with Δt time between two frames is given by

$$u_i^f = \frac{x_i^{f+1} - x_i^{f-1}}{2\Delta t}. \tag{5.6}$$

5.2 Experimental Set-up

The basic experimental set-up comprises of a container in which the cylinder mantle is submerged in a bath of silicon oil (type AK2000 by Wacker-Chemie GMBH, Munich, Germany). The endwalls are mounted on support structures, lowering them into the fluid in order to meet the cylinder mantle and can perform an in-plane motion via translation along two perpendicular guiding rails driven by electrical motors. The translational displacement $D = D_2 R \leq D_{\max}$ and the velocity $U \leq U_{\max}$ are both set and monitored by means of a computerized motion control system, permitting optimal reproducibility of the forcing conditions[1]. The container, the cylinder and both endwalls are fabricated of transparent perspex to reach maximum optical accessibility. The silicon oil has the same refractive index as the used perspex for cylinder mantle and the endwalls. The silicon oil has a very high kinematic viscosity ($\approx 2000\nu_{water}$) and a density somewhat lower than the density of water.

Relevant parameters are listed in table 4.1 and a projective view of the configuration is given in figure 5.3. The figure shows a gap between the cylinder mantle, this gap is smaller than 1.0 mm and therefore assumed to be irrelevant to the problem, but one should keep into mind that the cylinder is not a fully closed object, a small mass flux between cylinder and the rest of the tank is still possible. More details about this gap can be found in Speetjens (2001).

[1] Software written by Van Uittert has been used to control the motion system.

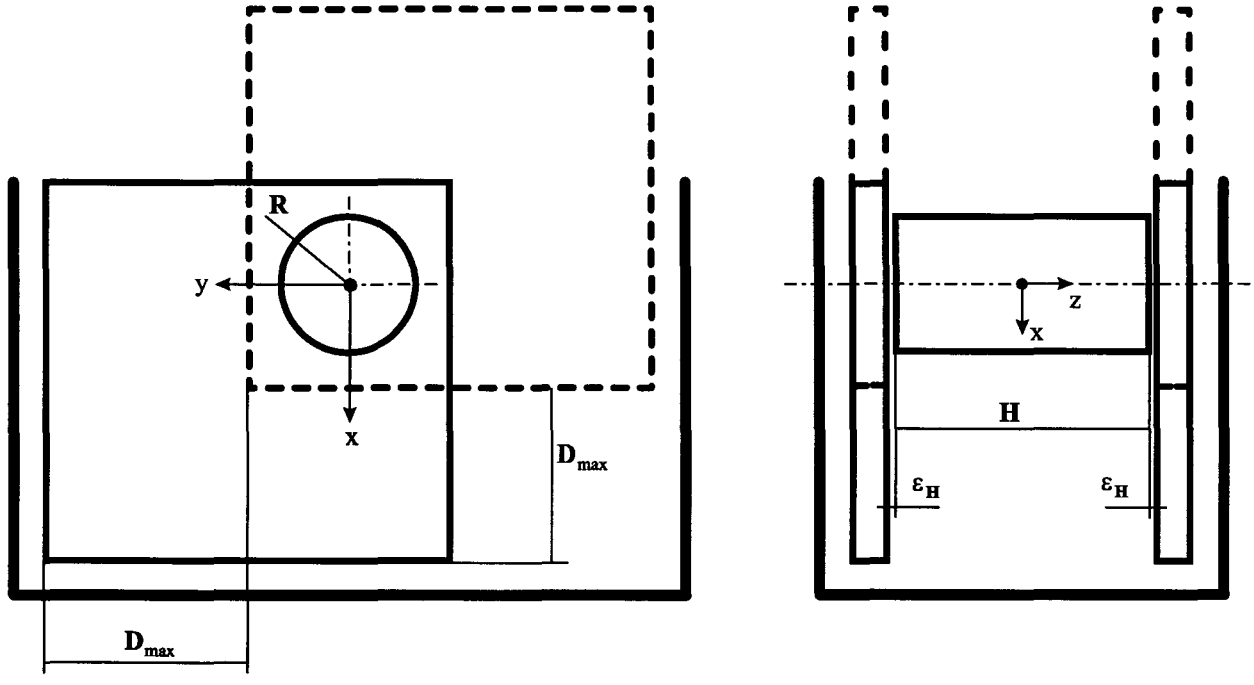

Figure 5.3: Schematic view of the experimental apparatus. The solid and dashed square in the left panel reflect the maximum horizontal/vertical displacement ($D_{\max}$) of either endwall and the variable ϵ_H indicates the axial-wise gap between the cylinder mantle and the translating endwalls. The actual measures are listed in table 3.1.

H [m]	R [m]	ν [m^2/s]	ρ [kg/m^3]	$D_{\max}$[m]	$U_{\max}$[m/s]
$7.0 \cdot 10^{-2}$	$3.5 \cdot 10^{-2}$	$2.0 \cdot 10^{-3}$	970	0.21	$2.3 \cdot 10^{-2}$

Table 3.1: Specifications of the experimental set-up.

Substitution of the values listed in table 3.1 into the dimensionless parameters defined in section 2.3 leads to

$$D_1 = 2, \qquad Re \leq 1.61, \qquad D_2 \leq 6. \tag{5.7}$$

In all experiments the Reynolds number will be set at $Re = 0.25$ and the dimensionless displacement at $D_2 = 5$. The Reynolds number is the same as Speetjens (2001) used in his experiments and thus allow for a direct comparison. The adopted values enables for an estimation of Sr_f and for a verification of the demand of $Sr_f \ll 1$ underlying adoption of (2.15) as governing flow model. Employment of relation (2.16) puts forth $Sr_f = 0.05$ and in consequence proves the steady state approximation (2.15) holds for the experiments.

In practice $Re = 0.25$ comes very close to $Re = 0$, considering the velocity field discrepancies which are found to be of order 10^{-3}, see Speetjens (2001). As a consequence differences between both Reynolds numbers might not be observed experimentally under laboratory conditions. Therefore experimentally results are directly compared to the analytical solution of Shankar ($Re = 0$), see Shankar (1997).

PTV set-up

Three high-resolution cameras (1018×1008 pixels 10-bit gray scale Kodak ES 1.0 camera by Roper Scientific, San Diego, USA), are positioned in a triangular form as shown in figure 5.4, viewing the bottom wall of the cylinder under an angle $\alpha \approx 8^0$ relative to the z-axis of the cylinder. The

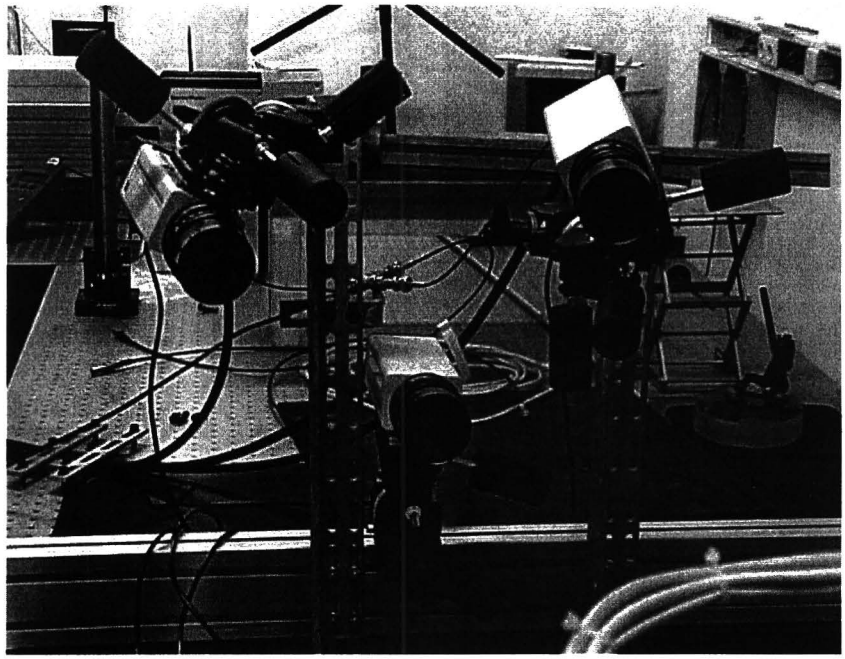

Figure 5.4: Camera arrangement. Cameras are attached to iron standards. Left under, the cable attachment to the table can be seen.

adapted camera arrangement ensues from a compromise between optical performance of the tracking algorithm (recommended angle $\alpha \approx 20^0$, see Schreel et al. (2000)) and maximum visibility of the interior of the cylinder ($\alpha \rightarrow 0$). Note that this 20^0 correspond to a triangular pyramid with equal legs with all angles 60^0. The camera cables are attached to the table to overcome movements of the camera by forces on the cable. The distance between the camera triangle and cylinder bottom endwall is 1.2 m in the z-direction. Lenses being used have a focal length of 75 mm.

Each camera is connected to one of the three measurement computers. The disk sizes are 68.4 GB and the maximal data flow is 60 MB/s continuously. The configuration of each of these computers is identical. The computers are connected to a network hub, to let the computers communicate with each other and to make a single network connection. The software needed for the detection of a connected camera is *Kodak Universal Remote*. In this program it is possible to adjust some settings. A camera can work in a continuous running mode (or free running mode) or in a triggered mode. A camera running in the continuous mode captures frames at 30 Hz. The three cameras in this mode are connected to the *strobe* (internal clocking) connectors of each of the cameras by small coax cables. For frequencies lower than 15 Hz the trigger mode can be used. In this mode an external signal regulates the frequency. The cameras in the trigger mode are connected to the *trigger* connectors of each camera and to the external source, all by the small coax cable's. The software package *Video Savant* has been used to capture, view and store the images. This software package contains a lot of tools, for details on this subject see Zoeteweij & van der Plas (2001).

An important issue is the calibration, because a good calibration is needed to obtain accurate data from the measurements. The used calibration configuration is shown in figure 5.5. The displayed $2D$ calibration grid consists of a disk inserted into the cylinder, placed parallel in the xy-plane and accommodating an equidistant grid defined by small holes (diameter $d_h = 0.1$ mm) with spacing $\Delta x = \Delta y = 6$ mm. The L-shape in the centre of the grid (defined by three holes with diameter $d_h = 0.5$ mm), defines the locally xy-frame, with the short leg and the long leg indicating the x and y-axis, respectively. The calibration grid is translated from the bottom to the top with step size $\Delta Z = 3$ mm (*F3DLineMapper dZ)*, defining 24 parallel planes (*nZCalibr)*, collectively making up the $3D$ reference grid in the cylinder with height $H = 70$ mm. For the first

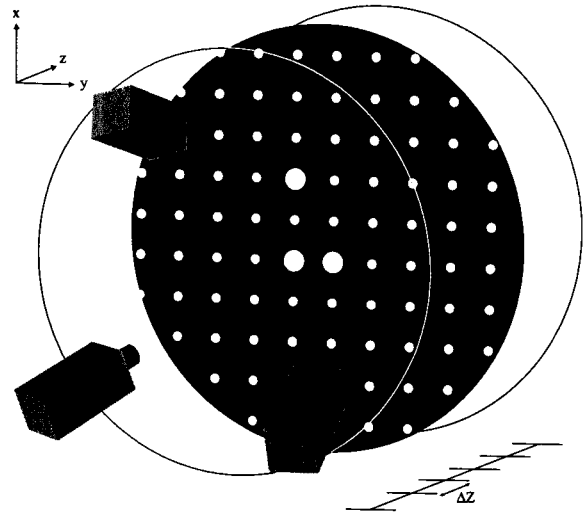

Figure 5.5: The calibration configuration consists of a 2D grid translated with step size ΔZ through the cylinder.

axial position it is recommended to stay little away from the bottom (≈ 0.5 mm), because otherwise the $2D$ calibration grid and bottom wall will stick together.

The optical settings should be optimized for measuring the particles. The calibration optics can be improved by adjusting the shutter time, no changes of other set-up parameters are allowed. When the measurement has been carried out, the data can be transported to a processing computer. When data is transferred, the most time-consuming part is the production of calibration images in such a way that only the calibration grid pixels are visible. This can be done with the aid of the image manipulation program *Gimp*. When all calibration images are perfect, calibration files can be made by using *Fac*. *Fac* is a program that relates the known $2D$ grid points in world coordinates to the grid points in pixel coordinates of the camera image. Thereafter a configuration file has to be made. An example is given and explained in appendix A. The processing and post processing has already been described in the subsection 5.1.1 and can be used from this point.

5.3 Optics

The optics used in the experiment determines the quality of the recorded images q_i. Important optical effects are *distortion* (deformation of the image), *vignetting* (non-uniform image) and *depth of field* (camera can focus on just one plane). Optical distortion can almost be fully corrected for by using the mapping functions, and thus forms not a problem. Vignetting is the difference in light intensity for points with different distances to the optical axis. Using a smaller aperture decreases the effect of vignetting, however it also lowers the total amount of light intensity on the image, see Zoeteweij & van der Plas (2001). Both effects exists in two and in three dimensions. Depth of field is different, because it plays only a role in a three dimensional object space. Therefore some extra attention will be paid to it.

Depth of field is important if one wants to obtain images with a high image quality q_i. With some rather simple geometrical optics, a good approximation of this depth of field can be made. To obtain this approximation the derivation will follow here.

The enlargement factor N in the set-up can be seen as a constant, because samples of the whole cylindrical surface with dimensions πR^2 ($L = 2R$) are wanted to be fully projected on the CCD's

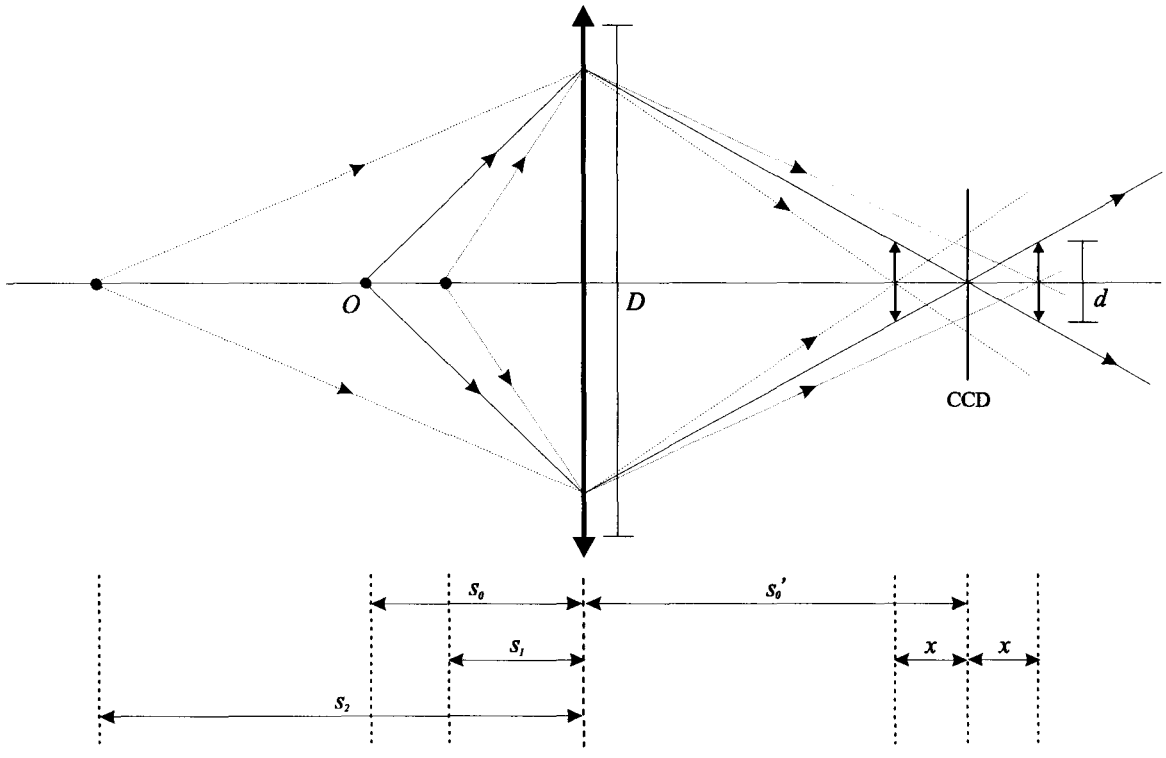

Figure 5.6: Construction illustration of depth of field. Object and image spaces are not on the same scale represented in this figure.

of the cameras with dimensions of 10×10 mm ($L' = 10$ mm). This enlargement factor is given by:

$$N = \frac{s_0'}{s_0} = \frac{L'}{L}, \tag{5.8}$$

with s_0 the object distance and s_0' the imaged distance. Resulting in an enlargement factor $N = 1/7$, when a cylinder with radius $R = 3.5$ cm is used. When a lens with a focal distance f is chosen, the optimal object distance can be calculated by using the enlargement factor and the thin-lens equation by elimination of the imaged distance s_0'. The thin-lens equation is given by:

$$\frac{1}{f} = \frac{1}{s_0} + \frac{1}{s_0'}. \tag{5.9}$$

The explicit expression for s_0 is given by:

$$s_0 = \left(\frac{N+1}{N}\right) f. \tag{5.10}$$

The depth of field can be introduced by accepting circles of confusion with an acceptable diameter d, such that all images are well focused within a distance x. This approximation has been made in *Introduction to Optics* Pedrotti & Pedrotti (1993). The construction for the calculation of depth of field is shown in figure 5.6. Note that the interval about s_0' in the image space is symmetric, while the depth of field is not symmetric about s_0. The near-point and far-point distances s_1 and s_2, can be determined, when a allowed blurring parameter d is chosen and the lens is specified by focal length f and the circular aperture diameter D. On a camera the aperture will normally be given relative to the focal length in the following way:

$$A = \frac{f}{D}, \tag{5.11}$$

with A the *relative aperture*. By using some algebra the near-point s_1 and the far-point s_2 distances can be expressed in the following way:

$$s_1 = \frac{s_0 f(f + Ad)}{f^2 + Ads_0}, \qquad s_2 = \frac{s_0 f(f - Ad)}{f^2 - Ads_0}. \tag{5.12}$$

The depth of field, $\Delta s = s_2 - s_1$, can be expressed as

$$\Delta s = \frac{2Ads_0(s_0 - f)f^2}{f^4 - A^2 d^2 s_0^2} \overset{\text{sub. eq. (5.11)}}{\Longrightarrow} \Delta s = \frac{2ds_0(s_0 - f)fD}{f^2 D^2 - d^2 s_0^2}. \tag{5.13}$$

The blurring parameter d has to be chosen very small, a good measure could be the typical size of a pixel the 1018×1008 CCD camera, which is about $1/1000$ of L'. Because d is very small, d^2 is so small that it can be neglected. Applying this to equation (5.13) leads to the following reduced equation

$$\Delta s = \frac{2ds_0(s_0 - f)}{fD}, \qquad \text{assumed that} \quad d^2 << \frac{f^2 D^2}{s_0^2}. \tag{5.14}$$

This reduced equation can be written in a more convenient form, by using equation (5.10) in the slightly different form

$$N = \frac{f}{s_0 - f}, \tag{5.15}$$

resulting in

$$\Delta s = \frac{2ds_0}{ND}, \qquad \text{with} \quad d^2 << \frac{f^2 D^2}{s_0^2}. \tag{5.16}$$

There are three manners to increase the depth of field, all having the same disadvantage that less light will fall on the CCD's of the cameras. Decreasing the enlargement factor N, by using a bigger cylinder or increasing the focal length f using relation $s_0 \sim f$, see equation (5.10) leads to a reduction of light falling on the CCD's of the cameras, because the object distance increases, while light intensity $I \propto \frac{1}{s_0^2}$. Another option is closing the aperture more, which also leads to a light reduction falling on the CCD's , while light intensity $I \propto \frac{1}{A^2}$.

A to be filmed volume will have certain dimensions. The depth of field should always be minimal the height of that volume. Applying this to equation (5.16) lead to an inequality equation. This inequality equation is derived for a very general case. As blurring tolerance the typical size of a pixel of an $n \times n$ CCD is used, leading to a blurring size $d = L'/n$. The minimum required depth of field is the height H of the to be recorded object (cylinder) and thus requires $\Delta s \geq H = D_1 R = D_1 L/2$. All together this results in the following inequality equation

$$D \leq \frac{4(N+1)}{nND_1} f \quad \text{or} \quad A \geq \frac{nND_1}{4(N+1)}. \tag{5.17}$$

The inequality equation shows, that using an object, with less depth relative to the front size, is preferable (small D_1). In this inequality equation it can also shows, that increasing the focal length f leads to a less restricted aperture, but relatively seen it is not effective.

In the experiments 1018×1008 CCD cameras ($n \approx 1000$) are used, lenses with focal length $f = 75$ mm and a cylinder with aspect ratio $D_1 = 2$. Resulting in a maximum feasible enlargement factor of $N = 1/7$ leading to the restriction $D \leq 1.2$ mm for the aperture. The enlargement factor used in the experiment is about 70% of the maximum possible value, relaxing the aperture to $D \leq 1.65$ mm (or $A \geq 45$), which is still very small.

Chapter 6

Accuracy assessment of the $3D$ PTV algorithm

Two sessions of experiments have been carried out. In the first session, steady flow measurements are done, with different particle densities. Before doing the second session some improvements have been implemented. In this second session a steady flow measurement has been repeated but with just one particle density. During this session a measurement of the complete forcing protocol D has been attempted. After these two sessions, two methods to check the results of a measurement are treated. In both sessions it appears that particle size is an important issue and therefore an experiment with some greater particles, has been carried out. In paragraph 6.5 two quality factors are introduced. These quality factors are adapted versions of the quality factors introduced for $2D$ PTV. In paragraph 6.6 the summary of this accuracy assessment chapter is given.

6.1 First Session

6.1.1 Steady flow

Particle trajectories and a velocity field can be found when the $3D$ PTV algorithm has been applied. For the steady flow case typical results are given in figure 6.1, with on the left panel all the particle trajectories of a complete steady flow experiment and on the right panel the velocity field calculated with the second order scheme at a certain moment. Both panels give a global impression of the steady flow. The bottom endwall has, during the steady flow translation, a velocity of $U = 3.57$ mm/s, which sets the dimensionless parameter to $Re = 0.25$. Remind that for $Re = 0$ all trajectories can be projected in the rz-plane, without crossing each other. The experimental Reynolds number is so close to zero, that for the small time scales being used, this projection is still allowed. The rz-projection of all the particle trajectories are shown on the right panel of figure 6.2. On the left panel the xy-projection can be seen. In the xy-projection particle trajectories cross, especially when away from the x-axis. The noise along the particle trajectories in the rz-projection is striking. This noise is mainly caused by vibrations of the cameras[1].

The PTV algorithm has initially been developed for the measurement of particle velocities only. Therefore good results are often defined in terms like high quality velocity fields with less mismatches. For studying chaotic advection, long Lagrangian particle trajectories are required, which makes knowledge of the velocity field alone not enough. Therefore another criterion will be introduced, valid for the rest of this report. Long particle trajectories without mismatches, will be used as criterion of being a good result. The output of the $3D$ PTV algorithm of course depends

[1] At the moment of measuring, people were building in the direct surroundings and causing a lot of vibrations. In the second session cameras are attached closer to their standards and rubber has been used to reduce the effects on experiments.

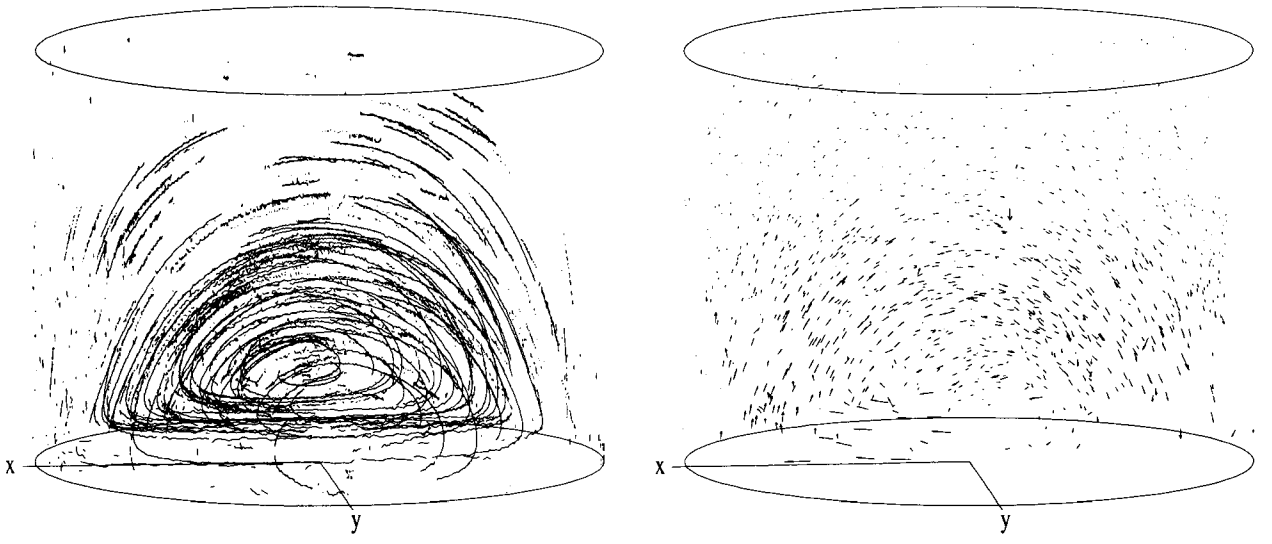

Figure 6.1: Post processed data from a steady flow measurement, directly plotted. On the left panel all particle trajectories of a complete steady flow experiment. On the right panel a velocity field calculated with the second order scheme at a certain moment.

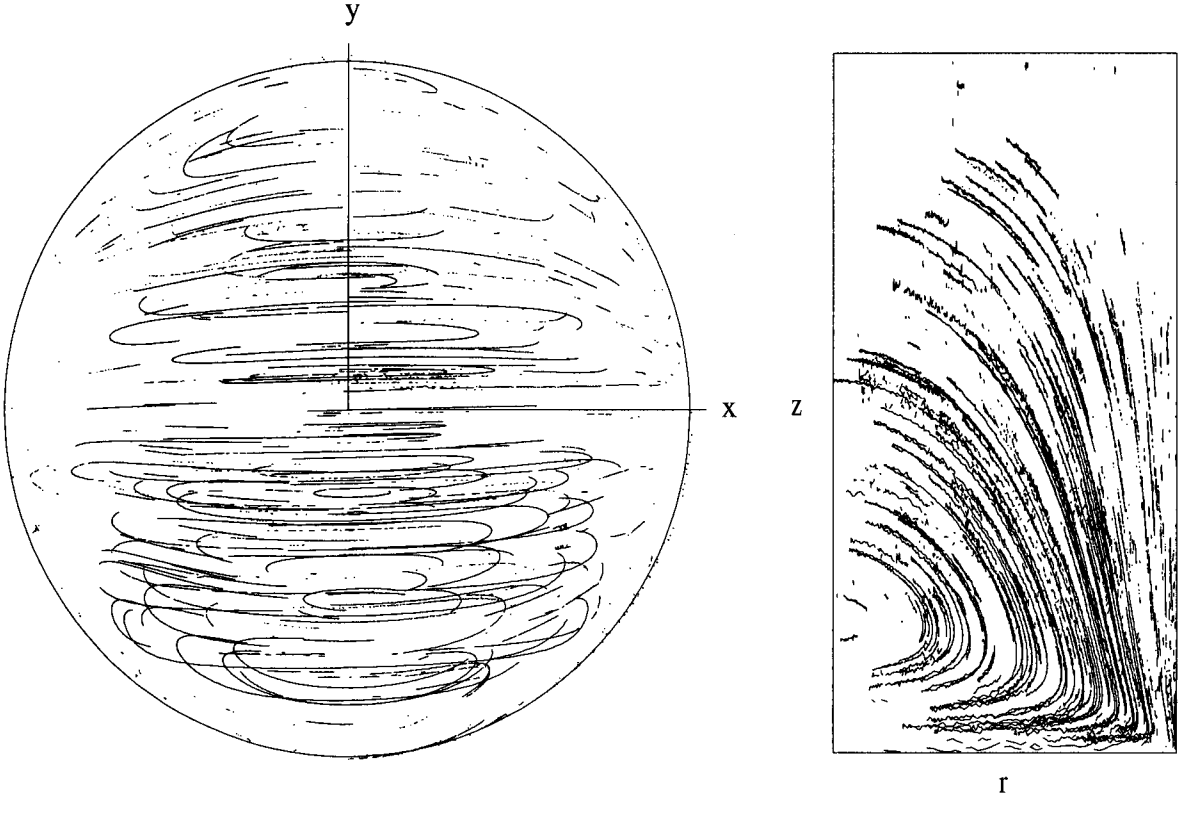

Figure 6.2: Projections of a complete $3D$ PTV steady flow measurement. On the left panel the xy-projection is shown. On the right panel the rz-projection is shown. The primary eddy structure can be seen in the rz-projection.

on the parameters being used, which are set in the configuration file. For an explanation of a configuration file, see appendix A.

The parameter to set the prediction scheme can be seen as an illustrative example to show how different these two criteria really are. According to the subsection 5.1.1, linear extrapolation often leads to the best results. This is true, when applying the velocity criterion, but for the long particle trajectories criterion this no longer holds. In that case no prediction leads to the best results. The reason therefore is, that linear extrapolation leads to mismatches or no matchings at all, when a particle highly deflects. For the velocity field criterion, this is no big deal, just losing one vector. In the next frame(s) the particle will be back again for a newly measured velocity field. For finding long trajectories this is a problem, only short trajectories can been found.

6.1.2 Particle Trajectories

An important $3D$ PTV set-up parameter is the particle seeding density. This parameter is varied by doing four steady flow measurements with an increased particle density. Before the measurements are carried out, the particles are mixed as good as possible through the whole domain, in order to create a homogeneous particle density. In the $3D$ PTV algorithm the trajectories are identified by identification and matching of the subsequent particle positions, proceeding through the recorded time sequence. To compare the results of the four experiments, the parameters in the configuration file are kept equal. The number of initially detected particles N_0 in the first frame will be used as a measure for the particle density. The path length will be defined by a time span by $t_p = (p-1)/f$, with p the number of followed frames and f the sample frequency. Samples are taken in the continuous running mode, so the cameras sampled at 30 Hz. The frame skip in the configuration file has been set to 5, which makes the actual sample frequency $f = 6$ Hz. This results in a sequence of $P = 348$ frames.

To say more about the long particle trajectory criterion, the yield parameter will be introduced. This yield is defined as:

$$Y_p = \frac{\sum_{k=p}^{P} n_k}{N_0}, \tag{6.1}$$

with n_k the number of particles all starting on $t = 0$ with path length t_k. The variable Y_p thus defines the fraction of initially detected particles N_0 with path length $t \geq t_p$. This is the same definition as being used by Speetjens, another definition would also be imaginable but this one is clear and simple. Results are represented in figure 6.3, where the different lines represent the different particle densities. The experiments are labeled with a, b, c, d, corresponding to the increasing initial detected particle numbers of $N_0 = 86$, 190, 684, 2968, respectively. All lines show a bend, indicating the moment upon which the bottom endwall starts to move and in fact indicating the starting point of the steady flow experiment. It is nice to show that a complete experiment in fact exists out of two smaller experiments, namely a non-forcing part (zero motion) and a steady flow part. In the case of a protocol with more than just one single step, this would possibly lead to more of these bends, each indicating a new starting point.

The yield parameter is expected to be an exponential decreasing function of p, because a constant fraction will be lost in every next processed step. In the steady flow case the yield can be approximated by two straight lines, one before the bend and one after the bend. It can be seen that the slope for zero motion is much less than for steady flow, which means that non-moving particles are more easy to follow. In experiment d only 118 frames could be followed, because the particle seeding density is too high for the $3D$ PTV algorithm.

Experiment b definitely gives the best yield results: 36 of the 190 initially detected particles could be followed during the whole experiment (348 frames). For experiment a and c only 16 and 24 particles, respectively, could be followed. Speetjens could only follow 11 particles of the 874 initially detected particles and just for 230 frames. Major improvement is caused by using no prediction

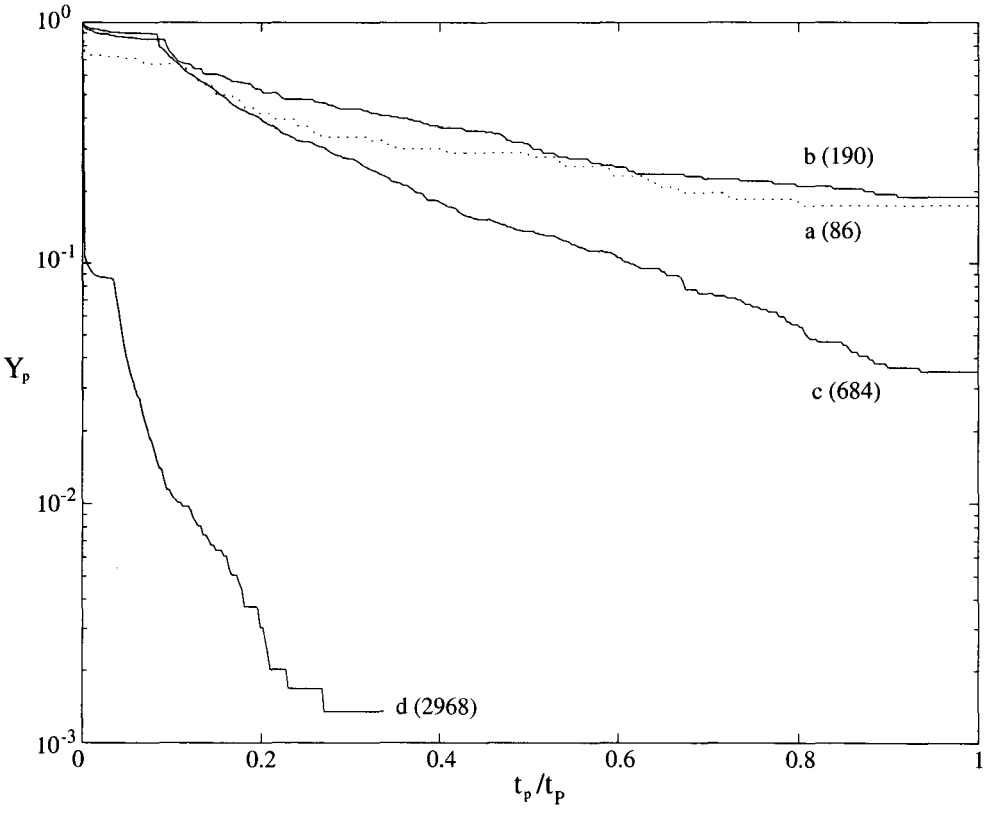

Figure 6.3: The yield function of steady flow experiments for different particle densities. The different experiments, are indicated with a letter. The number between the brackets indicates N_0. The used sample frequency is 6 Hz. All the lines show a bend after a couple of frames, from this point the bottom endwall starts with its steady translation.

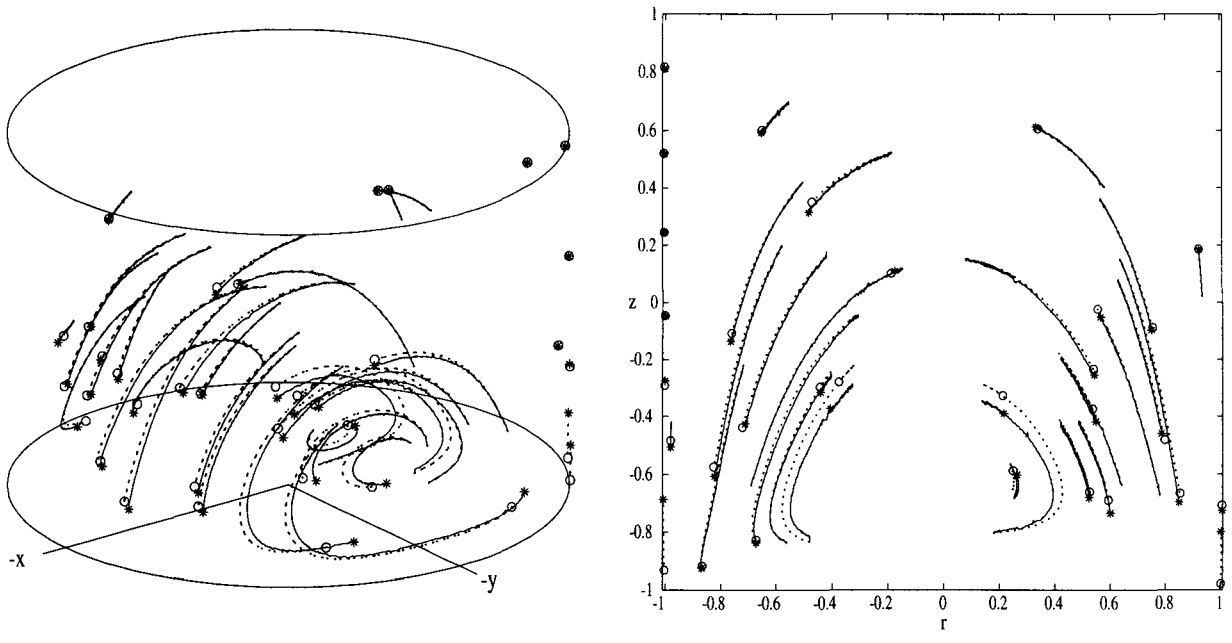

Figure 6.4: On the left panel all 36 complete measured particle trajectories are shown, with their numerically simulated particle trajectories (dashed). On the right panel the rz-projection of 31 complete particle trajectories is shown, to show the small difference between experiments and numerical simulations. Measured end points are indicated with $*$ markers and numerical calculated end points are indicated with o markers.

scheme and of course using a lower N_0 value is profitable, see figure 6.3. All further analysis will be done with the results of experiment b only. All complete particle trajectories of this experiment are given on the left panel of figure 6.4. The end of the measured trajectories are indicated with $*$ markers.

A comparison with numerical results has been made. The numerical trajectories start exactly at the measured begin positions of the particle trajectories. The end points of the numerical trajectories are indicated with o markers. To show more details the rz-projection of 31 of the 36 particle trajectories are given on the right panel of figure 6.4. Some of these particle trajectories are projected in $-r$ direction and 5 particle are leaved out for clarity. Most differences between measured and numerically obtained particle trajectories can be seen in the centre region of the primary eddy were particle trajectories are highly deflecting. The end points of particle trajectories have an average mismatch with their numerical found end points of $\Delta d = 2 \pm 2$ mm and a median of 1.2 mm. These values express the high quality of measured long particle trajectories. Note that long particle trajectories are normally more accurate than shorter ones, because for short particle trajectories mismatching is more probable than for long particle trajectories. For the simulation $Re = 0$ has been used, while in the experiments this is not the case and even more important is that there is an error between grid coordinates and world coordinates caused by the method of calibration. In the second measurement session a correction procedure will be introduced to eliminate the differences between grid coordinates and world coordinates.

Long particle trajectories can be found by using the yield parameter. To say more about the quality of the long particle trajectories, the mismatch has been given. Particle trajectory segments are accurate too. To show this, all particle trajectories of the whole experiment with $t_p > 0$ are shown in the rz-projection on the left side of figure 6.5, the right side has been used to show a couple of numerically simulated streamlines. In total 5844 particles are detected, of which 2730 particles have a pathlength $t_p > 0$. The measured particle trajectories in the rz-projection looks

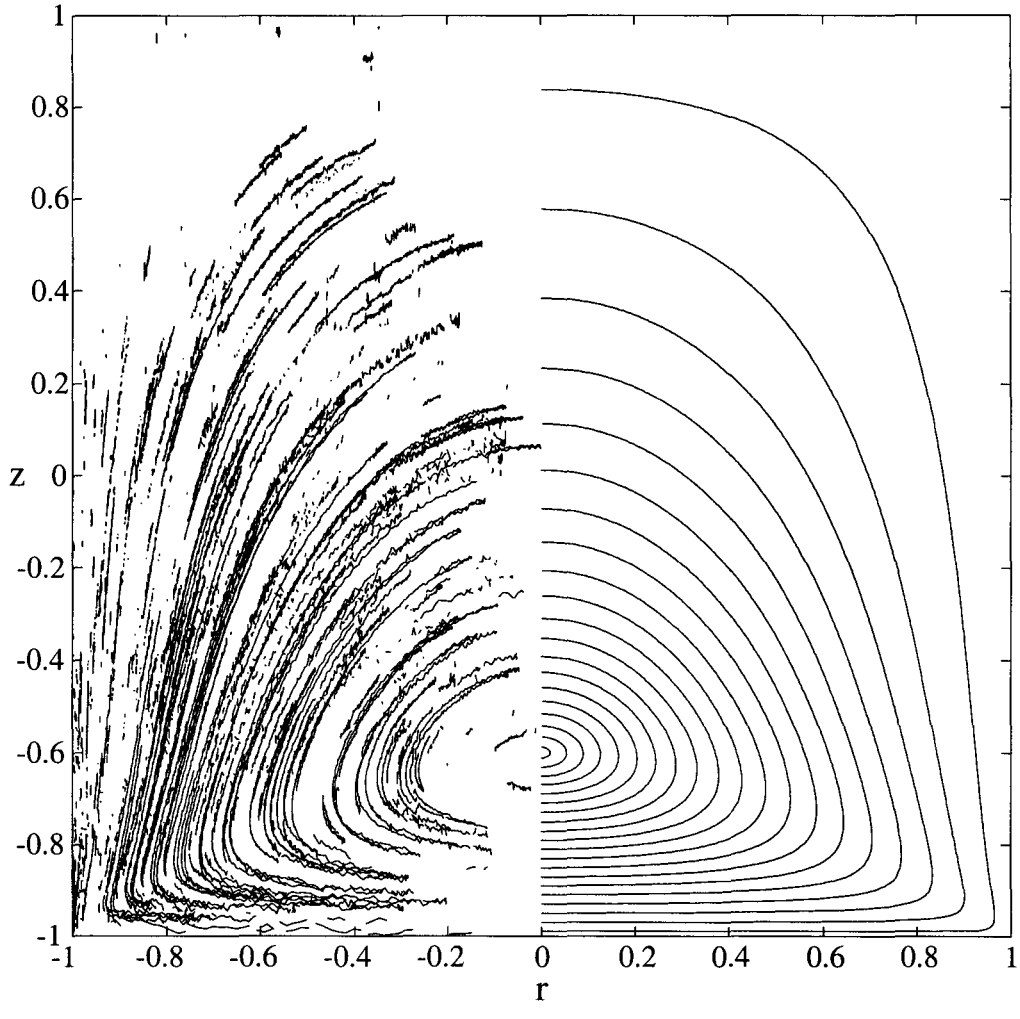

Figure 6.5: All rz-projected measured particle trajectories with $t_p > 0$ are plotted on the left side. On the right side a couple of the rz-projected numerical streamlines are shown.

very similar to the numerically simulated streamlines.

6.2 Second session

6.2.1 Steady flow

In the second session rubber has been used between the laser table and the standard to reduce the influence of vibrations on the cameras. The cameras are attached as close as possible to their standards. All calibration tools are coloured black, to prevent for reflections. On the outer side of the top endwall black perspex has been attached to reduce reflections. Important is that this black perspex also masks the uninteresting part of the measurement container. Some more attention has been paid to the depth of field and the full gray scale has been used. The cameras are set in the triggered mode at 12 Hz, because that has appeared to be fast enough to follow the particle movements in all details. Only at higher Reynolds numbers, it will be useful to increase the sample frequency of the cameras. When sampling at 12 Hz, protocol D can be measured for 10 complete forcing periods, before the harddisks on measurement computers are getting full.

A problem for this complete session forms the high particle density being used. The yield figure 6.3 already shows that large particle densities lead to a very low yield. To show that at least the applied improvements were effective, all long particle trajectories in the steady flow case are plotted in the rz-projection on the right side of figure 6.6 versus a number of long particle trajectories of experiment b on the left side. The dotted lines indicate the numerically simulated streamlines of the primary eddy. It can be seen that there are less wiggles on the measured particle trajectories in the second session. This shows that improvements to reduce the vibrations caused by external sources are very useful.

For the steady flow case only one particle could be followed during a complete experiment. This forecasts that no particle trajectories will be long enough to evaluate forcing protocol D. A measurement has been carried out under the forcing conditions of protocol D over two global forcing times T. Technically seen such a measurement is possible by now. However, due to the high particle density, only particle trajectory segments are found. Because protocol D consists of four steady flow steps and only short particle trajectory segments are found, no more than steady flow information can be derived. Therefore a measurement analysis of this protocol D will be left undone.

6.2.2 Endwall Movement

Knowing the exact positions of the endwalls is very important. In first place because grid coordinates are measured only relative in the currently used set-up, knowing the position of an endwall can resolve this problem. In the second place the fluid flow depends entirely on the boundary conditions and therefore better knowledge will lead to better results. All this information can be gathered from the endwall motion itself. Therefore white dots with a diameter of 1 mm are painted on the inner side of the endwalls acting as passive tracer particles. Measuring these dots give a lot of information. In first place the velocity of the endwall itself can be measured and in second place additional information about position and orientation can be extracted.

The endwall velocity equal to the dots fixed on the endwalls is measured. The measured velocity is only 0.4% greater than the experimentally prescribed value. This experimentally prescribed value has been defined as a 17.5 cm movement of a single endwall in exactly 49 s (thus $U = 3.57$ mm/s), corresponding to dimensionless parameters $Re = 0.25$ and $D_2 = 5$. The computer settings of the motion controller corresponding to these values are: 154 r.p.m. for the motor speed and total displacement of 250,000 steps. These values differ slightly from the values Speetjens used.

The additional position and orientation information is extracted here. A stack of the 2D calibration grids build up the 3D calibration volume. This 3D volume has still some degrees of freedom within the cylinder, see the left panel of figure 6.7. The largest degrees of freedom are in

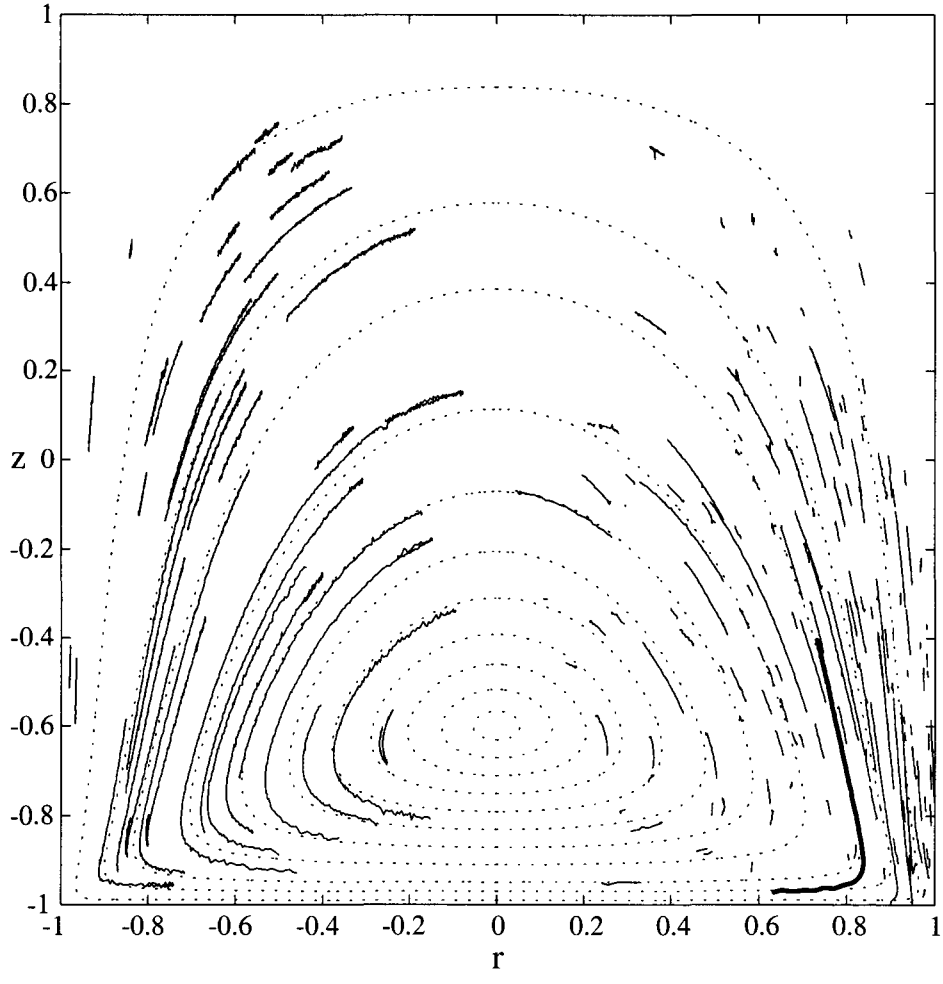

Figure 6.6: On the left side some long particle trajectories of experiment b are plotted in the rz-projection. On the right side all long trajectories found for the second session steady flow experiment are shown. Trajectories of the latter are much smoother. Dotted lines are numerical found streamlines.

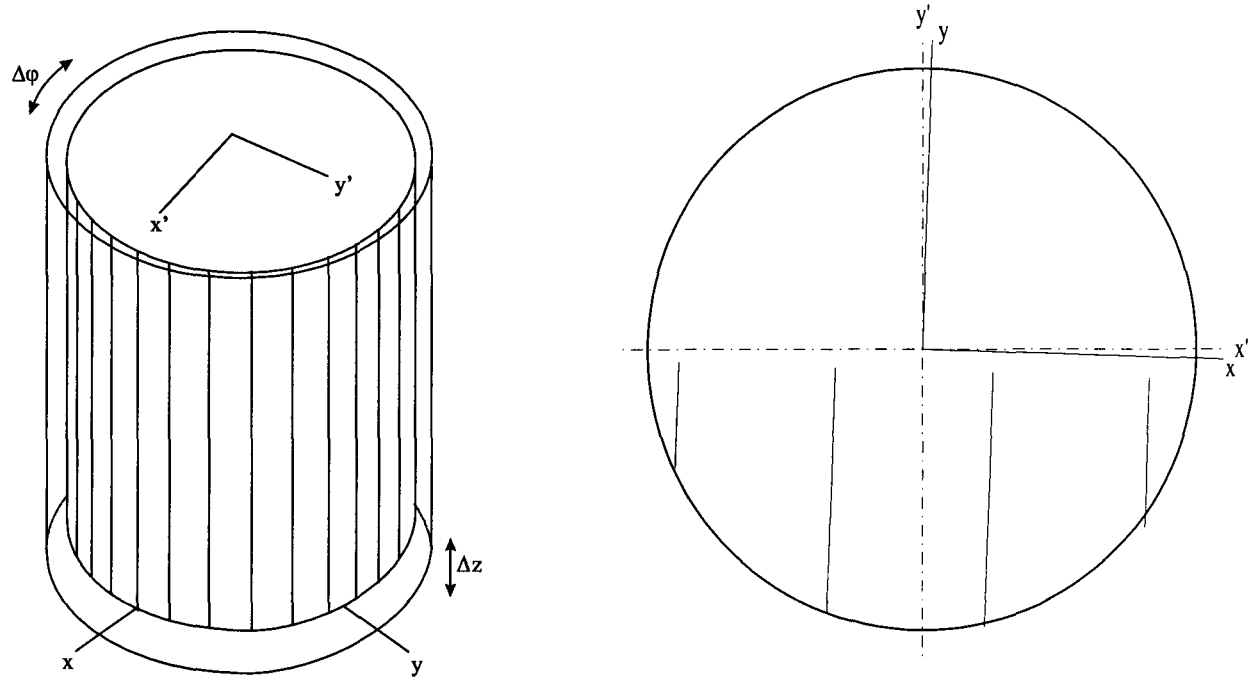

Figure 6.7: On the left side the calibration "volume" is shown, still having freedom in the directions Δz and $\Delta\varphi$. On the right side the angle difference between the grid coordinates and world coordinates is shown, by tracking four blobs fixed on the bottom endwall moving in the y-direction.

the directions Δz and $\Delta\varphi$. All other possible variations are very small, because the 2D grid is just about 1 mm smaller than the inner diameter of the cylinder itself. In fact all possible variations are variations between the known grid coordinates and the world coordinates to be measured.

All blobs fixed on the bottom wall should have coordinate $z = 0$ mm (or relative $z = -1$), which directly gives the correction needed for the z-coordinate. The average measured particle z coordinate, for particles fixed on the bottom endwall in this second session, is $z = -1.01$ mm. This means that all measured z values should be raised with 1.01 mm, thus $\Delta z = 1.01$ mm. Looking on the right panel of figure 6.6 shows that increasing the z coordinates of the particle trajectories a little would indeed lead to more correspondence with the dotted numerical streamlines, especially in the region of the centre of the eddy where particle trajectories are highly bending.

Following the fixed dots on a moving endwall in a certain direction gives the angle correction $\Delta\varphi$. Four blobs fixed on the bottom endwall are tracked on their movement in the y-direction. A view in the $x'y'$-plane is given on the right panel of figure 6.7. The angle between y' and y is on average $\Delta\varphi = 1.8^0$. This is a small angle but one should definitely correct for it, because all movements are very uni-directional oriented, when a single endwall is translated in a certain direction.

To show this correction method works, the correction is applied to a single long particle trajectory with deflection. The actual particle trajectory used, is the thick line indicated particle trajectory in figure 6.6. The difference between the endpoint of the measured trajectory and numerical simulated trajectory is calculated. Before the correction procedure the mismatch between the endpoints is 3.87 mm. When the correction in the z-direction is applied the distance is reduced to 0.94 mm and after angle correction reduced to 0.79 mm. This makes that the suggested correction for the position error in the z and φ-coordinate is very useful.

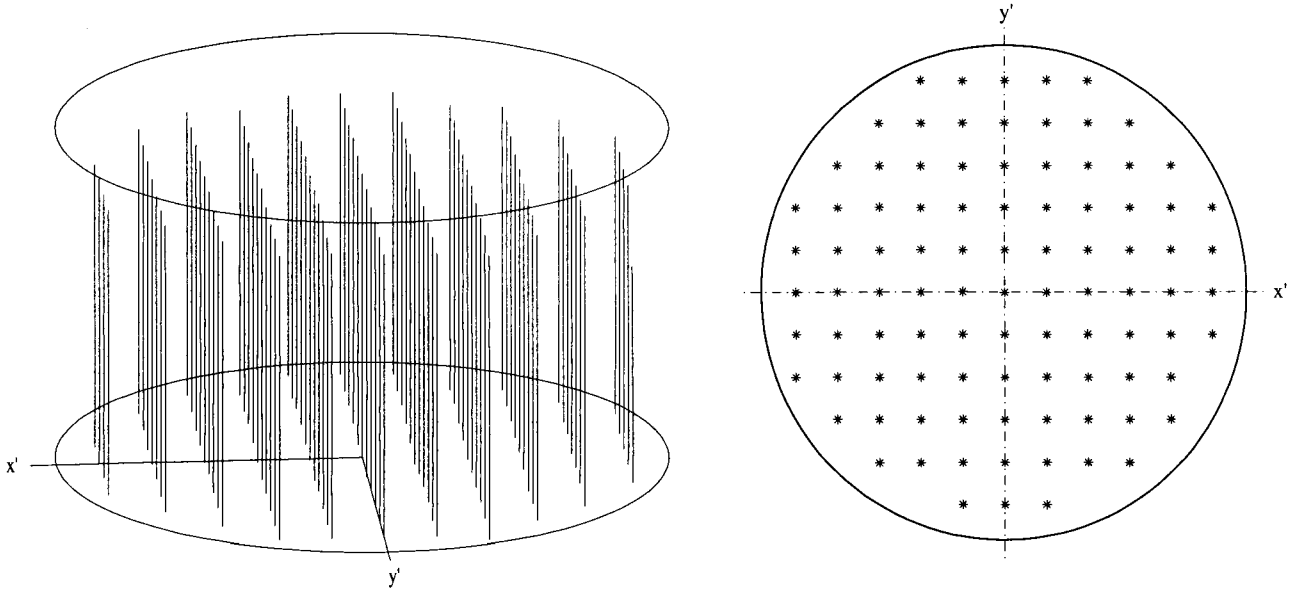

Figure 6.8: The grid point of the $2D$ grid are being used as particles. The $2D$ grid is moved in the z-direction. The "particle" trajectories are lines in the z-direction, shown on the left panel. The xy-projection can be seen on the right panel.

6.3 Measurement Checking methods

Two very valuable methods can be used to see if the PTV algorithm produces useful results. The first method checks the calibration grid points, to see if nothing went wrong during the calibration procedure. The second method is tracking particles under zero motion conditions, which gives accuracy results of the measurement technique.

First, the calibration grid method will be treated. A grid point can be seen as a "particle" moving in de z-direction, when a sequence of $2D$ grids in the z-direction is followed. All found particle trajectories followed in this way are shown on the left panel of figure 6.8. On the right panel the projection in the $x'y'$-plane can be seen. This projection shows that all grid points are almost perfectly visible. Positions between neighbouring grid points are nicely equidistant and exactly 6 mm. This xy-projection is equal to the $2D$ grid being used, this $2D$ grid is illustrated in figure 5.5. Of course these grid points are very well defined points, because the mapping functions are based on these points, but if the mapping functions contain any error this would directly be reflected in figure 6.8. Because the grid moves in the z-direction, the $x'$and y'coordinates of each particle should be fixed.

The standard deviation in the $x'$and y' coordinates for 93 followed grid points over 21 positions in z-coordinate is $\sigma_{x,y} = 0.01$ mm. The standard deviation in the z-coordinate is $\sigma_z = 0.05$ mm, where all measured grid points are fitted on lines by using the least squares method. In the first session the standard deviation is about three times bigger in the z-direction, while in x and y direction it is almost the same. The error in the z-direction is always bigger than in other directions, because the grid points are moving particles and a small camera angle has been used, both causing a higher error in the z-direction. The distance between a sequence of two 2D grid should be 3 mm within the accuracy of the used adjusting screw. The measured distance between 2 disks is equal to the velocity, when using a sample frequency of $f = 1$ Hz. The average measured velocity in the z-direction is $U_z = 2.996$ mm/s, which comes very close to the 3 mm of the adjusting screw.

In the second method samples of passive tracers particles are taken, while no forcing on the endwalls is applied. All measured particle positions should be stationary. Due to the Brownian

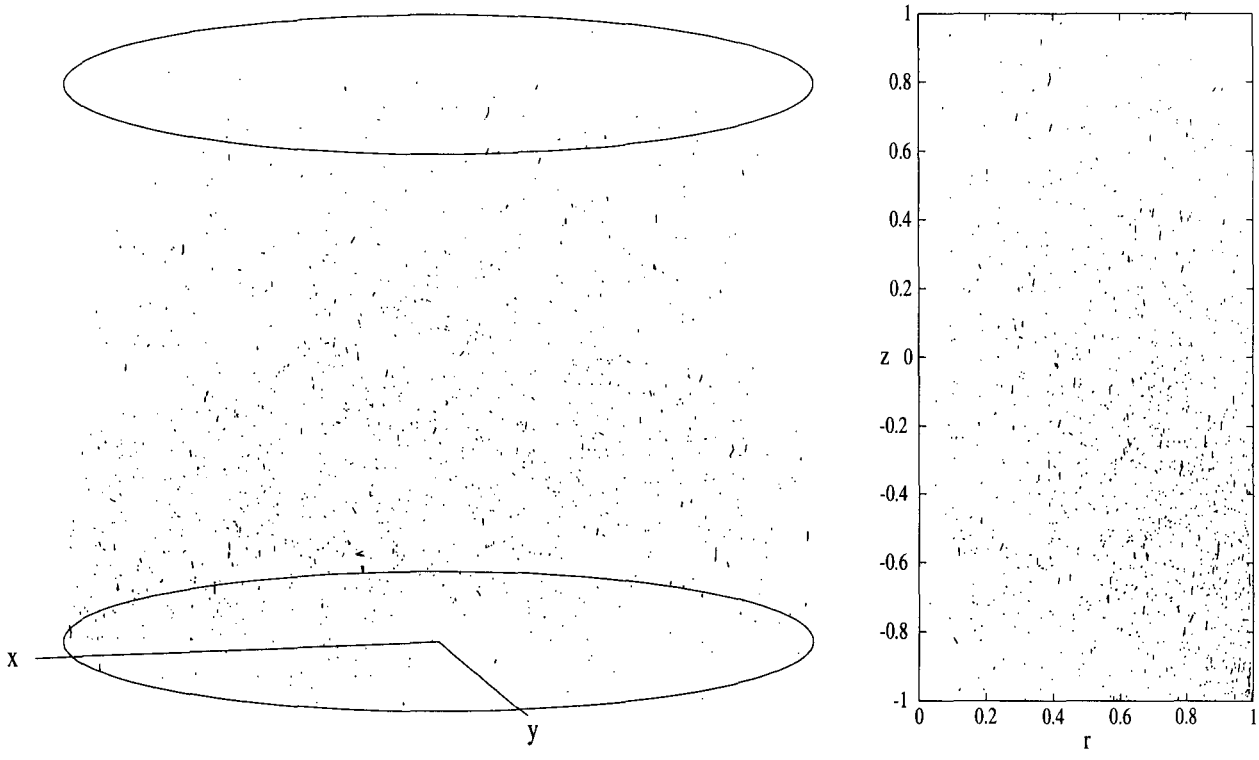

Figure 6.9: Eight seconds before the bottom endwall starts to move. All particle positions should be fixed. The biggest error is definitely in the z-direction, which is caused by the camera settings in the experimental set-up. On the left panel a perspective view can be seen and on the right panel the rz-projection.

motion, influence of gravity and probably some vibrations on the cameras, there will still be some motion.

The second session steady flow experiment starts with 8 seconds of no forcing at all. Within this time 3282 particles are detected and plotted in the left panel of figure 6.9. On the right panel the rz-projection is shown. For 122 particles starting in the first frame the position error has been calculated. The standard deviation in x' and y' coordinate is $\sigma_{x,y} = 0.002$ mm. The standard deviation in z-direction is $\sigma_z = 0.02$ mm. In the first session the error in the z direction is about 50% larger, in the other directions it is almost equal.

The position error in the z-direction is thus about 10 times bigger than in other directions. The z-coordinate is less accurate, because a small angle of 9^0 between the cameras relative to the z-coordinate of the cylinder axis has been used. Using an angle of 20^0 would lead to the best accuracy results and equal in all directions. The 50 % less accuracy in the z-direction is due to the mechanical vibrations on the cameras. When a camera is vibrating, most effects are seen in the z-direction, because that is the direction the camera makes the records of. It is possible to calculate an average particle velocity for the non moving particles, which is in for the second session in z-direction $V_z = 0.0 \pm 0.3$ mm/s.

6.4 Particle Size

The size of the used particles is very important. Bigger particles are usually more visible than smaller ones, however it is possible that bigger particles do not act as passive particles. When particles are to small, a sub-pixel accuracy in pixel coordinates can not be achieved. For the

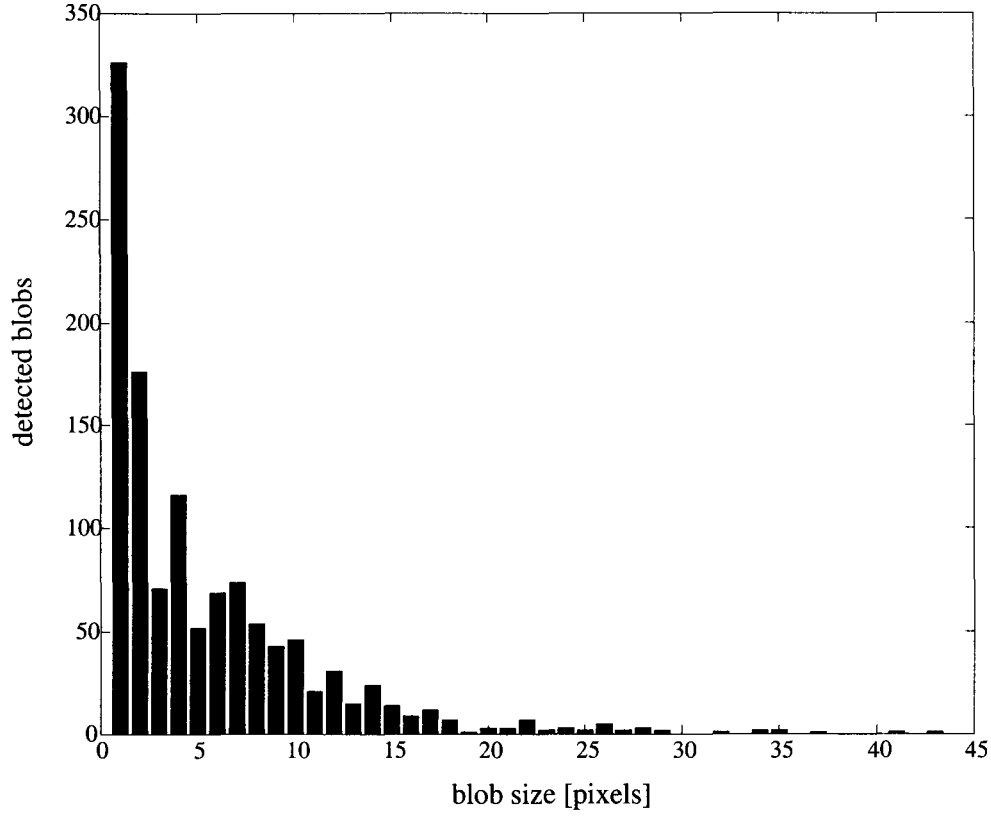

Figure 6.10: The blob sizes in pixels of 1201 detected particles on one camera.

mentioned reasons, some attention will be paid to the particle size in this section.

The used particles in the first two sessions have an average diameter of 250 μm. Using 70% of the enlargement factor $N = 1/7$, would result in a image particle with a typical diameter of 25 μm, corresponding to the a surface of about 5 pixels. A size of 5 pixels is enough to apply the gray value weighted centre of gravity and thus knowing the particle position within sub-pixel accuracy. A blob size measurement leads to the same average results, however there is a large spread on it. A typical example, of the measured blob sizes of all blobs found on one camera image, is given in figure 6.10. 27 % of the detected particles have a blob size of just one pixel and thus no sub-pixel accuracy can be achieved for these particles. The median blob size is 4 pixels, which roughly means that only about half the number of the detected particles positions are known within an accurate sub-pixel accuracy.

For this problem there exist two controversial solutions. The most obvious way is by increasing the blob size, so that also the smallest particles are greater than just one pixel. The other way is using particles so small that diffraction takes over the role of reflection, therefore particle sizes of about 10 times the wavelength of light are required. The more intense a light source, the greater detected particles look. The best way to achieve this is by using an intense laser sheet. Two main disadvantages are: a more complex experimental set-up and the measurement technique itself becomes quasi two dimensional, which means only good velocity measurements are possible in the plane of the laser sheet.

Using bigger particles has been studied in more detail. An experiment with some bigger particles has been carried out. These particles are two times bigger than the particles used in the first and second session experiments, they have an average diameter of 500 μm. Two camera samples are shown in figure 6.11. The clear big particles are the 500 μm particles, the smaller less clear particles are the 250 μm particles being used in the first two sessions. The time between the two taken

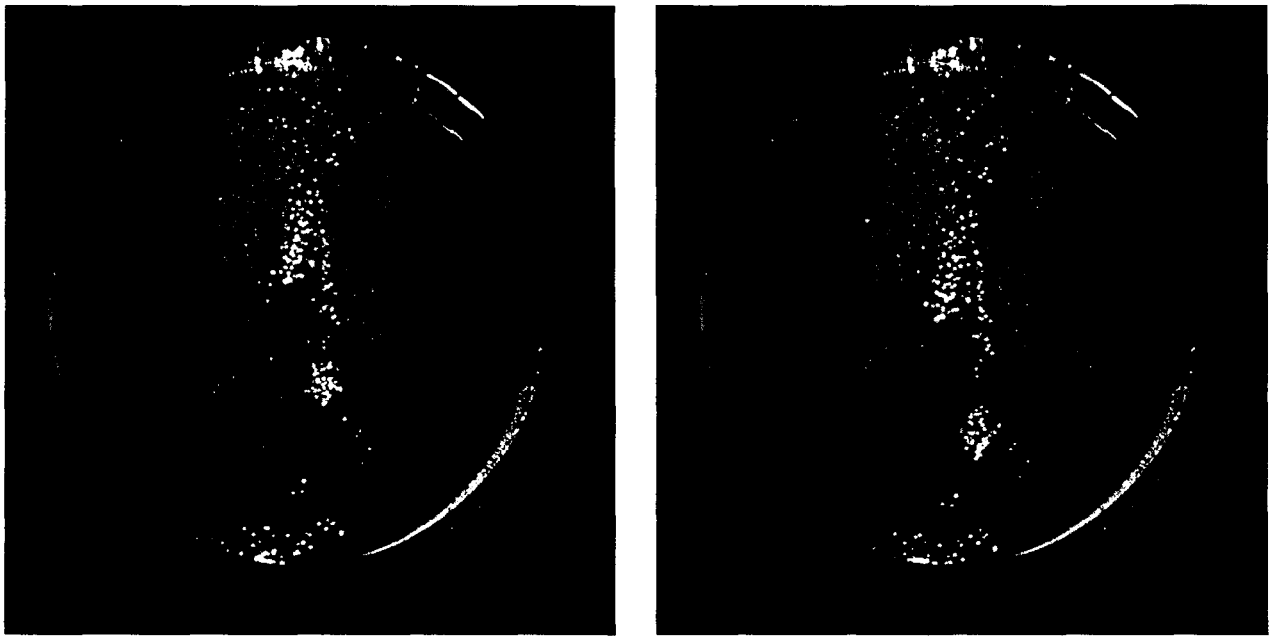

Figure 6.11: Time between the left and the right image is 300 sec. The big particles are going down due to the gravity forces. The smaller particles are almost stationary.

samples is 300 s. It can be seen that the big particles drop too fast.

A rough approximation of the velocities of the small and bigger particles can be made by using both camera shots. The small particles have an average velocity in the y direction of $V_y = -0.002$ mm/s and the bigger particles $V_y = -0.02$ mm/s. The bigger particles drop 10 times faster than the smaller ones. A tolerance in the y-direction of 1 mm would lead to the restriction that an experiment with the bigger particles may last maximal 50 s. This restriction is just within the limits for doing a steady flow experiment but nothing more.

A movement of a spherical particle with radius r in a Stokes flow, whereupon no external forcing (endwall motion) is applied, is determined by the following three forces: gravity force, upward force and the Stokes friction force. The upward force is a force in the y-direction, making a particle weight less in the fluid. On a moving particle a friction force is exerted: the Stokes force. This force is given by $F_s = -6\pi\eta r V_y$. Due to this friction force the resultant of the forces on the particle becomes equal to zero after a while, from then the particles move at a constant velocity. The characteristic time scale to reach this final velocity is given by

$$t^* = \frac{2\rho r^2}{9\eta}, \tag{6.2}$$

with ρ the density of the fluid and r the radius of the spherical particle. A typical time value is $t^* < 0.1$ ms for the currently used experimental set-up. It can be said that a particle is always moving with its final velocity. This final velocity is given by

$$V_\infty = \frac{2}{9}(\rho - \rho_s)\frac{gr^2}{\eta}, \tag{6.3}$$

with ρ_s the density of the particles. The radius r of the particle in 6.3 is very important, because it appears as a square. When the radius of a particle is twice as large, the difference between particle density and fluid density should be four times smaller, when accepting a certain tolerance for V_∞. This explains why the bigger particles drop and the smaller particles do almost not. The density of the used silicon oil is 28 kg/m^3 less than the density of water. Commonly used particles have the

same density as water and therefore drop too fast in the silicon oil, which makes them useless for experiments. Special particles having the same density as the silicon oil should be used.

There is another problem when using "big" particles, because these particles cannot be considered passive tracers anymore. When the fluid flow has a velocity relative to the particles, these particles exhibit a lift force perpendicular to the direction of the flow, caused by shear or vorticity in the fluid flow. When $Re < 1$ the McLaughlin approximation can be used to estimate the lift force, see Simons (1995). By using this lift force and the Stokes drag force, an asymptotic velocity in the y-direction can be calculated. The asymptotic velocity equation in the McLaughlin form is given by:

$$u_y = \frac{3}{2\pi^2} u_x T J(\epsilon) \qquad \text{with} \qquad T = \sqrt{Re_\kappa} = r\sqrt{\frac{\kappa}{\mu}}, \tag{6.4}$$

with κ the local linear shear coefficient and $J(\epsilon)$ a function of $\epsilon = \frac{\sqrt{\kappa\eta/\rho}}{u_x}$, which can be regarded as a non-dimensional lift force, which has the value 2.255 when $\epsilon \to \infty$.

Most of the shear is in the region of the moving endwall. Therefore the distance between the centre of the primary eddy and the moving endwall in the plane $x = 0$ will be used as typical length scale L, resulting in $\kappa = \frac{u_x}{L}$, with the endwall velocity u_x chosen as a characteristic velocity. This makes the asymptotic velocity equation (6.4) linear for the particle radius r and to the power of $1\frac{1}{2}$ for the applied endwall velocity u_x. Substitution of the limit value 2.255 of J, $L = 15$ mm, $u_x = 3.57$ mm/s and $\mu = 2.10^{-3}$ m/s^2, lead to $u_y = 0.013r$ as approximation for the velocity orthogonal to the plane of motion.

Again accepting a tolerance of 1 mm, but now for when doing a complete forcing protocol D experiment, thus $t_{exp} \geq 196$ s, would lead to a particle radius restriction of $r \leq 0.38$ mm. Both particle sizes used in the experiments satisfy this restriction. It is always recommended to use particles smaller than 1 mm always, because otherwise these particles do not act like passive tracers anymore.

6.5 Quality factors

To determine the quality of a $3D$ PTV measurement two quality factors can be introduced, comparable to the quality factors of $2D$ PTV. The first quality factor q_i determines the image quality. A good image quality means low noise and well detectable particle blobs on an image. Choosing the right particles and using a bright light source is important. Using the whole gray scale range of the cameras is important to achieve a sub-pixel accuracy. Last but not least the depth of field is very important. This factor has the greatest influence on the image quality q_i. Depth of field of future experiments can be improved using equation (5.17). More particles are found near the bottom wall, this is probably caused by the choice of depth of field, but it is also related to the calibration itself, where less grid points are found near the cylinder top. Improvements are possible by using a more intense beam, which allows for a higher relative aperture.

The other quality factor is the sample quality q_s. While the q_i largely depends on the experimental settings, this q_s is important when applying the $3D$ PTV algorithm. The quality factor q_s will be introduced as

$$q_s = \frac{\widehat{d}_n}{\Delta x}, \tag{6.5}$$

with $\widehat{d}_n$ the average mean distance between the particles, which is defined in equation (5.4), with $C = 1$ and Δx is the maximum displacement between two frames. Note that $\widehat{d}_n$ depends on the particle seeding density and thus q_s still depends on the experimental settings. The maximum displacement Δx will be chosen equal to the displacement of an moving endwall between a sequence of two processed frames.

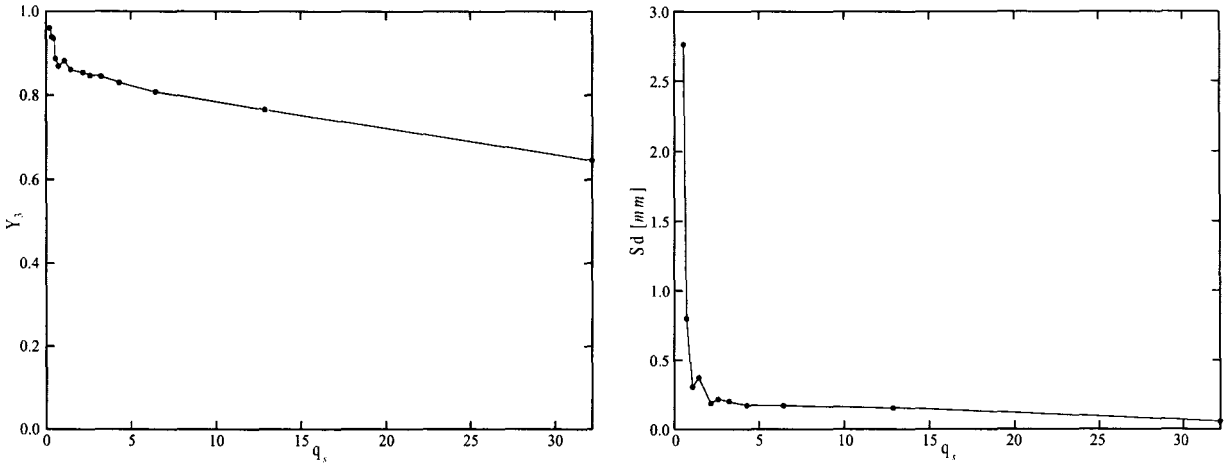

Figure 6.12: On the left side Y_3 is shown as function of q_s. On the right plane the standard deviation of a fit through the found particle trajectories is given as a function of q_s.

$q_s > 1$ is required to gather good results with only a few mismatches. The higher the quality q_s is the better the found particle trajectories are. When q_s becomes too large only a few particle trajectories will be found, because the distance between two frames Δx becomes very small and too many steps have to be taken. Due to the very small steps the position error will also grow important. When the sampling quality q_s decreases, the spatial resolution decreases, because larger steps are taken. This troubles experiments with a very low particle density, because relatively large steps have to be taken to get particle trajectories with a reasonable value for q_s. An optimal sampling quality q_s can be expected somewhere around $q_s = 3$.

To show how this q_s works, experiment b of session one is used as an example. Therefore Δx is written in the following form

$$\Delta x = \frac{skip}{f} U, \tag{6.6}$$

with U the bottom endwall velocity, f the camera sample frequency and *skip* the number of frames being skipped when using the algorithm. Here $skip = 1$ means that all images are used. The *skip* is used as a variable, all further setting in the configuration file are held constant. The most direct result is gathered, when plotting q_s versus yield. Detecting a particle in a sequence of minimal three frames will be used here as a criterion, so a velocity field could have been derived. On the left plane of figure 6.12, Y_3 is plotted versus q_s. This Y_3 is a nicely monotone decreasing function of q_s. When q_s increases only the better (less noisy) particle trajectories will remain.

Twenty particle trajectories are fitted on curves in the rz-plane for every used *skip*, the average standard deviation measured has been used as an indication to determine the reliability of the found trajectories. The results are given on the right plane in figure 6.12. Lower values of q_s have higher standard deviation values representing a higher probability of mismatching. The long trajectory criterion with less mismatches is the combination of both figures. More longer trajectories are found when q_s is low, which comes down to going through the experiment with large steps. The steps should not be too large, because mismatches occur more often and determination becomes less accurate. So there should be some optimal value for q_s.

Long particle trajectories are of real interest here and not finding particle trajectories just long enough to measure a velocity field. Therefore the average tracking length measured in frames is plotted versus the parameter q_s on the left plane of figure 6.13. It is remarkable that shape of the curve looks the same as the performance curve of $2D$ PTV, which can be found in Zoeteweij & van der Plas (2001). The position of the maximum is situated on a somewhat higher q_s, because for C

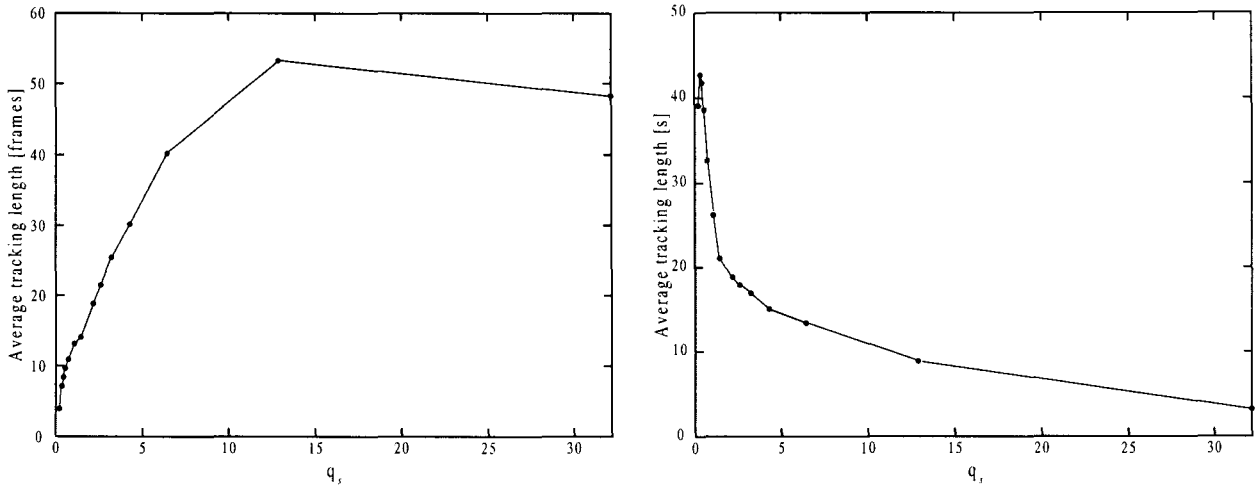

Figure 6.13: Average tracking length in frames as a function of q_s is shown on the left side. On the right side the average tracking length measured in seconds is shown as a function of q_s.

a rough approximation is made. The performance of $2D$ PTV has been defined as $\eta_{ex} = \frac{\sqrt{Y_3}}{\sigma_{u,v}}$. Here a more straight forward method will be used.

The algorithm itself generates good results, when the average tracking length is long. When large steps are taken, many mismatches occur and will reflect in a not so long average tracking length, on the other hand when steps are taken too small, many matchings are needed and therefore particle trajectories are likely to be lost, due to Brownian motion. In the subsection 6.1.2, the path length is defined as a length in time, because that is the parameter of interest. The average path length defined in time units is plotted versus q_s on the right panel of figure 6.13. The range $1 < q_s < 10$ should be used to find long particle trajectories. For higher values of q_s the average particle tracking length measured in time becomes very small, because of the high quality constraint. It is always important to check if q_s is in the right range, especially when applying the tracking algorithm. But also before doing an experiment, because it is important to choose the right particle density.

Varying the particle density causes a change in $\widehat{d_n}$. When for example a low density is used, a high *skip* must be used to maintain a certain sample quality. This higher skip rate causes a lower spatial resolution of the particle trajectories measured. Instead of varying the *skip* it is also possible to vary the particle density, in this way the measurements a, b, c, d can be compared. In the left figure of 6.13, this reflects in point b with $q_s = 18.9$ (right from the top), point a with $q_s = 24.6$ (more right from the top), point c with $q_s = 12.3$ (left from the top) and point d with $q_s = 7.55$ (more left from the top). Using roughly 200 detected particles ($\sim$ experiment b) can be seen as an optimum.

The sampling quality factor of experiment b, which is described in paragraph 6.1.2, is $q_s = 18.9$. This is an extremely high value, especially when searching for long particle trajectories expressed in time, see the right panel of figure 6.13. As mentioned, q_s should be in the range $1 < q_s < 10$. Increasing the *skip* from 5 to 30 leads to $q_s = 3.1$, which is still large enough to find reliable particle trajectories. To compare the results, the particle trajectories with $q_s = 18.9$ (left) versus the particle trajectories with $q_s = 3.1$ (right) are plotted in the rz-projection figure 6.14.

Most important here is the increase from 36 to 75 complete particle trajectories found. Except from a few random jumps, the particle trajectories found are qualitatively good. If desired, these small jumps can be filtered by doing a simple curve fit. Due to the high *skip*, less wiggles, caused by camera vibrations during the first session experiments, are found. More (relatively) fast moving particles are found when lowering the q_s, as can be seen on the bottom of the cylinder, see figure 6.14, were more particle trajectories are found than for higher values of q_s. This example shows the

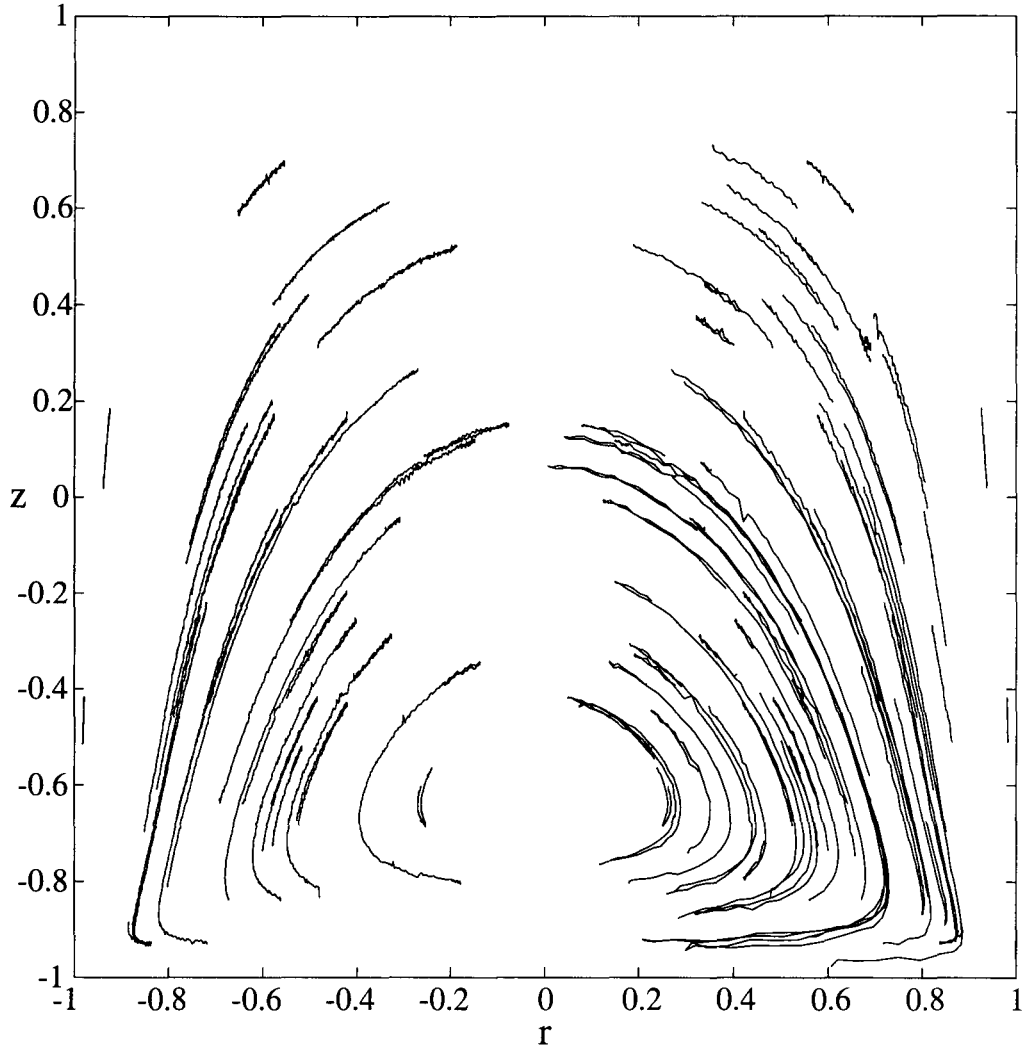

Figure 6.14: All complete particle trajectories of experiment b projected in the rz-plane. On the left, all 36 complete particle trajectories with $q_s = 18.9$ are shown. On the right, all complete 75 complete particle trajectories with $q_s = 3.1$ are shown.

importance of using q_s as a tool to find long particle trajectories. It is possible to reduce q_s even more, to for example $q_s = 1.6$. In that case 89 complete particle trajectories are found. However, at such a low q_s some trajectories are mismatched and the spatial resolution gets worse. Therefore $q_s = 3$ can be seen as an appropriate value.

6.6 Summary

For both measurement sessions holds, that using a low particle density and turning off the prediction scheme leads to the best results. In the first session, 36 particles (after optimization 75) have been followed during the complete steady flow experiment. This is a lot more than the 11 particles Speetjens could follow during his steady flow experiment. In the second session only one complete particle trajectory is found, because of the high particle density. The particle trajectory segments are smoother than the ones found in the first session, because the influence of mechanical noise is reduced. When using low particle densities, using a prediction scheme is no more needed. It is even better when no prediction scheme is used. This is advantageous, because this allows measurements on more complicated fluid flows, without predicting anything.

The fluid flow depends entirely on the boundary conditions. For an accurate position measurement of these boundary conditions, dots have been painted on both endwalls. These dots give detailed information about the $3D$ position of the endwalls, making comparison with numerical simulations much more accurate. An accessory effect is that the endwall velocity can be verified.

The correctness of the calibration files and the algorithm can be checked by tracking the grid points of the $2D$ grid. These grid points should be moving nicely in the z -direction.

An accuracy test has been carried out, by tracking particles seeded in the fluid while no forcing on the endwalls is applied. Most accurate are the x and y directions, where errors are roughly 10 times smaller than in the z-direction. The measured error in the z-coordinate of the particle position is at most 0.03 mm. An average pixel diameter on the CCD camera is about 0.01 mm, corresponding to a length in the object space of 0.1 mm. This sub-pixel accuracy is achieved by using the gray weighted centre of gravity.

The particle size is important: it should be large enough to obtain sub-pixel accuracy. On the other hand, the typical size of a particle should be smaller than 1 mm, because larger particles do not act like passive tracers. For smaller particles the particle density is less critical, which is shown in equation (6.3).

All experimental parameters and all tracking parameters set in the configuration file, form a complex system. Using the most important parameters, two quality factors have been defined. The first quality factor is the image quality q_i, which largely depends on the experimental settings, like light source, depth of field, the used particles and the optical settings.

The second quality factor is the sampling quality q_s, which is determined by the configuration parameters and the particle density. The sampling quality gives a good indication of the accuracy of the results. The sampling quality should be larger than 1, otherwise too many mismatches occur. On the other hand it should not be chosen too large (>10), because the larger q_s, the fewer trajectories are found, as shown in figure 6.12. Using an appropriate value for q_s led to a large increase in the number of complete particle trajectories found. In total 75 complete particle trajectories without mismatches are found using $q_s = 3.1$.

Chapter 7

Conclusions and Recommendations

7.1 Conclusions

The performance of the $3D$ PTV measurement technique is improved considerably, with respect to tracking long particle trajectories. Steady flow has been used to perform an accuracy assessment on the $3D$ PTV measurement technique. The particle trajectories found are highly comparable to their numerical simulations. To find interesting Lagrangian information, the four-step cyclic protocol D has been introduced. A measurement using this protocol led to particle trajectory segments only, because in this experiment the particle density was too high.

Using a steady flow, 75 particles have been followed during a complete experiment. This is a lot more than the 11 particles Speetjens (2001) could follow in his steady flow experiment. The three most important reasons contributing to this improvement are: a low particle density ($\sim$200 particles), no temporal extrapolation prediction and an optimal value for $q_s(\sim 3)$.

$3D$ PTV is proven to be a very accurate measurement technique. Results are shown to be sub-pixel accurate and the long particle trajectories are highly comparable to their numerical simulations, because boundary conditions have been measured and compensated for.

Based on the 75 particles, which have been followed during a complete steady flow step using 190 initially detected particles, it can be expected that about 4 particles could have been followed during a complete forcing protocol D. Thus it can be concluded, that the currently used experimental $3D$ PTV set-up can be used to find particle trajectories long enough to follow one complete forcing period in protocol D.

Protocol D has been investigated analytically and numerically. Periodic-1 lines are found and compared to the periodic-1 lines Anderson (1999) found in his cubic domain. Tools developed by Speetjens and others, are proven to be useful for investigating this protocol. The mixing properties of protocol D are inferior to the mixing properties of the protocols B and C, introduced by Speetjens. However, protocol D can be used for long-time experiments, while the protocols Speetjens introduced are ill-suited for this purpose. In terms of integrable states, which can be found in Speetjens (2001), protocol D can be classified as an integrable state II system, just as protocol A and protocol B.

A lot of pioneering work has been done with respect to $3D$ PTV. This report can be used as a starting-point for a user's guide for $3D$ PTV. Results gathered till thus far are very promising. It is reasonable to expect that much more longer particle trajectories are found, when the light intensity and particle size are increased. A more intense light beam should be used to make particles more visible and increase the depth of field by using a higher relative aperture. Specialized particles with a diameter of 0.5 mm should be used because they are more visible, the difference between particle and noise is more pronounced and particle positions are more accurate because a better sub-pixel accuracy can be achieved.

7.2 Recommendations

Although the camera frequency used in the experiments is 30 Hz (later 12 Hz), the effective sampling frequency is reduced to 1 Hz due to the high skip factor. In order to make fine-tuning of q_s still possible, it is advised to use a camera sampling frequency of 6 Hz. Lowering the camera sampling frequency saves a lot of disk space.

The following three relatively simple improvements will lead to considerably more long particle trajectories:

- use a more intense light source, such as a 500 W slide projector or even a sky-spot. However, a brighter light source will cause more unwanted reflections;
- use round particles with a diameter of about 0.5 mm, having the same density as the used silicon oil;
- improve the blob detection scheme in the tracking algorithm. This makes blob size selection possible. Currently, the blob detection scheme is limited to 10 frames.

The three suggested improvements are very promising, especially when all three are implemented. When even more improvement is desired after applying these improvements, more rigorous changes in set-up are needed. Two options are: use a fourth camera and try to improve the depth of field.

Virant (1997) mentioned that four cameras are almost obligatory when searching for Lagrangian particle information. This indicates that using a fourth camera can be profitable. It will cost about 50,000 euro's, which makes this solution quite expensive. A special frame should be designed to attach the cameras. Such a frame can also be very useful when using three cameras, making the cameras more steady.

Depth of field is hard to optimize. Apart from using more light, the most obvious way is decreasing the enlargement factor by using a larger cylinder. Therefore, the complete experimental set-up should be enlarged. This will not result in a better depth of field alone, but the angle between camera and optical axis can be increased too, leading to a higher accuracy performance in the z-direction. Also the use of a fourth camera is more effective, when using a larger cylinder.

Appendix A

3*D* PTV Configuration file

```
EExperimentTag          # EExperimentTag
expl.                   # basefilename (bfn)
0                       # begin
23                      # end
1                       # skip
0.08333                 # time between frames
EEndTag                 # EEndTag
4 4                     # minmax substractie filter: int xsize, int ysize (window = 2n+1)
1 50 5                  # blobdetect1: int min, int max, int threshold
1 50                    # blobValidator1: int min, int max
1 50 4                  # blobdetect2: int min, int max, int threshold
1 50                    # blobValidator2: int min, int max
1 50 5                  # blobdetect3: int min, int max, int threshold
1 50                    # blobValidator3: int min, int max
3 24 3 4 3 8 4 expl.    # F3DLineMapper: double dZ, int nZCalibr, int nCam, int imOrde, int imCrOrde, int lnOrde, int lnCrOrde, bfn
0.1                     # F3DLocator: double maximummatchingrange
3.5                     # matcher: double maximummatchingrange
1 1.0 0.03              # FPredictor: order, gaussian delta, minimum particles
                        # empty line required
```

Figure A.1: The 3*D* PTV algorithm configuration file.

Figure A.1 shows how a 3*D* PTV configuration file should look. The file contains 19 lines all describing what the 3*D* PTV algorithm has to do. Note the explaining text on the right should be placed under the empty line 19 or must be deleted otherwise the configuration file will not work. The basefilename is chosen in line 2, here 'expl.' is chosen and thus this configuration file should be named 'expl.cfg'. The output of the 3*D* PTV algorithm will be 'expl.log' and 'expl.prt'. The *log* file contains information about what the algorithm did, odd things can easily be detected by exploring this file. The *prt* file contains all the information about the tracked particles. The post processing program *f3dpostES1.0new* can be used to extract the particle information and put it in a certain form.

The lines 3 and 4 define the first and the last maximal possible frame number (depending on skip) to be processed, respectively. Line 5 defines the (frame)skip, telling how many frames there will be skipped before processing the next frame. The time between two successive frames is given in line 6, which is determined by the used camera sampling frequency, where in this case 12 Hz has been used, resulting in the time between two frames of $1/12$ s $= 0.08333$ s.

Line 8 defines the window size for the square min-max sub filtering procedure. In line 9 the minimum and maximum allowed blob size for camera 1 are given and a low single threshold will be subtracted after the sub-min max filtering procedure. Note that minimum and maximum blob size does not work when applying the peak detection scheme. In line 10 the minimum and maximum blob sizes are repeated. Lines 11, 12 and 13, 14 are the same parameters for the cameras 2 and 3,

respectively. Eventually different values can be used for each of the cameras.

In line 15 a couple of camera line mapping parameters are defined. Double dZ is the distance between two successive $2D$ calibration images, int nZCalibr represent the taken number of calibration image positions, int nCam is the number of cameras being used, the two numbers thereafter represent the mapping order $(= n)$ x^n, y^n and the mapping cross order $(= n+m)$ $x^n y^m$, translating the $2D$ mapping functions from pixel coordinates into world coordinates, respectively, the last two numbers are the same but now to attach the particles to the closest perspective lines.

Line 16 defines the maximum matching distance of the detected particles to the perspective lines, used as a square, which means that the maximum matching distance of the matching lines here is $\sqrt{0.1}$ in the physical space. In line 17 the maximum matching distance is given, this value depends on the used skip. A good measure for this, is the displacement of the moving endwall between two successive processed frames. In line 18 the prediction parameters are declared. If the order number is 1, no prediction will be used. Order 2 reflects a linear temporal extrapolation. For the spatial interpolation the Gaussian approach will be used, with σ as Gaussian delta and minimum particles is used as a kind of a threshold to decide using the approximation or not. The last line is a white line.

Appendix B

How to find all particle trajectories of a $3D$ PTV experiment

```
#!/usr/bin/awk -f
BEGIN{
        if(ARGC!=4)
        {
                print;
                print " totaltrack, Eindhoven University of Technology, Arnold van der Starre, (c) 2002"
                print
                print " usage: samples prtfile outputfile";
                exit;
        }

    {   command = sprintf("/home/arnold/bin/f3dpostES1.0new  0 %d f %s >> %s",ARGV[1],ARGV[2],ARGV[3]);
            print command;
                system(command);
                command = sprintf("echo >>%s",ARGV[3]);
                system(command);
        }
        for(i=1;i<=ARGV[1]-1;i++)
        {
#               command = sprintf("echo >>%s",ARGV[3]);
#               system(command);
                command = sprintf("echo %04d >> %s",i,ARGV[3]);
                system(command);
                command = sprintf("/home/arnold/bin/f3dpostES1.0new  %d %d n %s >> %s",i,ARGV[1]-
i,ARGV[2],ARGV[3]);
                print command;
                system(command);
                command = sprintf("echo >>%s",ARGV[3]);
                system(command);
        }
  }
```

Figure B.1: A method to write all measured particle trajectories in just one file.

By using a clever combination the options f and s in the post processing routine *f3dpostES1.0new* all particle trajectories of a complete experiment can be written to a single file. This can be done by using the routine *totaltrack* shown in figure B.1. When using this routine, the path settings should be adapted. The routine has been created by using AWK.

usage : totaltrack samples prtfile outputfile.

This routine starts to find all particle trajectories of the 'prtfile' beginning in frame 0 and following them until the end of their trajectories or until framenumber *samples -1* has been reached

and write it to 'outputfile'. In every following step, first the frame number will be written to 'outputfile' and thereafter all newly found particles belonging to that frame and corrected for their path lengths will be written to 'outputfile'. All particle trajectories written in 'outputfile' are separated by a white line. For the parameter 'samples' principally all values can be used, however always use an positive integer value at least 2 smaller than the total number of processed samples by the $3D$ PTV algorithm, because the end of the 'prtfile' file contains some errors.

Now all particle trajectories of a complete experiment are written into a single file in a chronological order. To work with the file it has to be read by some data processing program, therefore Matlab will often be used. Reading data with irregular forms like this in Matlab is not very common. First idea is trying to put all information in a $3D$ array, because three variables can be used, namely: Particle number, Particle length and Particle position, with the particle position written in 4 coordinates x, y, z and some *error*. Where the error is the measured square distance between the particle and the nearest found perspective line. The framenumber can be put in $1D$ array later on. The gathered $3D$ array grows incredible large and is barely to handle, because all dimensions must be set maximal, while pathlength for example highly alters. Using a cell array forms a good alternative. In this array every cell number represents a particle, containing all the particle positions and the particle length in a dynamic $2D$ array. Using the cell array makes it is possible to read all found particle trajectories of a complete experiment in Matlab.

This reading in is far from trivial and therefore a possible reading procedure will be given here. The problem will be tackled by reading first the 'outputfile' rule by rule and keep information as blocksize and frame number in mind. Thereafter the information is read again but now in block form, this can be done because now all array sizes are known. How this can be done, is shown in figure B.2. This routine needs the 'outputfile' containing the particle trajectories only. Some additional information is needed when explicit time information is wanted. This additional information is given by: the used camera sampling frequency $freq$, the $frameskip$ used in the $3D$ PTV configuration file and the first frame where particles are seen to be moving for the first time, as variable $firstMframe$. The output of this routine is cell array C containing all particle trajectory information. Time information is given in a very basic form as variable $pframe$, telling in which frame particle i is detected for the first time. Using $C\{i\}$ gives the complete particle trajectory of particle i. The x, y, z and the *error* position coordinates are placed in the rows of the cell element $C\{i\}$ the columns represent the sample moment. The Matlab command 'plot3' can be used to plot $3D$ particle trajectories. For example 'plot3(C{i}(1,:),C{i}(2,:),C{i}(3,:))' plots the complete $3D$ trajectory of particle i in the measured coordinate units.

Till thus far nothing has been done with the additional time information. Beginning times and ending times of the particle trajectories can be calculated by using the additional information. A routine to do so is given in figure B.3. This routine determines all the beginning times $t0(i)$ and ending times $t\_eind(i)$ of all individual particles i. The used time scale is made dimensionless by using the dimensionless displacement D_2 as measure, which is in the steady flow case ($n = 1$) equal to the final time t_total of the experiment. The beginning and ending times of the particle trajectories often form a good criterion whether particle trajectories are useful or not.

```
close all
clear all

%inlezen willekeurige file in blokken met verschillende lengten

pathname = ['C:\Afstud\matlabfiguren\experimenten\'];
filename =['zeromotion']
firstMframe = 4;
freq = 30:
frameskip = 5;

file = [pathname filename]

fid=fopen(file,'r');
n_part=1;
blocksize(1)=0;
beginframe(1)=0;
j = 1;
while feof(fid)==0
 a = fgetl(fid);
 p=length(a);
 if p>10;
  blocksize(n_part)=blocksize(n_part)+1;
 end
 if (p==0) & (blocksize(n_part)>0) ;
  n_part=n_part+1;
  blocksize(n_part)=0 ;
 end  if p==4;
  beginframe(j)= n_part;
   J=j+1;
end
end

frewind(fid)
n_part = n_part -1

k = 1;
for i=1:n_part;
 if beginframe(k)==i  jan=fscanf(fid,'%f',[1,1]);
  if k<length(beginframe)
   k = k+1;
    for m=1:j
     if beginframe(k)==beginframe(k-1):
      jan2=fscanf(fid,'%f',[1,1]):
       if k<length(beginframe);
        k = k+1;
       end
     end
   end
  end
end
 pframe(i)=k-1;
 C{i}=fscanf(fid,'%f',[4,blocksize(i)]);
end
fclose(fid);
```

Figure B.2: A Matlab routine putting all particle positions of every single particle trajectory in cell array C. Each element $C\{i\}$ contains the complete position information of particle i. Time information in a basic form is given by $pframe$.

```
i2=1
if i2==1

n = 1;
D2 = 5;
t_total = 49;

beginframe(length(beginframe)+1)=n_part+1;

 for i=1:n_part
  t0(i)=(pframe(i)-firstMframe)*frameskip*n*D2/(freq*t_total);
   if t0(i)<0
    t0(i)=0;
   end
  if t0(i)>n*D2
   t0(i)=n*D2;
  end
 end

t_eind(1)=0;
for i=1:n_part
 t_eind(i)=(pframe(i)+blocksize(i)-1-firstMframe)*frameskip*n*D2/(freq*t_total);
  if t_eind(i)<0
   t_eind(i)=0;
  end
  if t_eind(i)>n*D2
   t_eind(i)=n*D2;
  end
 end

end
```

Figure B.3: An additional routine to determine the beginning and ending times of all the particle trajectories.

Appendix C

Addition to the non-inertial limit of protocol D

In paragraph 4.2 is concluded, that both planes $x = 0$ and $y = 0$ are planes of time-reversal symmetry. This conclusion is based on the analysis of tracer particles released on the periodic lines, followed a complete forcing in protocol D. Times of special interest are: $t = T/8, 5T/8$ (symmetry plane $y = 0$) and $t = 3T/8, 7T/8$ (symmetry plane $x = 0$), thus always half away each forcing step. To prove these planes really are the planes of time-reversal symmetry, an analytically analysis is given in paragraph C.0.1.

Recently, it appeared that in the limit of $Re = 0$ the simulated Poincaré maps by using the spectral method are very different to the Poincaré maps simulated by the semi-analytical Shankar method. The Shankar method is used in paragraph 4.1. In paragraph C.0.2 this problem is further investigated.

C.0.1 Analysis of the symmetry planes

In paragraph 3.2 the analytically analysis to find the 180^0 rotation symmetry along the line L_s is given. This analysis is carried out, starting at $t = 0$ till $t = T$ under forcing conditions forcing protocol D and exploiting the symmetry relation $\widetilde{S}$, leading to the rotation symmetry along the line L_s. The special times, each time half away a forcing step, can be exploited, because the forcing protocol D is periodic and repetitive. For example one can start at $t = 1T/8$ and follow the flow till $t = 9T/8$, this must give similar results as when starting at $t = 0$ till $t = T$.

To find symmetry plane $y = 0$, the symmetry operator S_y is introduced, which is defined as $S_y(x, y, z) = (x, -y, z)$. An adapted form of forcing protocol D starting at $t = T/8$ is used. This adapted protocol is described by

$$\boldsymbol{\Phi} = \boldsymbol{F}_{1h}\boldsymbol{F}_4\boldsymbol{F}_3\boldsymbol{F}_2\boldsymbol{F}_{1h}, \qquad \text{with } \boldsymbol{F}_{1h} = \boldsymbol{F}_1^{1/2}. \tag{C.1}$$

For the derivation of the global time-reversal symmetries, the symmetries of every single forcing (steady flow) step are exploited, see paragraph 2.5. A special property of protocol D is that step 4 is the inverse of step 2, this results in

$$\boldsymbol{F}_2 = \boldsymbol{F}_4^{-1} \qquad \text{and} \qquad \boldsymbol{F}_4 = \boldsymbol{F}_2^{-1}. \tag{C.2}$$

Substitution of (C.2) in equation (C.1) leads to

$$\boldsymbol{\Phi} = \boldsymbol{F}_{1h}\boldsymbol{F}_2^{-1}\boldsymbol{F}_3\boldsymbol{F}_4^{-1}\boldsymbol{F}_{1h}. \tag{C.3}$$

Every single step exhibits two symmetry planes: an ordinary reflection symmetry in the radial plane aligned to the forcing direction and a time-reversal symmetry orthogonally to that plane, see

Speetjens (2001). Four of these symmetry relations are needed to derive one of the time-reversal symmetries. The first needed are

$$\begin{aligned} \boldsymbol{F}_2 &= S_y \boldsymbol{F}_2 S_y \quad \text{and thus} \quad \boldsymbol{F}_2^{-1} = S_y \boldsymbol{F}_2^{-1} S_y, \\ \boldsymbol{F}_3 &= S_y \boldsymbol{F}_3^{-1} S_y, \\ \boldsymbol{F}_2 &= S_y \boldsymbol{F}_2 S_y \quad \text{and thus} \quad \boldsymbol{F}_2^{-1} = S_y \boldsymbol{F}_2^{-1} S_y. \end{aligned} \tag{C.4}$$

Substitution of the three inverse symmetry relations of equation (C.4) into equation (C.3) and sandwich the equation between S_y gives

$$S_y \boldsymbol{\Phi} S_y = S_y \boldsymbol{F}_{1h} S_y \boldsymbol{F}_2^{-1} S_y S_y \boldsymbol{F}_3^{-1} S_y S_y \boldsymbol{F}_4^{-1} S_y \boldsymbol{F}_{1h} S_y. \tag{C.5}$$

To complete the inverse relation the following single step symmetry relation is needed:

$$\boldsymbol{F}_{1h} = S_y \boldsymbol{F}_{1h}^{-1} S_y \quad \text{and thus} \quad \boldsymbol{F}_{1h}^{-1} = S_y \boldsymbol{F}_{1h} S_y. \tag{C.6}$$

Substitution of the last relation of equation (C.6) and using $S_y S_y = I$ results in the global symmetry relation

$$S_y \boldsymbol{\Phi} S_y = \boldsymbol{F}_{1h}^{-1} \boldsymbol{F}_2^{-1} \boldsymbol{F}_3^{-1} \boldsymbol{F}_4^{-1} \boldsymbol{F}_{1h}^{-1} \text{ and thus } S_y \boldsymbol{\Phi} S_y^{-1} = \boldsymbol{\Phi}^{-1}. \tag{C.7}$$

The last equation proves that the plane $y = 0$ is a plane of time-reversal symmetry under forcing conditions of protocol D.

The same mathematical structure can be used, starting one step later, to find that plane $x = 0$ is a plane of time-reversal symmetry under forcing conditions of protocol D too. To find symmetry plane $x = 0$, the symmetry operator S_x is introduced, which is defined as $S_x(x, y, z) = (-x, y, z)$.The adapted forcing protocol D is described by

$$\boldsymbol{\Phi} = \boldsymbol{F}_{2h} \boldsymbol{F}_1 \boldsymbol{F}_4 \boldsymbol{F}_3 \boldsymbol{F}_{2h}, \qquad \text{with } \boldsymbol{F}_{2h} = \boldsymbol{F}_2^{1/2}. \tag{C.8}$$

Another property of protocol D is that step 1 is the inverse of step 3, this results in

$$\boldsymbol{F}_1 = \boldsymbol{F}_3^{-1} \qquad \text{and} \qquad \boldsymbol{F}_3 = \boldsymbol{F}_1^{-1}. \tag{C.9}$$

Substitution of (C.9) in equation (C.8) leads to:

$$\boldsymbol{\Phi} = \boldsymbol{F}_{2h} \boldsymbol{F}_3^{-1} \boldsymbol{F}_4 \boldsymbol{F}_1^{-1} \boldsymbol{F}_{2h}. \tag{C.10}$$

Four of these symmetry relations holding for a single step are needed to derive one of the time-reversal symmetries. The first needed are

$$\begin{aligned} \boldsymbol{F}_1 &= S_x \boldsymbol{F}_1 S_x \quad \text{and thus} \quad \boldsymbol{F}_1^{-1} = S_x \boldsymbol{F}_1^{-1} S_x, \\ \boldsymbol{F}_3 &= S_x \boldsymbol{F}_3 S_x \quad \text{and thus} \quad \boldsymbol{F}_3^{-1} = S_x \boldsymbol{F}_3^{-1} S_x \\ \boldsymbol{F}_4 &= S_x \boldsymbol{F}_4^{-1} S_x. \end{aligned} \tag{C.11}$$

Substituting the three inverse symmetry relations given in equation of (C.11) into the equation (C.10) and sandwich the equation between S_x gives

$$S_x \boldsymbol{\Phi} S_x = S_x \boldsymbol{F}_{2h} S_x \boldsymbol{F}_3^{-1} S_x S_x \boldsymbol{F}_4^{-1} S_x S_x \boldsymbol{F}_1^{-1} S_x \boldsymbol{F}_{2h} S_x. \tag{C.12}$$

To complete the inverse relation the following single step symmetry relation is needed:

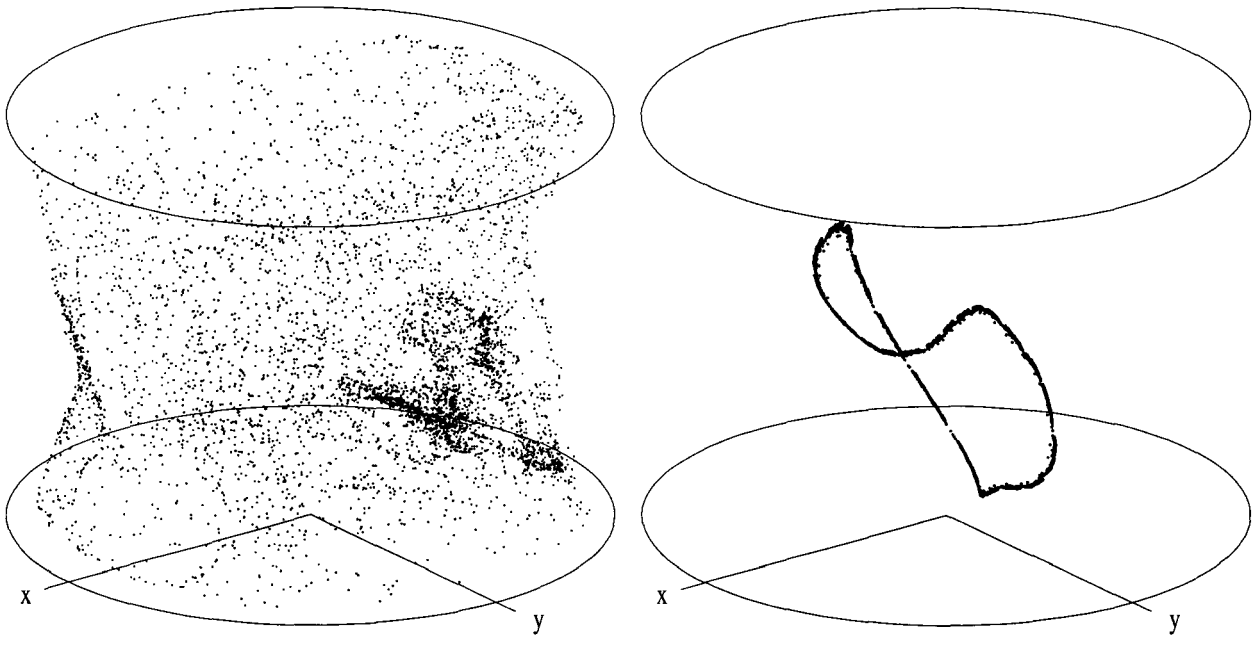

Figure C.1: Poincaré map of a tracer particle followed over 5,000 global periods T. On the left side the Shankar method is used and on the right side the spectral method is used ($Re = 0$).

$$\boldsymbol{F}_{2h} = S_x \boldsymbol{F}_{2h}^{-1} S_x \quad \text{and thus} \quad \boldsymbol{F}_{1h}^{-1} = S_x \boldsymbol{F}_{1h} S_x. \tag{C.13}$$

Substitution of the last relation of equation (C.13) and using $S_y S_y = I$ results in the global symmetry relation

$$S_x \boldsymbol{\Phi} S_x = \boldsymbol{F}_{2h}^{-1} \boldsymbol{F}_3^{-1} \boldsymbol{F}_4^{-1} \boldsymbol{F}_1^{-1} \boldsymbol{F}_{2h}^{-1} \text{ and thus } S_x \boldsymbol{\Phi} S_x^{-1} = \boldsymbol{\Phi}^{-1}. \tag{C.14}$$

This equation proves that the plane $x = 0$ is a plane of time-reversal symmetry under forcing conditions of protocol D. Starting another one step later results again in the time-reversal symmetry plane $y = 0$ and when starting at the fourth step results again in the time-reversal symmetry plane $x = 0$, these are precisely the same symmetry relation half a global forcing period later, see also figure 4.4.

C.0.2 Shankar method versus spectral method in the non-inertial limit

Large differences are found between Poincaré maps, when using the different numerical simulation methods. To show the difference, a tracer is released at (0.1231,0.3912,-0.6510), which is the same starting point as for all other poincaré maps in this report, and followed under forcing conditions of Protocol D over 5,000 global time periods T. The Poincaré map obtained with the semi-analytical Shankar method is shown on the left plane of figure 5.2. On the right plane the Poincaré map is shown, using the spectral method. The methods use slightly different boundary conditions, but this can not cause these large differences, qualitatively seen both maps should be equivalent.

To show more details, the complete trajectory over the first 100 global time periods is shown in figure C.2 using both methods, with on the left plane the Shankar method and on the right plane the spectral method.

The particle trajectory simulated with the spectral method obeys to both time-reversal symmetries, which are proven in paragraph C.0.1. This particle trajectory is said to be double-symmetric. The

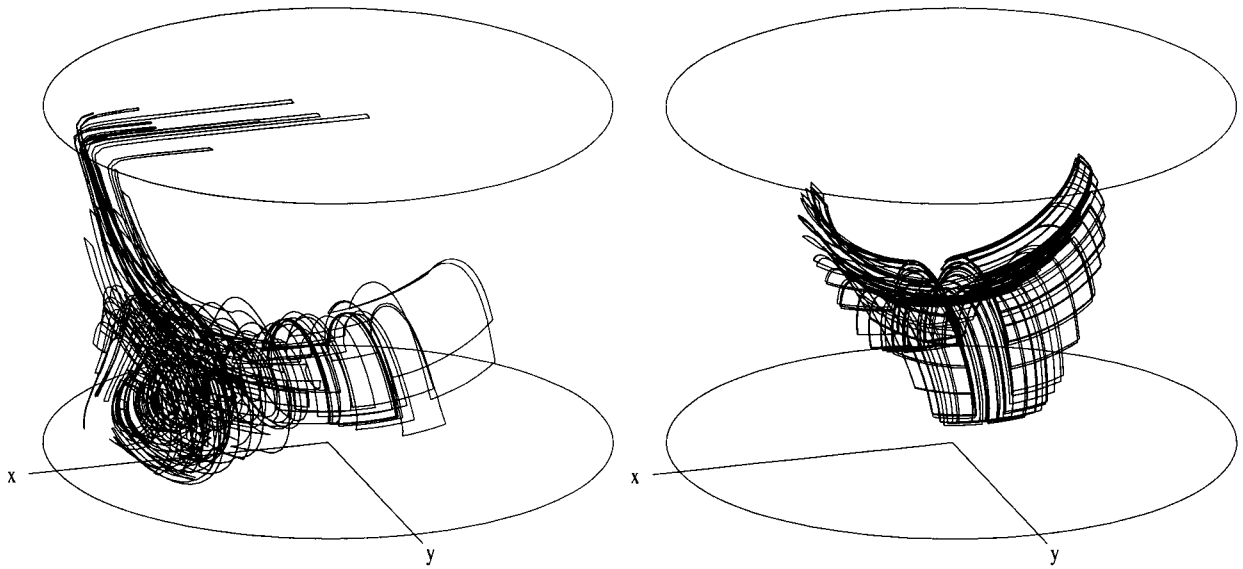

Figure C.2: The tracer particle trajectory followed the first 100 global time periods T. On the left side the Shankar method and on the right side the spectral method is shown. The right plane figure is symmetrically in the planes $x = 0$ and $y = 0$.

tracer particle trajectory simulated with the Shankar method is almost symmetrically in the plane $y = 0$, but definitely not symmetrically in the plane $x = 0$. Particle trajectories in the non-inertial limit should obey to the time-reversal symmetries, this is only seen when using the spectral method. Despite the slightly different boundary conditions, the spectral method gives qualitatively better results in the non-inertial limit when the flow is forced over a long time. The Poincaré map, when using the spectral method, is 1 dimensional, making the flow under forcing conditions of protocol D in the limit $Re = 0$ an integrable state III system. Such a system is comparable to the steady flow. At very low Reynolds numbers ($Re = 1$) symmetry relations are broken and the integrable state III system alters into an integrable II system.

It seems that in the Shankar case, there is some numerical error braking the laws of symmetry, which is possibly caused by not using enough terms of the in fact infinite series. The Shankar method uses Bessel functions, which are known having not that good convergence. To do simulations the first 25 terms are used only. According to Shankar (1997), it is enough to use 20 terms, to gather a good picture of the flow field. Shankar focused on the steady flow case. It is possible that when applying forcing protocol D to the flow, more terms should be used, to require sufficient accurate results over long forcing times.

The time-reversal symmetries are broken at very low Reynolds numbers. The Poincaré map simulated by using the Shankar method is qualitatively good comparable to $Re = 1$, when using the spectral method.

Appendix D

Technology Assessment

Transport of passive tracers is an important issue in a variety of physical and chemical systems, both in nature and technology. For example, in the geophysical context, the study of transport characteristics of passive scalars in flow systems is relevant to the problem of dispersion of pollutants in the atmosphere and in the ocean and to mixing problems in estuaries. In technological context, mixing processes are of crucial importance for polymer processing, (petro) chemical industry and chemical reaction vessels, to mention only a few examples. Many of these mixing processes are essentially three dimensional. An illustrative example is the short-dwell coater, which is used to produce high-grade paper and photographic film, the structure of the flow field in the liquid pond can greatly influence the quality of the coating on the roll. A schematic view is given in figure D.1.

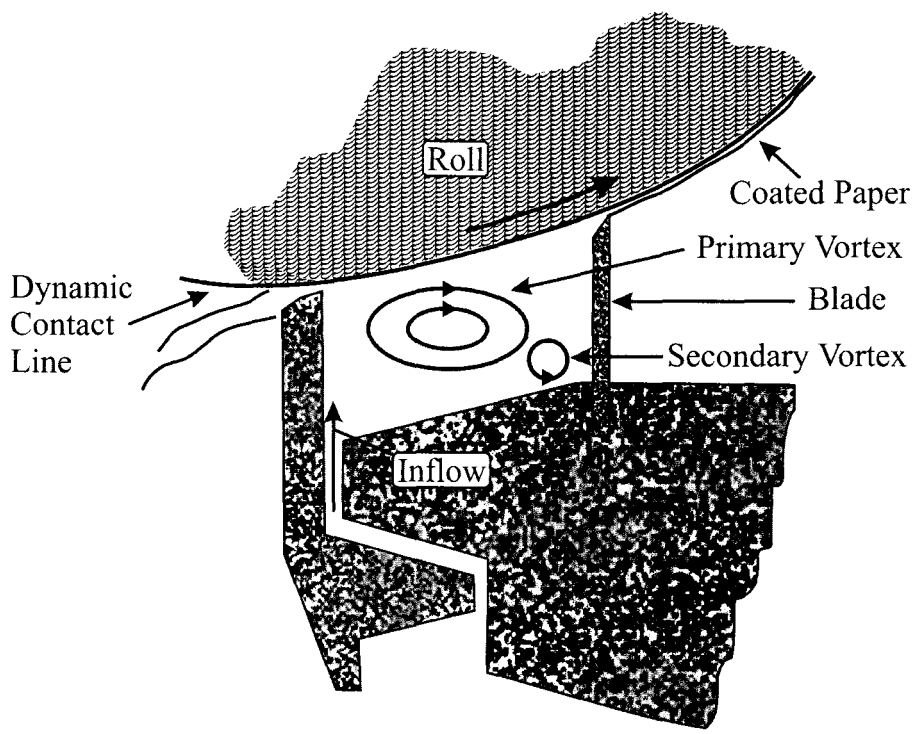

Figure D.1: A schematic view of a short-dwell coater from Shankar & Desphande (2000).

In many practical situations the major challenge is to establish the most efficient mixing of certain components. Efficient mixing reduces energy costs and can prevent oversizing of industrial plants. Mixing processes in industry are often characterized by a three-dimensional viscous flow in a non-Newtonian fluid in a complex geometry. As a first step to understand three-dimensional mixing in a viscous fluid, a few simplifications are usually made by considering an incompressible

Newtonian fluid flow in a relatively simple geometry such as a cylinder. Almost all phenomena that can occur are still possible after these simplifications. Examples of these phenomena are: eddies, secondary flows, complex three-dimensional patterns, chaotic particle motions, instabilities, transition and turbulence.

The $3D$ PTV measurement technique is a quantitative measurement technique following passive tracer particles in the fluid. Phenomena like the eddy structure or $3D$ mixing processes can be followed very accurately. The $2D$ PTV variant is already shown to be successful and is widely used in all kinds of experiments.

Bibliography

Anderson, P. D.: 1999, *Computational Analysis of Distributive Mixing*, PhD thesis, Eindhoven University of Technology.

de Groot, J. P. J.: 2001, Mixing measurements in stokes flow in a cylindrical container, *Technical report*, Eindhoven University of Technology.

Nijdam, S.: 2000, *Concentration measurements in a stratified fluid using laser induced fluorescence*, Master's thesis, Eindhoven University of Technology.

Ottino, J. M.: 1989, *The Kinematics of Mixing: Stretching, Chaos and Transport*, Cambridge University Press.

Pedrotti, F. L. and Pedrotti, L. S.: 1993, *Introduction to Optics*, Prentice-Hall.

Schreel, K. R. A. M., van der Plas, G. A. J. and Kieft, R. N.: 2000, Accuracy of a 3d particle tracking velocimetry method, *9th international symposium on flow visualisation* .

Shankar, P. N.: 1997, Three-dimensional eddy structure in a cylindrical container, *J. Fluid Mech.* **342**, 97–118.

Shankar, P. N. and Deshpande, M.: 2000, Fluid mechanics in the driven cavity, *Annual Review Fluid Mechanics* **32**, 93–136.

Simons, P.: 1995, A comparison of two velocity measuring techniques in a laminar flow, *Reportnumber woc-wet 95.051*, Eindhoven University of Technology.

Speetjens, M. F. M.: 2001, *Three-Dimensional Chaotic Advection in a Cylindrical Domain*, PhD thesis, Eindhoven University of Technology.

Telionis, D. P.: 1981, *Unsteady Viscous Flows*, Springer, New York.

Virant, M. and Dracos, T.: 1997, 3d PTV and its application on lagrangian motion, *Meas. Sci. Technol.* pp. 1539–1552.

Zoeteweij, M. and van der Plas, G. A. J.: 2001, PIV, PTV and HPV user's guide, *Technical report*, Eindhoven University of Technology.